

Solid-Fluid Transitions in Wet Granular Material

Dissertation

**zu Erlangung des Doktorgrades der
Mathematisch-Naturwissenschaftlichen
Fakultäten der Georg-August-Universität zu Göttingen**

vorgelegt von

S. H. Ebrahimnazhad Rahbari

geboren in Tabriz (West Azarbayjan), Iran

Göttingen, 2009

Referent: Prof. Dr. Stephan Herminghaus,

Koreferent: Prof. Dr. Markus Müller

Tag der mündlichen Prüfung :

*To:
Ata,
Ana,
Hadi,
and sand castles*

Abstract

In this thesis, the stability and the dynamics of wet granular materials under shear are explored. Inspired by the Green's function approach, a theoretical model for yielding of a wet pile on an inclined plane is presented. It enables one to predict the critical inclination angle at which the pile fluidizes. The theory is based on the balance of forces acting on each particle at the vicinity of the fluidization and has two major consequences. First, the theory shows that yielding of a wet pile does depend on the gravitational acceleration, whereas a dry pile fluidizes for any arbitrary small non-zero gravitational acceleration when the inclination angle exceeds a certain value depending on the geometry. Second, the theory shows that a wet pile yields in the bottom layer where the pile touches a non-slip boundary. There is excellent agreement between the theory and extensive MD-type simulations where one calculates forces between each individual pair of particles. The dynamics of driven wet particles is studied in two different ways. First, we explore dynamics of wet particles in a channel driven by gravity. Second, we apply a spatially sinusoidal driving force. In both cases we find discontinuous hysteretic solid-fluid transitions, i.e. solid-to-fluid and fluid-to-solid transitions and encountered at different forcing of the system. We calculate phase diagrams separating solid and fluid states and thresholds for the solid-to-fluid and the fluid-to-solid transitions. Beside that, we study the spatial and temporal distributions of drift velocity, granular temperature, area fraction, stress tensor, interparticle force etc.

Kurzzusammenfassung

In dieser Arbeit wird die Stabilität und Dynamik feuchter granularer Medien unter der Einwirkung von Scherkräften untersucht. In Anlehnung an den Greenschen Formalismus wird ein theoretisches Modell für das Brechen und Abrutschen eines feuchten granularen Haufens auf einer geneigten Ebene vorgestellt. Dieses Modell erlaubt eine Vorhersage des kritischen Neigungswinkels, also des Winkels, an dem das Material zu rutschen beginnt. Die Theorie beruht auf dem Gleichgewicht der Kräfte in der Nähe des Fluidisierungspunktes und hat zwei weitreichende Folgen: Zunächst zeigt die Theorie, dass das Nachgeben des granularen Haufens von der Grösse der Erdschleunigung abhängt. Ein trockener Haufen hingegen fluidisiert im verwendeten Modell bei jeder noch so kleinen Normalbeschleunigung, sobald der Neigungswinkel einen bestimmten Wert überschritten hat. Desweiteren zeigt die Theorie, dass der granulare Haufen in der Höhe der Auflage nachgibt, sofern dort eine Randbedingung ohne Schlupf angenommen wird. Die theoretischen Vorhersagen werden im Detail von MD Simulationen bestätigt, die auf der Berechnung der individuellen Kräfte zwischen benachbarten Teilchen beruhen. Das dynamische Verhalten von feuchten Granulaten, die durch äussere Kräfte angetrieben werden, wird anhand von zwei Modellsystemen untersucht. Auf der einen Seite wird die Dynamik eines feuchten Granulats in einem Kanal unter der Einwirkung der Schwerkraft betrachtet. Auf der anderen Seite wird der granulare Haufen einer räumlich sinusförmig variierenden externen Kraft unterworfen. In beiden Fällen findet man einen un stetigen und hysteretischen dynamischen Übergang, d.h die Grösse der äusseren Kräfte, bei dem das System von einem fluidisierten in einen festen Zustand bzw. von einem festen in einen fluidisierten Zustand übergeht, sind nicht identisch. Der Übergang zwischen beiden dynamischen Zuständen des Systems wird anhand von Phasendiagrammen veranschaulicht werden. Desweiteren werden die zeitlichen und räumlichen Verteilung einer Reihe physikalischer Grössen, wie z.B. der Driftgeschwindigkeit des Granulats, der granularen Temperatur, der Dichte, der mechanischen Spannungen sowie der Kräfte zwischen den Teilchen des Granulats,

betrachtet.

Table of Contents

Abstract	i
Kurzzusammenfassung	iii
Contents	vii
1 Introduction	1
1.1 Landslides	3
1.1.1 La Conchita Landslide, California	4
1.1.2 Mobility of the fluidized landslides	5
1.1.3 Modeling a fluidized landslide	6
1.2 Physical model for wet granular matter	7
1.2.1 Overview	7
1.2.2 Repulsive interactions	7
1.2.3 Capillary bridges	9
1.2.4 Rescaled units	11
1.2.5 Physical quantities	11
1.3 Numerical implementation	12
1.3.1 5th order Gear method	14
1.3.2 Accuracy of the Gear method for different interaction forces	17
2 Stability of a granular pile	19
2.1 Motivation	19
2.2 Theoretical formalism	20
2.2.1 Critical angle	20
2.2.2 Isostatic dry pile	23
2.2.3 Isostatic wet pile	27
2.3 Numerical simulations of monodisperse disks	29
2.3.1 An isostatic wet pile	29

2.3.2	An isostatic wet pile with height disorder	30
2.3.3	A hyperstatic wet pile	32
2.3.4	A hyperstatic wet pile with height disorder	34
2.3.5	Rupture length and stability of a wet pile	35
2.4	Numerical investigations of the stability of bidisperse piles	36
2.4.1	Preparation step	37
2.4.2	Protocol of the numerical simulation	37
2.4.3	Critical angle of a bidisperse dry pile	38
2.4.4	Stability of a wet bidisperse pile	41
3	Wet disks running down an inclined plane	43
3.1	Convergence to the steady state	43
3.2	Profiles	44
3.2.1	Downhill velocity	45
3.2.2	Local area fraction and granular temperature	47
3.2.3	capillary bridges	49
3.2.4	Stress field	50
3.3	Longer capillary bridges	52
3.4	Formation of capillary bridges	54
3.5	Hysteretic solid-fluid transitions	57
3.5.1	Phase diagrams	57
3.6	Leidenfrost state	62
3.6.1	Summary	66
3.7	Appendix	66
3.7.1	Quadratic velocity profile	66
4	Isochoric model for avalanches	69
4.1	Description of the model	69
4.1.1	Preparation	71
4.2	Results	72
4.2.1	Time evolution	72
4.2.2	Fluidized-to-solid transition	76
4.2.3	Dry disks under external driving	80
4.3	Distribution of physical quantities	81
4.3.1	Profiles of drift velocity and shear rate	82

TABLE OF CONTENTS**vii**

4.3.2	Area fraction and granular temperature	83
4.3.3	Liquid bridge number and rupture frequency	85
4.3.4	Stress field	88
4.3.5	Viscosity	92
4.3.6	Interparticle forces	95
4.4	Hysteretic transitions	99
4.4.1	Phase diagram	101
4.4.2	Why hysteretic-discontinuous transition?	105
4.5	Appendix	106
4.5.1	Relation between driving force and shear stress	106
5	Conclusion	109
	Appendices	111
A	Symbols and notations	113
B	Energy balance	115
C	Derivation of stress tensor	119
C.1	Tensorial form of the Virial theorem	119
C.2	Stress Tensor in 2D	121
	References	123
	Acknowledgments	129

Chapter 1

Introduction

Due to frictional forces and inelastic collisions between grains, granular material exhibit a rich variety of emergent properties [1]. Granular material may behave like an unusual solid. When granulates such as wheat or rice are kept in a silo, due to the force chains inside the bulk and the frictional forces between grains and sides of the container, pressure does not depend on the height of the material. Furthermore, granular material may behave like an unusual fluid. Granular material can be fluidized and flow like a liquid. To describe such a fluid in particular its dynamics, it is useful to have a continuum theory of granular matter. Since granular fluids are extremely heterogeneous, continuum models are being debated. Granular matter may also behave like an unusual gas. Due to inelastic collisions between granulates, in any collision, the energy is dissipated according to the restitution coefficient. The velocity distribution of the particles does not follow the Maxwell-Boltzmann distribution, and one can not carry over the equilibrium statistical mechanics.

These unusual properties of granular materials tempt scientists and engineers to study granular matter. Most studies on granular media have focused on dry granular matter, where the effects of adhesion due to interstitial fluid have not been taken into the account. In the real world, however, we often find wet granular material such as beach sand. Wet granular materials are cohesive due to the surface tension of the wetting liquid [2]. Due to complexity of wet granular matter, in the last decades, many people who studied granular material, avoided the humidity in their studies. Even in some cases, the experiments have been done in vacuum chambers [3] and humidity was seen as a nuisance. The complexity of granular matter increases when the humidity is added into the system [4].

Dry sand and water are not pasty. However, when a small amount of water is mixed into

dry sand, eventually a pasty material will emerge which allows to sculpture a stable sand castle. A satisfactory theory of wet granular matter has been launched in recent years [5–7]. The stability of a pile of wet granular material is caused by numerous capillary bridges between grains which act as glue. When liquid is added to dry granular matter, in the ideal case, each grain has a thin liquid layer. As soon as two grains touch each other, at the contact region, a sharp bend forms on surface of the liquid film. That sharp bend gives rise to a large negative Laplace pressure which sucks the liquid towards the contact region as long as the liquid surface acquires a spatially constant mean curvature which can be interpreted as equilibrium and a capillary bridge [2]. However, if the amount of liquid is larger than about 7% of the total volume, there no longer will be any capillary bridge and structure of clusters will grow [8].

Results of the investigations on wet granular material can be applied on Industrial Pharmacology, food processing, dynamics of snow [9], and applications on civil engineering, *e.g.* huge and expensive civil work projects like the construction of the Kansai international airport on a man-made island in Japan [10]. Most of natural hazards, such as landslides and debris flows, happen after a period of heavy rain. In these catastrophic phenomena, fluidized wet granular matter plays an essential role.

We are interested to study the stability and the dynamics of wet granular matter under shear [11]. Wet and dry granular matter under shear have tempted many groups to investigate their dynamics, both theoretically and experimentally [12–14]. Losert *et al.* [15] studied experimentally particle dynamics of dry granular matter in a Couette geometry with an inner rotating wall. They explored the velocity profile of the system and showed that the velocity profile is strongly nonlinear and decreases with distance from the moving wall. They proposed that such a nonlinear granular flow can be well described by a Newtonian fluid with local temperature and density dependent viscosity. They found that there may be a useful analogy between dynamics of granular material and the behavior of the super cooled liquids close to glass transition.

Xu *et al.* [16] performed molecular dynamics simulations of soft frictionless dry particles with a moving wall. They studied the influence of packing fraction on the velocity profile, and found a non-linear velocity profile for high density fractions. A critical boundary velocity (u_c) exists above which the mean velocity profile is nonlinear, and below which the mean velocity profile becomes linear.

Although most studies on granular matter under shear are restricted to dry granular matter, there are a few reports on wet granular matter under shear. Schulz *et al.* [11] studied numeri-

cally cohesive spheres in 3D under a spatially periodic external force. They used particles that are very soft when they touch each other, but become extremely repulsive when they overlap more. They found a solid-fluid transition, when the amplitude of the external force field exceeds a critical value. In their model, dissipation is only due to the capillary bridge rupture events.

There are still many open questions about the dynamics of wet granular matter under shear. How does a wet granular pile yield? Does a fluid-solid transition exist and is it hysteretic? How does the fluidization threshold depend on rupture separation of the liquid bridges, density fraction, system size etc? How does viscosity depend on granular temperature, shear rate, density fraction etc. How does the inter-particle force distribution look like? Is there any specific symmetry that can describe the stress field in wet granular matter? These questions are our objectives in this thesis.

1.1 Landslides

Landslides are the natural form of fluidization of granular materials. They are geological phenomena which include a wide range of ground movements [17–21]. Accordingly, there are many different definitions to landslides. Cruden [22] defines landslide as a movement of a mass of rock, earth or debris down a slope.

According to Varens [23], it is a downward and outward movement of slope forming materials under the influence of gravity. Hutchinson [24–28] classifies slope movements into the eight categories:

1. *Rebound*: movements associated with human excavation and naturally eroded valleys.
2. *Creep*: slow downward progression of rock and soil down a low grade slope.
3. Sagging of mountain slopes.
4. Rotational and compound slides
5. *Topples*: forward rotation of a mass of rock, or soil about a pivot or hinge on a hill slope.
6. *Falls*: free movement of material away from steep slopes such as cliffs.
7. Complex slope movement

8. Debris movement of fluidized form: dry and wet debris flow

We are interested in the last category of Hutchinson's classification. After a heavy rain, when wet soil becomes too heavy and exceeds its yield stress, it fluidizes and produces a landslide. Observations show that a fluidized landslide normally starts with sliding, then fluidizes, and changes into a debris flow [29]. Liquefaction is an important mechanism in such a landslide which fluidization occurs along the sliding surface. Bishop [30] notes that fluidization can be distinguished from general sliding, which usually has an intact soil mass above the sliding surface. Hutchinson mentions that:

flow-like motion consequent to fluidization is a neglected and little-understood group of movements [28].

Furthermore, geological data show that during the flow of a fluidized landslide, the highest shear stresses are concentrated within a thin shear layer located deep inside the landslide, whereas the upper cap remains relatively undisturbed [31, 32].

1.1.1 La Conchita Landslide, California

As an example of a fluidized landslide, we report the landslides occurred at La Conchita, California. These landslides have been well documented by the U.S. Geological Survey [33]. 1995 was an extraordinarily wet season for La Conchita. Fig.1.1a shows the rainfall at La Conchita from October 1, 1994, through March 31, 1995. Landslide failed on March 4, 1995, and one can count at least 7 heavy rainfalls from Fig.1.1a in just a period of 1 month before the first landslide. Moreover, on March 4, 1995 at 2:03 pm, the La Conchita first landslide failed and moved tens of meters in a few minutes. Fortunately, nobody was injured or killed, but it destroyed nine houses. On March 10, a subsequent debris flow damaged five additional houses in the northwestern part of La Conchita. In particular, the extraordinary rainfall of January 1995 probably was the principal contribution factor to the landslide movement.

On January 10, 2005, another landslide struck the community of La Conchita, destroying or seriously damaging 36 houses. The second landslide occurred at the culmination of 15-day high rainfall period. Unfortunately, 10 people were buried in debris flow.

The first landslide in 1995, was a deep, coherent slump-earth flow that deformed plastically and moved slow enough that people could get out of its way. The second landslide in 2005 was a shallower fluidization of the very same material into a rapid, highly fluid debris flow. However, due to the heavy rainfalls before both landslides, it is clear why these landslides

failed, however why and how the same material fluidized twice in 10 years by fundamentally different flow behavior, will certainly be the object of future research on physics of fluidized wet grains.

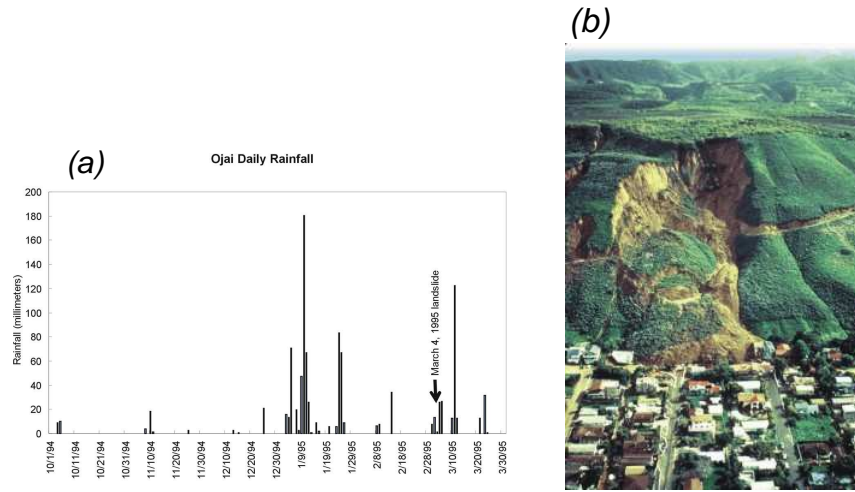


Figure 1.1: (a) Daily rainfall at La Conchita from October 1, 1994 through March 31, 1995. The 1995 landslide occurred more than 1 month after the heaviest rainfall of the season. (b) Snapshot of La Conchita, after 1995 landslide (nobody was injured [33]). There is a trail on the slope which has a curve shape after the landslide, being a hint for plastic deformation of the material during the landslide.

1.1.2 Mobility of the fluidized landslides

One of the challenging questions about fluidized landslides is to understand the mobility of a landslide [34, 35]. Numerous suggestions have been put forward to explain the mobility of large landslides. Some researchers have suggested mechanisms based on lubrication by an air layer trapped underneath the landslide [31], acoustic fluidization due to high-frequency acoustic waves travelling through the granular medium [36], dispersive forces exerted by powder-sized grains [37], mechanical fluidization [38–40]. Habib [41] and Goguel [42] independently suggest that there is so much heat generated in the slippage plane that water will be quickly brought to the boiling point and transform into vapor. The consequent build of water vapor pressurized could act as a lubricant in the shear layer, thus increasing the landslide mobility. Apparently there are some mechanisms which reduce friction and increase the lubrication of a fluidized landslide, but to find the dominant mechanism one has to construct simple mod-

1) The highest shear stresses are localized within a thin shear layer deep inside the landslide [31, 32].
2) Fluidized landslides occur normally after a period of heavy rainfall, hence water content is essential for fluidized landslides.

Table 1.1: Two common features of fluidized landslides.

els to explore the influence of each mechanism individually. Inspired from landslides, in the current study we construct simple models to understand yielding of wet granular matter.

1.1.3 Modeling a fluidized landslide

Due to complex fractal geometry of soil grains and diverse interparticle interactions between them, it is not easy to create a simple model which describes fluidized landslide [43]s. There are some attempts to explore fluidized landslides using numerical experiments. Most of them are based on continuum models [34]. They do not take into account microscopic interactions between the grains. However, we are interested to develop a microscopic model which allows us to study the influence of interparticle interactions between the individual grains on the behavior of large systems. There are many parameters which play an important role in such systems, *e.g.* the shape of the particles, friction, moisture etc.. Friction is one of the parameters which depends on the shape of the particles as well as their material structure. For instance, sand beads made by water erosion have less friction than many other kinds of the grains. Moisture is also another important parameter to study fluidized landslides. When two neighbor grains are wet, due to the surface tension of liquid film at the contact point an attraction force acts between neighbors which is hysteretic, *i.e.* when two grains approach each other there is no capillary interaction. Finding the common features of fluidized landslides could probably help us to know which features play a dominant role. Studying portfolios of fluidized landslides, one finds that they all have the following two main features: As an example to demonstrate impact of moisture on fluidized landslides, Fig.1.2 shows an experiment to induce a fluidized landslide by artificial rainfall has been done by Hirotaka Ochiai *et al.* [29], at Mt. Kaba-san, Japan 2004. Average slope gradient was 33° , and the rainfall intensity was 78 mm/h . They found also a curve shape during plastic deformation of the artificial landslide (marked by the yellow arrow), similar to La Conchita 1995 landslide.



Figure 1.2: A fluidized landslide caused by an artificial rainfall.

1.2 Physical model for wet granular matter

1.2.1 Overview

In this section, we present our simplified physical model which describes wet granular matter. For simplicity, the grains are supposed to be circular 2D disks in our model. We use soft disks that interact via repulsive forces when they 'overlap'. In addition, in section 1.2.3 we take capillary bridge interaction into account.

1.2.2 Repulsive interactions

When two adjacent soft disks touch each other and subsequently 'overlap', they interact via a short range repulsive force. Several methods have been suggested to model the repulsive interactions. We introduce some of those models in the following.

Hard core model is used in event-driven molecular dynamics simulations of soft particles.

$$F(r_{ij}) = \begin{cases} \infty & \text{if } r_{ij} \leq R_i + R_j; \\ 0 & \text{if } r_{ij} > R_i + R_j. \end{cases}$$

in which R_i and R_j are radii of particles i and j , and r_{ij} is the center to center distance between two particles.

Spring-like forces are a class of repulsive forces that can be used in the force-based molecular dynamics simulations.

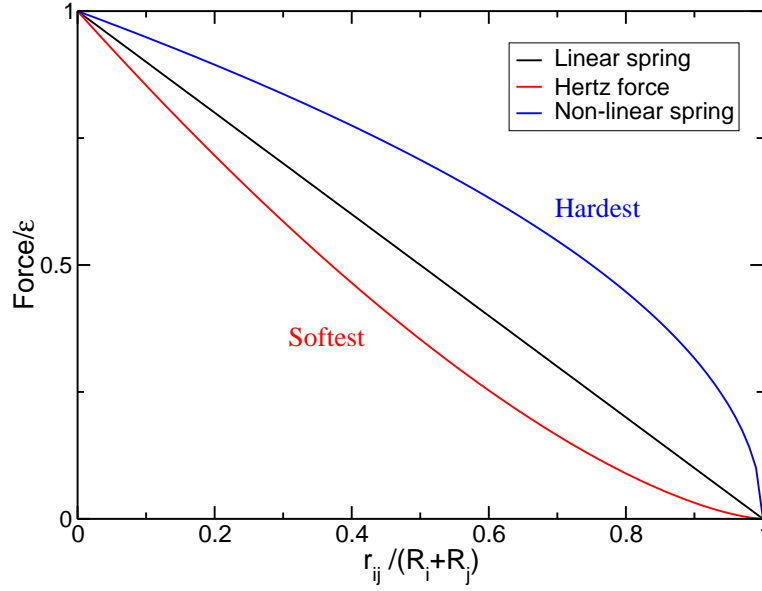


Figure 1.3: Repulsive interparticle force as a function of the rescaled distance. The blue curve shows the nonlinear spring force. The linear spring depicted by the red curve and the black curve shows the Hertz force. Y axis (force) is rescaled on the ϵ .

$$F(r_{ij}) = \begin{cases} \epsilon(R_i + R_j - r_{ij})^\alpha & r_{ij} \leq R_i + R_j \\ 0 & r_{ij} > R_i + R_j \end{cases}$$

where r_{ij} is the center to center distance between particles, while R_i and R_j are the radii of the particles i and j . The exponent $\alpha = \{0.5, 1, 1.5\}$ correspond to nonlinear spring, linear spring, and Hertzian force respectively. The radius dependent prefactor $\epsilon = A \cdot (R_i \cdot R_j) / (R_i + R_j)$ and A is a constant.

Schultz's Force is another type of the repulsive forces [11]. It is given by:

$$U(r_{ij}) = \begin{cases} (\xi^{-13} + (\xi - 1)\xi_0^{-13}/(\xi_0 - 1)) & \xi \leq \xi_0 \\ 0 & \xi > \xi_0 \end{cases}$$

where $\xi = r_{ij}/(R_i + R_j)$, and $\xi_0 = 1.05$. This model is a mix of repulsive Lennard-Jones and repulsive spring. When two particles overlap the spring force is dominant and as one decreases the particle indentation, the first part will dominate.

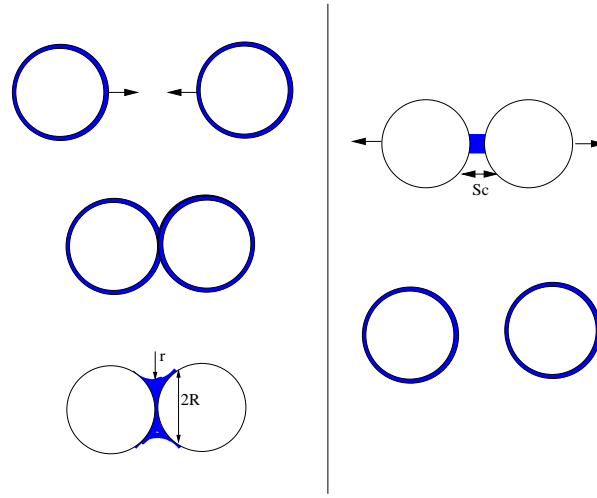


Figure 1.4: Formation (left) and rupturing (right) of a liquid bridge. **Top-left:** two wet grains are approaching. The liquid films depicted by blue thin layers on the surface of two grains. **Left-center:** two wet grains touch each other. **Bottom-left:** a capillary bridge forms at the contact region. **Bottom-right:** when two grains are pulled out, a pendular bridge forms. **Top-right:** capillary bridge ruptures as the separation between two grains exceeds the rupture separation S_c .

1.2.3 Capillary bridges

When a wetting liquid is added to granular material, a thin liquid film forms on surface of each particle. As soon as two adjacent grains touch each other, a sharp bend in the liquid film at the contact region results to a high negative Laplace pressure. Due to the negative Laplace pressure in the contact region, most of the liquid in the film will be sucked into the contact region and eventually a capillary bridge will form. The process of formation of a capillary bridge is shown in Fig.1.4.

The capillary attractive force between two wet grains is a consequence of interfacial tension of the liquid, as well as the difference of pressure between the liquid and the gas phase. Subsequently, a liquid bridge forms and entails to an attractive force between particles as soon as two adjacent grains touch each other. The force switches off as the capillary bridge ruptures. This happens at a limit difference being larger than the separation at which the bridge is formed. Furthermore, the critical separation depends on the liquid content in the system. Experiments prove that the attractive liquid bridge force decreases exponentially with increasing the separation between the grains. It was recently shown by Soulie et al. [44] that the capillary

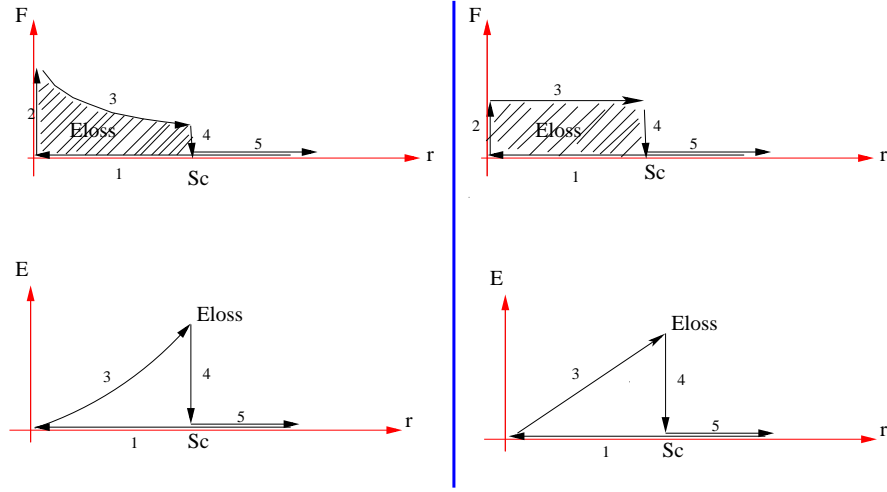


Figure 1.5: **Top-left:** capillary bridge force as a function of the distance between particles. 1: two grains approach each other. 2: as soon as they touch each other a capillary bridge forms and entails to an attractive force. 3: the force decreases particles are stretched. 4: the force switches off as the capillary bridge ruptures. At the end $E_{loss} = \int_0^{Sc} F(r)dr$ is dissipated. **Bottom-left:** the particle energy as a function of the distance. **Top-right:** capillary bridge force versus the distance in the minimal capillary model in which the capillary force is constant as two disks are stretched. **Bottom-right:** particle energy versus the distance in the minimal capillary model.

force can be cast into the form:

$$F(r) = -\pi\gamma_s \sqrt{R_1 R_2} [\exp(Ar + B) + C] \quad (1.1)$$

where R_1 and R_2 are radii of the contacting spheres ($R_1 < R_2$), γ_s is the liquid surface tension, and r is the particles separation. A , B , and C are the fitting parameters and function of the liquid volume V_b and the contact angle θ .

Formation and rupturing of a capillary bridges is illustrated in Fig.1.5-left.

One can simplify the capillary interaction, which is a function of distance between particles, to a minimal force that does not depend on distance between grains. Fig.1.5-right, shows this simplified capillary model. In the minimal capillary model, the capillary bridge force is assumed to be constant as the capillary bridge is stretched. This model has been successfully used to describe the dynamics of wet granular material [4, 45–47].

Symbol	Description
$\langle d \rangle$ =average diameter of the disks	Length unit
mass over area of each disk	Mass unit
f_{LB} =minimal capillary force	Force unit

Table 1.2: The rescaled units of simulations.

1.2.4 Rescaled units

Here, we introduce the rescaled units that will be used for all the simulations in this thesis. The units of simulation is briefly listed in tab. 1.2.

We choose the average diameter of particles as the unit of the length, the minimal capillary force as the unit of the force, and the mass over area of each particle as the unit of the density. This means that mass of each particle equals its corresponding area.

1.2.5 Physical quantities

The best mathematical tool to study the stress field is the *stress tensor*¹ [48]. The stress tensor is composed of two parts:

1. **Kinetic part:** It characterizes the thermal kinetic energy transported into different degrees of freedom by the thermal motion of particles.
2. **Static part:** It characterizes the amount of the momentum transported by the interactions between particles. The static part increases when the area fraction is increased such that there are more contacts.

The stress tensor in 2D can be written as:

$$S = \frac{1}{A} \begin{pmatrix} \sum_i (v_{ix} - U_x)^2 & \sum_i (v_{ix} - U_x)(v_{iy} - U_y) \\ \sum_i (v_{ix} - U_x)(v_{iy} - U_y) & \sum_i (v_{iy} - U_y)^2 \end{pmatrix} + \frac{1}{A} \begin{pmatrix} \sum_{i<j} r_{ijx} F_{ijx} & \sum_{i<j} r_{ijx} F_{ijy} \\ \sum_{i<j} r_{ijy} F_{ijx} & \sum_{i<j} r_{ijy} F_{ijy} \end{pmatrix} \quad (1.2)$$

in which v_i is the velocity of particle i , U_x and U_y are projections of the drift velocity along X and Y direction, $\mathbf{r}_{ij} = \mathbf{r}_j - \mathbf{r}_i$, F_{ij} is the interparticle force between particles i and j , and A is area of the region where the stress tensor is measured.

¹Derivation of the stress tensor is given in Appendix sect.C.

The *granular temperature* is defined as the random kinetic energy of particles. Here, the randomness means that the drift velocity is subtracted from velocity of each particle, so that the temperature can be written as:

$$T_G = \sum_{i=1}^N \frac{1}{2} m_i (\langle v_{ix}^2 \rangle - \langle v_{ix} \rangle^2 + \langle v_{iy}^2 \rangle - \langle v_{iy} \rangle^2) \quad (1.3)$$

where m_i is mass of particle i , and v_{ix} and v_{iy} are components of velocity of particle i along X and Y directions respectively.

1.3 Numerical implementation

Due to the large number of the particles within a typical granular system, and the complicated interparticle forces, the equation of the motion of each particle can not be solved analytically. Numerical methods must be implemented. Our numerical implementation is based on calculating trajectories of the center of mass of each particle from Newton's equation of motion individually on each particle. The calculation of the trajectories of all particles of the system, is called **Molecular Dynamics**. The idea of the Molecular Dynamics was pioneered in 1957 by Adler and Wainwright [49] [50] [51] who attempted to simulate molecular gases and simple liquids [49]. Molecular Dynamics simulations of granular systems are very expensive due to short range interactions of the particles [52]. There are two kinds of the molecular dynamics simulations:

1. **Event-driven Molecular Dynamics:** in systems where the typical duration of a collision is much shorter than the mean time between two successive collisions in the whole system, event-driven Molecular Dynamics is efficient. Hence, the system should be dilute like a granular gas [53]. The algorithm is focused on the calculation of the next collision, and thus the forces in the system has been not taken into the account. Event-driven Molecular Dynamics has been used to study free cooling of dry [54] and wet [55] granular gas.
2. **Force-based Molecular Dynamics:** in systems where the typical duration of a collision is much larger than the mean time between successive collisions, force-based Molecular Dynamics is efficient. It means that the system is densely packed and particles are in enduring contact. In this case, an event-driven algorithm must fail. Furthermore,

in force-based Molecular Dynamics, one can include external force fields like driving force in the system. Force-based Molecular Dynamics has been proven as a powerful method to study dry [56–59] and wet [60] [61] granular matter under shear.

Accordingly, the force-based molecular dynamics is the method of choice to simulate dense granular matter which is our aim. We developed the force-based molecular dynamics to explore the physics of wet granular matter under shear. To perform the molecular dynamics simulation, one should solve the Newton's equation of motion. Newton's equation is a second order ordinary differential equation:

$$\frac{d^2 \mathbf{r}_i(t)}{dt^2} = \frac{1}{m_i} \sum_j \mathbf{F}_{ij} \quad (1.4)$$

where $\sum_j F_{ij}$ is the force between particles i and j , and m_i is mass of particle i . During the preparation of the initial state, a viscous friction F_{drag} is applied individually on each particle to dissipate the injected energy:

$$\mathbf{F}_{drag} = -b \mathbf{v}_i \quad (1.5)$$

a 'virtual fluid' in the background being proportional to the velocity \mathbf{v}_i of the disks. The constant b describes the strength of the damping and is usually set to $b = 0.1$

A standard method to solve such an ordinary differential equation is the Gear method [62, 63]. The advantage of the Gear method is that forces are calculated once in each time step. In the next section, we will explain the method on detail.

To solve the euq.(1.4) for a system consisting N particle during calculation of the total forces acting on each individual particle, we deal with a N^2 problem. To decrease that number, the so-called linked-cell method has been implemented [62]. In this method, the simulation box is divided into a regular lattice of $M \times M$ cells. Particles in each cell interact only with their neighbor cells. This decreases the computational effort to a linear dependence of the number of particles N . Since interactions in granular material are short range, this is a suitable method for such projects. It is clear that the length of the cells should be smaller than the diameter of particles.

To measure the physical quantities, the simulation box is divided into rectangular bins along the direction of the flow. The width of each bin equals to one average particle diameter and its length is equal to the system size. Accordingly, the number of the bins equals the system size. Once the system has reached the stationary state, the measurements are done in each bin within a long simulation time. At the end of the simulations, a spatial profile can be

obtained by averaging over the temporal profiles during the measurements. The final profiles are calculated by averaging over 10000 profiles during a long simulation time.

1.3.1 5th order Gear method

The idea of the 5th order Gear method is to extrapolate solutions for each particle as an initial guess from the Taylor expansion, and correct the predicted values according to difference of the predicted force and the real force which can be calculated directly. If the difference becomes zero then the predicted values are accepted and algorithm proceeds to the next time step². Otherwise, the algorithm corrects the solution in the Corrector step.

Predictor step: Given positions, velocities etc. of particles at time t , we attempt to obtain the positions, velocities etc. at the time $t + \delta t$. Due to continuity of the classical trajectories of the particles, one can use the Taylor expansion to extrapolate the initial solutions:

$$r_i(t + \delta t) = r_i(t) \cdot C(0) + v_i(t) \cdot C(1) + a_i(t) \cdot C(2) + b_i(t) \cdot C(3) + c_i(t) \cdot C(4). \quad (1.6)$$

$$v_i(t + \delta t) = v_i(t) \cdot C(0) + a_i(t) \cdot C(1) + b_i(t) \cdot C(2) + c_i(t) \cdot C(3). \quad (1.7)$$

$$a_i(t + \delta t) = a_i(t) \cdot C(0) + b_i(t) \cdot C(1) + c_i(t) \cdot C(2). \quad (1.8)$$

$$b_i(t + \delta t) = b_i(t) \cdot C(0) + c_i(t) \cdot C(1). \quad (1.9)$$

$$c_i(t + \delta t) = c_i(t) \cdot C(0) \quad (1.10)$$

in which, $C(i) = dt^i/i!$, and dt is the integration time step. v, a, b, c are the first, second, third, and fourth derivatives of the position r . Therefore, in this step, using the Taylor expansion, we speculate the position and its derivatives at time $t + \delta t$, giving the position and its derivatives at the time t .

Calculation of inter-particle forces: In this step we calculate real total force that act on each particle i :

²In reality, it never happens

C_r	C_v	C_b	C_c
$G(0) \cdot C(2)$	$G(1) \cdot C(2)/C(1)$	$G(3) \cdot C(2)/C(3)$	$G(4) \cdot C(2)/C(4)$

Table 1.3: Coefficients of the corrector step.

$$f_i(t + \delta t) = \sum_j F_{ij} \quad (1.11)$$

Where f_i is the total force that acts on particle i at time $t + \delta t$, and $\sum_j F_{ij}$ is a sum on all neighbors j around particle i interacting by force F_{ij} . To give a feedback into the system, difference of the real acceleration and the predicted acceleration should be calculated.

$$\text{Feedback}_i = \Delta_i = f_i(t + \delta t)/m_i - a_i(t + \delta t) \quad (1.12)$$

If $\Delta_i = 0$ then we accept the extrapolated values and proceed to the next time step. For $\Delta_i \neq 0$, we correct the predicted values according to the Δ_i .

Corrector step: In order to correct the initial extrapolated solutions, the feedback quantity Δ_i is used as:

$$r_i = r_i + \Delta_i \cdot C_r. \quad (1.13)$$

$$v_i = v_i + \Delta_i \cdot C_v. \quad (1.14)$$

$$a_i = f_i/m_i. \quad (1.15)$$

$$b_i = b_i + \Delta_i \cdot C_b. \quad (1.16)$$

$$c_i = c_i + \Delta_i \cdot C_c. \quad (1.17)$$

The coefficients C_i are given by: while the Gear coefficients³ $G(i)$ equal:

To summarize the Gear method, a flowchart of the algorithm is sketched in Fig.1.6.

A major advantage of the Gear method in comparison with the other methods such as

³Please note that the Gear coefficients are different for different ODE's

$G(0)$	$G(1)$	$G(2)$	$G(3)$	$G(4)$
$\frac{19}{120}$	$\frac{3}{4}$	1	$\frac{1}{2}$	$\frac{1}{12}$

Table 1.4: The Gear coefficients for second order ODE's.

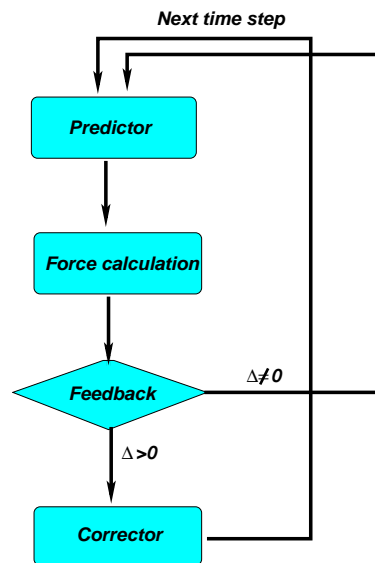


Figure 1.6: Flowchart of the 5th order Gear method illustrated.

Runge-Kutta method [62] is that one should calculate the the interparticle forces only once.

1.3.2 Accuracy of the Gear method for different interaction forces

In order to check the numerical accuracy of the Gear method, we explore the energy conservation in a gas of soft discs that interact via short range repulsive forces as described above. Fig.1.7 shows the standard deviation of the total energy of the system as a function of the time step Δt . We explore the energy conservation for both monodisperse and bidisperse discs in which the ratio of the radii is 1.4. The number of the particles is $N = 100$. They are equally distributed between large and small particles for the bidisperse case. The monodisperse and bidisperse particles are marked by M and B respectively. The interparticle forces are:

- **Schultz's potential**
- **Lennard-Jones (LJ)**
- **Non-linear spring** where the prefactor is set to $A = 10^3$
- **Hertz** where the prefactor is set to $A = 10^3$

For all systems the energy conservation is well observed. The fluctuations ΔE disappear like a power law with decreasing the time step Δt of the algorithm, $\Delta E \sim \Delta t^\gamma$. The exponent γ is noted in the graph. Furthermore, Fig.1.7 proves that the class of the spring forces, *i.e.* the Hertz or the nonlinear spring, are the most stable forces for this algorithm.

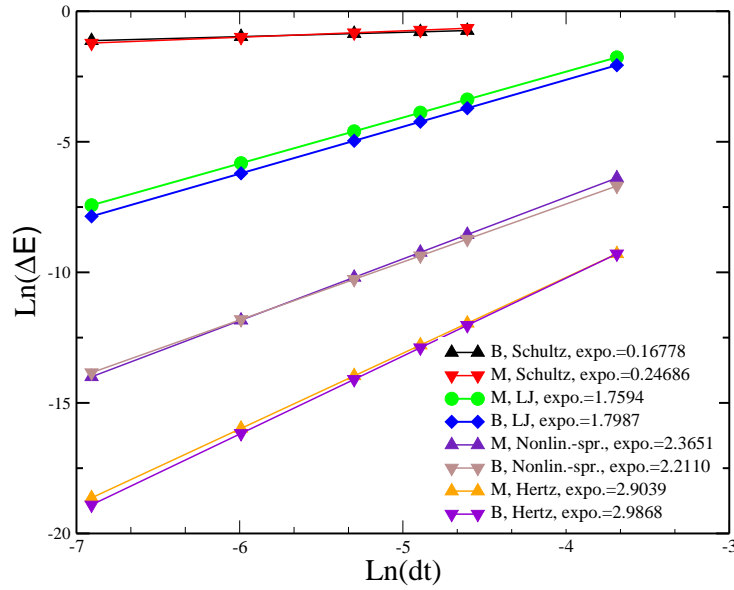


Figure 1.7: Logarithm of the average standard deviation of the total energy as a function of the logarithm of the time step dt . The simulation is done for both monodisperse and polydisperse discs. A power law scaling behavior is found. The corresponding exponent of each curve is written inside the graph.

Chapter 2

Stability of a granular pile

In this chapter we explore the stability of granular piles. One can prepare different kinds of granular piles based on the coordination number z of the particles. There are two main categories of granular piles [64, 65]:

1. **Isostatic pile:** The coordination number of each particle equals two times of the dimension of the system $z = 2d$.
2. **Hyperstatic pile:** The coordination number of each particle is greater than two times of the dimension of the system $z > 2d$.¹

Accordingly, in an isostatic pile of two dimensional monodisperse disks, the coordination number is 4. In a hyperstatic pile of such a system, the coordination number is greater than 4. The hexagonal arrangement of monodisperse disks is an example of a hyperstatic packing. If one make a regular gap between disks the pile will become a regular isostatic pile.

2.1 Motivation

We start with snapshots from simulation of a simple model for a dry isostatic pile consisting three layers of monodisperse disks (Fig.2.1). The brown disks (lowermost row) are immobilized in order to mimic a rough bed and the red disks are settled in the valleys between the brown disks resembling a hexagonal packing. There are regular gaps between disks given by δ and each disk has four neighbors. The disks are frictionless and interact via a nonlinear

¹Pouring frictional spheres into a vessel, often ends up with a hyperstatic packing.

spring force when they overlap. The snapshots are parts of a much longer pile in the direction parallel to the wall. The gravitational acceleration is $g = 1$, and the inclination angle is $\theta = 80^\circ$. Fig.2.1-bottom shows a snapshot of the pile configuration at time $t = 3.5$ where the pile is being fluidized. By that time all the red disks move simultaneously. Although the symmetry of the pile is conserved, and disks no longer touch each other.

Let's take exactly the same system as it is already described in Fig.2.1 and add capillary bridges at the contact points of disks in order to make the pile wet. In Fig.2.2 top-left a wet pile consisting of three layers and capillary bridges between them at $t = 0$ depicted. The gravitational acceleration is $g = 1$, and the inclination angle is $\theta = 80^\circ$. Fig.2.2 top-right shows a snapshot of the system at $t = 1.2$ where the pile started to move and the supporting capillary bridges in the deepest layer are significantly stretched. Fig.2.2 bottom-left the supporting capillary bridges ruptured such that each disk in the deepest layer keeps its contact with the brown disks only via a single capillary bridge. Fig.2.2 bottom-right is snapshot of the system at $t = 7$ where the pile is flying. Since some of disks in the middle layer have five contacts, isostaticity and periodicity of the pile are broken.

Accordingly, there is a dramatic difference between physics of a wet pile on an inclined plane and that of the dry pile. In a dry pile all layers of the pile fluidize simultaneously when the pile is tilted. In the wet case, the fluidization starts in the deepest layer. Why do wet piles break close to their support? Can one quantitatively predict fluidization threshold of wet piles?

2.2 Theoretical formalism

2.2.1 Critical angle

As explained above, we choose a pile in which there are regular gaps δ between adjacent disk in a layer. In Fig.2.3 we zoom in one of the red disk in the first layer. The disk is supported by two brown disks. Since disks are monodisperse, one can draw an isosceles triangle that connects the centers of the disks A, B, and C (the black triangle). The length of the sides of the triangle are $(2R, 2R + \delta, 2R)$ respectively. The critical angle θ_c is defined as half of the ABC cone, such that:

$$\sin \theta_c = \frac{R + 0.5\delta}{2R} \quad (2.1)$$

In the next section we will show that if an external force, *e.g.* gravity, acts on the red disk, it will not move and will be stable as long as the force points somewhere inside the ABC cone.

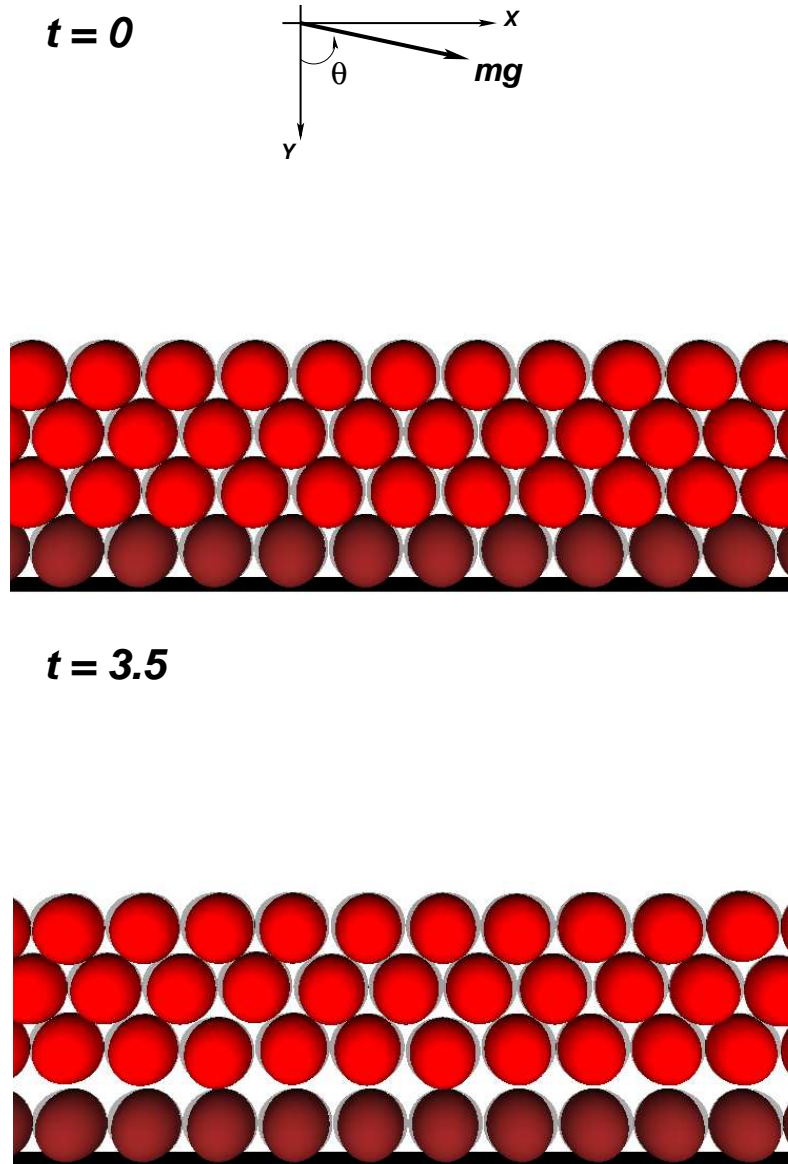


Figure 2.1: Snapshots taken from simulation of a dry isostatic pile on an inclined plane at different simulation times. The radius of each particle is $R = 0.5$, the mass of each disk is $m = \pi \cdot R^2$, the gravitational acceleration is $g = 1$, the regular gap is $\delta = 0.125$, and the inclination angle is $\theta = 80^\circ$.

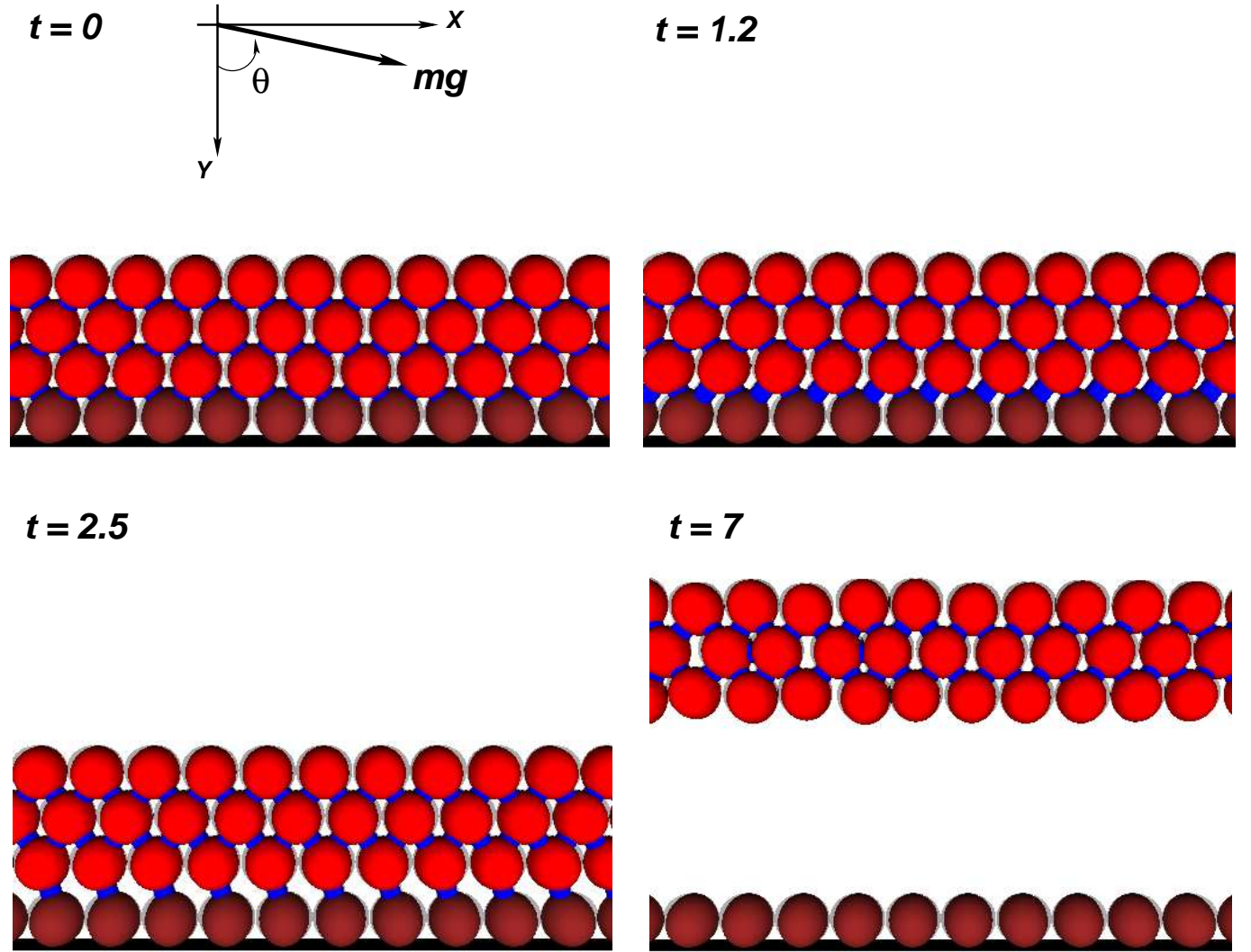


Figure 2.2: Snapshots taken from simulation of a wet isostatic pile on inclined plane at different simulation time. Radius is $R = 0.5$, the rupture separation is $S_c = 0.1$, the capillary bridge force is $f_{LB} = 1$, the mass of each disk is $m = \pi \cdot R^2$, the gravitational acceleration is $g = 1$, the regular gap is $\delta = 0.125$, and the inclination angle is $\theta = 80^\circ$.

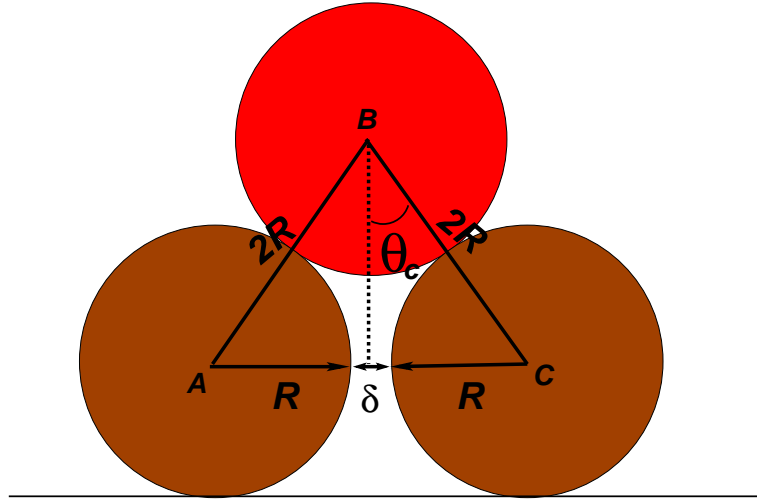


Figure 2.3: The critical angle θ_c in a system at which grains are separated from one another by a regular gap δ and disks in each layer sit in the valleys of the supporting disks.

2.2.2 Isostatic dry pile

Let's start with the simplest possible configuration for a pile of dry disks. Fig.2.4 shows sketch of a monodisperse pile in which the red disks are settled in valleys of the immobilized brown disks. The regular gap between disks in a row is δ , and the inclination angle is smaller than the critical angle $\theta < \theta_c$. There are three forces acting on each red particle as follows:

1. mg : the gravitational force
2. F_1 : the repulsive force from the right side supporting disk
3. F_2 : the repulsive force from the left side supporting disk

Because the direction of the inclination of the pile is normal to the plane, the right brown disk in Fig.2.4-top has to support more than the left one, thus $F_1 > F_2$. In order to have a static equilibrium in the pile, the forces acting on the red disks should balance:

$$\mathbf{F}_1 + \mathbf{F}_2 + m\mathbf{g} = 0 \quad (2.2)$$

If one projects equ.(2.2) into the parallel and vertical directions to the inclination plane:

$$\begin{cases} (F_1 + F_2) \cos \theta_c = mg \cos \theta \\ (F_1 - F_2) \sin \theta_c = mg \sin \theta \end{cases}$$

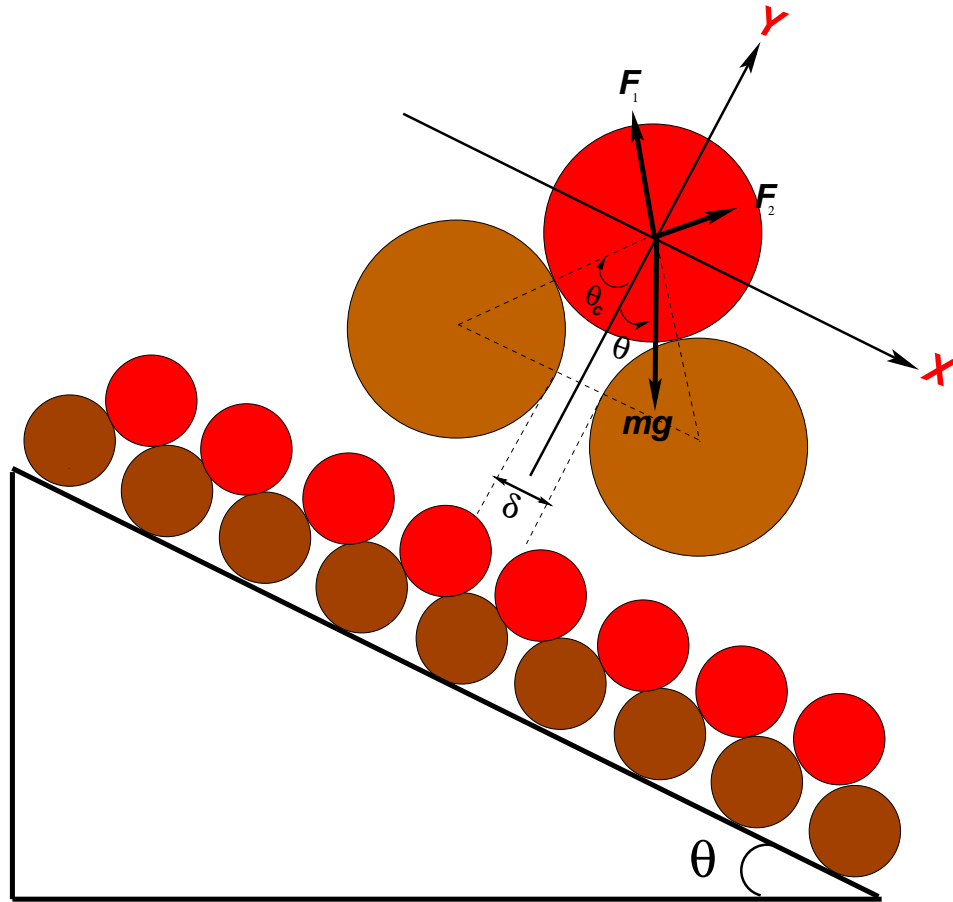


Figure 2.4: An isostatic pile of monodisperse dry disks on an inclined plane. The brown disks are immobilized and the red disks are settled in the valleys of the brown disks. A regular gap δ between disks in each row is implemented to make an regular isostatic packing. The inclination angle is smaller than θ_c .

one can calculate F_1 and F_2 as a function of the gravity and the inclination angle:

$$\begin{cases} F_1 = mg \sin(\theta_c + \theta) / \sin 2\theta_c \\ F_2 = mg \sin(\theta_c - \theta) / \sin 2\theta_c \end{cases}$$

This shows that as $\theta \rightarrow \theta_c$, F_1 increases and F_2 decreases and approaches zero. At $\theta = \theta_c$ the left side brown disk no longer supports $F_1 = 0$, and the right side brown disk fully supports the weight of the red disk $F_2 = mg$.

$$\begin{cases} F_1 = mg \\ F_2 = 0 \end{cases}$$

Due to periodicity of packing in X-direction, this picture is true for all the red disks in the first layer. Therefore, at $\theta = \theta_c$ the system is at vicinity of the fluidization. In conclusion, one sees that the critical angle θ_c is related to stability of the pile, *i.e.* for $\theta < \theta_c$ the pile is stable and for $\theta > \theta_c$ the pile fluidizes.

Let us consider a similar pile with an arbitrary large number of layers. Each particles in a layer is settled in the valley of two supporting disks in the lower layer. In the bulk of the pile, each particle has four contacts with the surrounding disks.

Fig.2.5 shows the forces acting on the red disk at the center. There are four repulsive forces acting on the red disk as well as the gravitational force. In the static equilibrium all forces should balance as:

$$\mathbf{F}_1 + \mathbf{F}_2 + \mathbf{F}_3 + \mathbf{F}_4 + mg = 0 \quad (2.3)$$

The angles of $\mathbf{F}_1, \mathbf{F}_2, \mathbf{F}_3$, and \mathbf{F}_4 with a line vertical to the inclined plane are $\theta_c, \pi - \theta_c, \pi + \theta_c$, and $-\theta_c$. Consequently the projection of equ.(2.3) into the parallel and vertical directions to the inclination plane are:

$$\begin{cases} (F_1 - F_3 + F_2 - F_4) \cos \theta_c = mg \cos \theta \\ (F_1 - F_3 - (F_2 - F_4)) \sin \theta_c = mg \sin \theta \end{cases}$$

Lets suppose $F' = F_1 - F_3$ and $F'' = F_2 - F_4$:

$$\begin{cases} (F' + F'') \cos \theta_c = mg \cos \theta \\ (F' - F'') \sin \theta_c = mg \sin \theta \end{cases}$$

Then:

$$\begin{cases} F' = mg \sin(\theta_c + \theta) / \sin 2\theta_c \\ F'' = mg \sin(\theta_c - \theta) / \sin 2\theta_c \end{cases}$$

and if $\theta = \theta_c$:

$$\begin{cases} F' = mg \\ F'' = 0 \end{cases}$$

the critical fluidization point θ_c does not change as one increases the number of layers. For $\theta > \theta_c$ there is a force $F_2 - F_4$ acting away from the wall, which triggers fluidization.

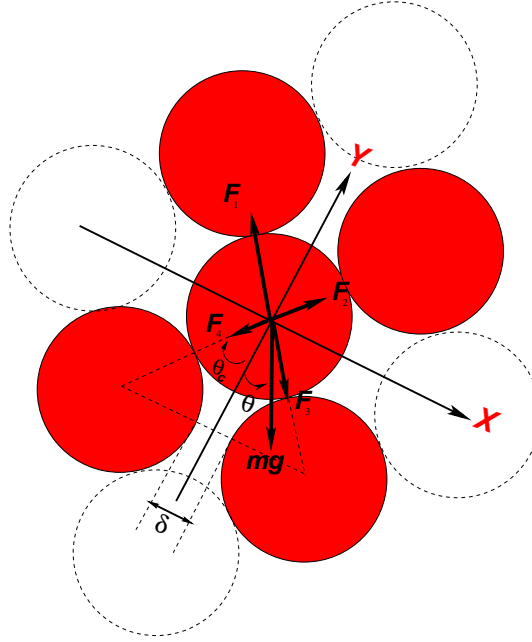


Figure 2.5: Forces acting on each disk in bulk of a pile consisting an arbitrary large number of layers depicted. The inclination angle is smaller than θ_c .

In conclusion, we analytically showed that fluidization of a dry pile occurs if the inclination angle exceeds the critical angle θ_c . Note that the fluidization point is independent from two physical parameters:

1. The number of the layers in the pile.
2. The gravitational acceleration.

This means that for $\theta < \theta_c$ the pile does not fluidize irrespective of the strength of the gravitational acceleration. On the other hand, for $\theta > \theta_c$ the pile fluidizes for any arbitrary gravita-

tional acceleration. In the next section, we will show that this picture completely changes for a wet pile.

2.2.3 Isostatic wet pile

To study stability of a wet pile we start again with the simplest possible isostatic pile of monodisperse disks. Fig.2.6 shows a sketch of the system consisting of one layer of monodisperse disks prepared on a layer of immobilized brown disks. There are capillary bridges at the contact points of the disks. δ is the gap between disks in each layer. Due to support of the capillary bridges at the contact points of the disks, the pile will still be stable if the inclination angle exceeds θ_c . For $\theta > \theta_c$ the repulsive force at equ.(2.2) can be substituted by an attractive force f coming from the supporting capillary bridge (Fig.2.6).

If in equ.(2.2) one substitutes F by F_2 and f by F_1 , at the vicinity of the fluidization where $g = g_c$, those three forces should balance:

$$\mathbf{f} + \mathbf{F} + m\mathbf{g}_c = 0 \quad (2.4)$$

leading to the following:

$$g_c = \frac{f}{m} \cdot \frac{\sin(2\theta_c)}{\sin(\theta - \theta_c)} \quad (2.5)$$

Therefore, for a given capillary bridge force, there is a corresponding critical gravitational acceleration which makes the capillary bridge unstable, and the fluidization is caused by rupturing of such an unstable capillary bridge. In order to understand the equ.(2.5), we notice that $mg_c \cdot \sin(\theta - \theta_c)$ is a force that pulls the disk out in the direction normal to the line that connects the red disk to the supporting disk at the right side. Accordingly, equ.(2.5) gives rise to a reasonable scaling law that can be understood by the physical intuition.

Now the next question is that what happens if one adds more layers of the red disks? Since the repulsive force from the brown disks increases linearly with the number of the red layers, to balance equ.(2.4) mg_c should decrease. We expect that the critical gravitational force is proportional to the inverse of the number of layers l :

$$g_c = \frac{f}{l \cdot m} \cdot \frac{\sin 2\theta_c}{\sin(\theta - \theta_c)} \quad (2.6)$$

It implies that the critical gravitational acceleration that makes the capillary bridges unstable, decreases as one approaches to the lowermost layer. Accordingly, this shows that a wet pile

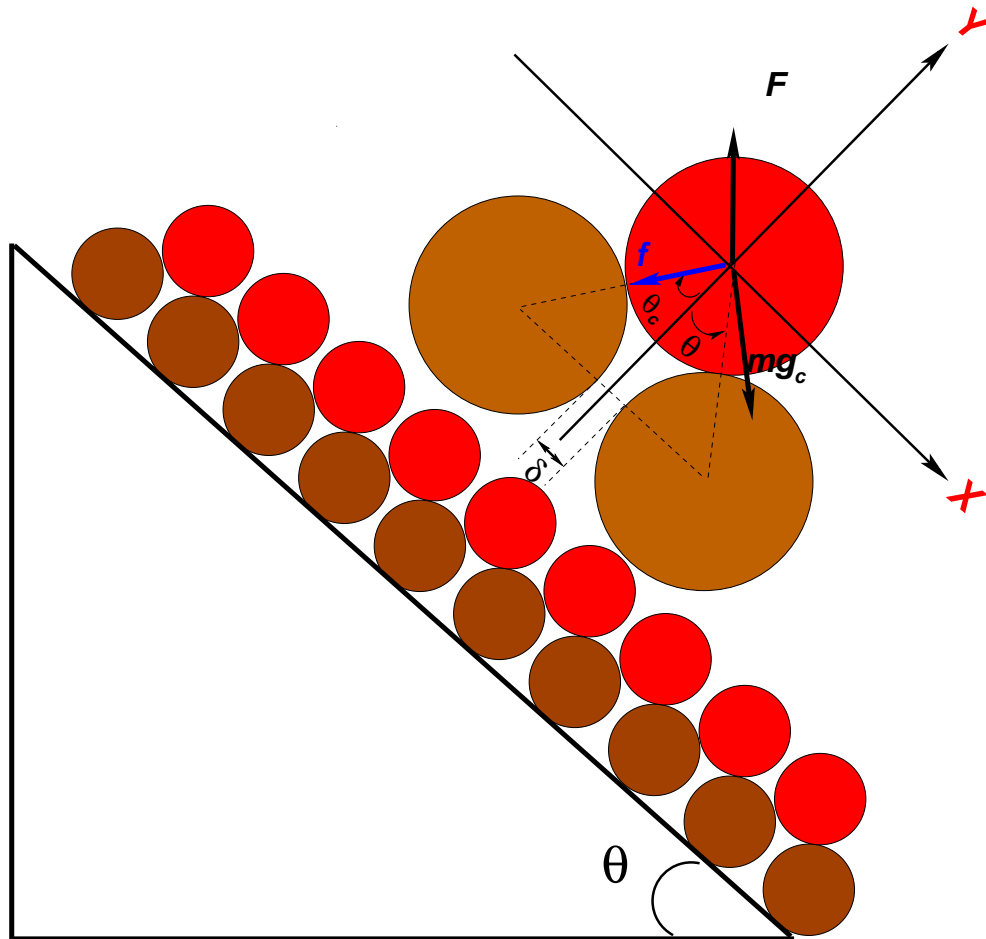


Figure 2.6: The brown disks are glued to the bottom in order to apply non-slip boundary condition. At the vicinity of the fluidization, there are three forces acting on each red disk that should balance. An attractive force from the supporting capillary bridge f , a repulsive force from the supporting disk, and the gravitational force of the golden disk. θ is the inclination angle, and θ_c is the critical angle.

yields in the bulk close to the wall. However, in a dry pile, usually particles on the surface of a pile are subject to move. This result completely changes our way of thinking about fluidization of granular piles. We will check the equ.(2.6) by extensive numerical simulations in the following sections.

In conclusion, the fluidization in a wet granular pile is caused by pinching off the capillary bridges in deepest layer. In contrast, in a dry pile fluidization occur simultaneously in all the layers of the pile as soon as the critical angle is exceeded. One sees that the fascinating aspect of capillary bridges in a granular pile is not only that one can sculpture a statue, but it gives rise to a fundamentally different physics that can be applicable to our understanding of avalanches and landslides.

2.3 Numerical simulations of monodisperse disks

2.3.1 An isostatic wet pile

In the previous section, we presented a theoretical model to describe the stability of a wet isostatic pile. In the current section, we check this model by numerical simulations. Fig.2.7-left depicts the fluidization threshold for one, two, and three layers of monodisperse disks for a pile with $\theta_c = 34.22^\circ$. The red, blue, and violet lines show the theoretical prediction and the solid points are the corresponding simulation data. We find an excellent agreement of the theoretical prediction and the simulation data. To show the deviations of the simulation data from the theoretical line, one may move all the parameters in equ.(2.6) to one side as:

$$\frac{\sin(\theta - \theta_c)}{\sin 2\theta_c} mg_c = \frac{1}{l} \quad (2.7)$$

where l is number of the layers. The right hand side of equ.(2.7) is a constant number independent from the tilting angle. Therefore, if one plots the left hand side of equ.(2.7) for each inclination angle one can have a chance to see the deviations of the simulation data from the theory. Fig.2.7-right shows $\sin(\theta - \theta_c)\sin 2\theta_c mg_c$ versus the inclination angle. For one, two, and three layers the theory predicts 1, 0.5, and 0.3333. One sees that deviations of the simulation data from the theoretical lines are indeed very small.

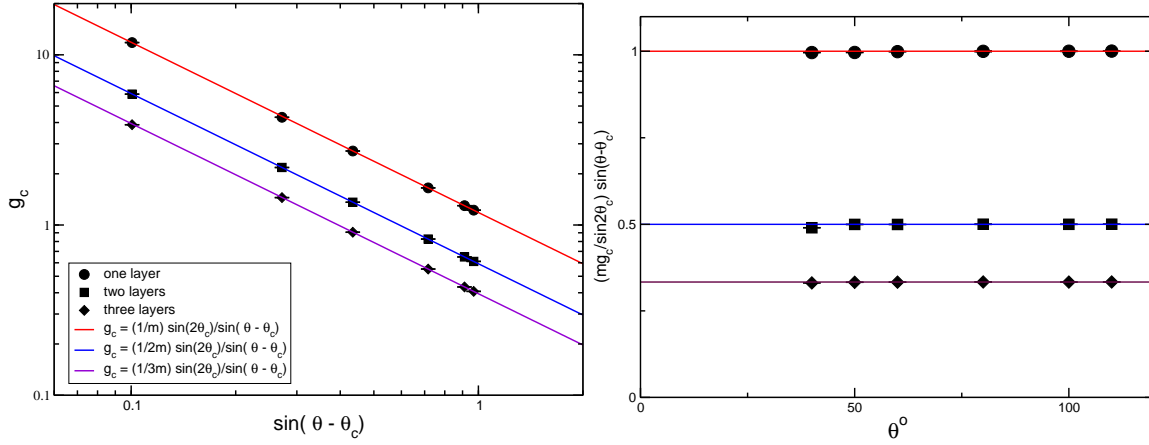


Figure 2.7: Fluidization threshold of a wet isostatic pile consisting one, two, and three layers of monodisperse disks. The solid points show the simulation data, and the solid lines show the theoretical prediction. We find a perfect agreement of the simulation data and the theory. The radius of each particle is $R = 0.5$, the rupture separation is $S_c = 0.01$, the capillary bridge force is $f_{LB} = 1$, the critical angle is $\theta_c = 34.22^\circ$, the regular gap is $\delta = 0.125$, the system size $L = 18$, and the mass of each disk is $m = \pi \cdot R^2$.

2.3.2 An isostatic wet pile with height disorder

In this section, we introduce disorder in the system and study its influence on the fluidization threshold. One of the easiest ways to implement disorder in the system is by breaking the translational invariance of the system. To that end, we add a single disk on top of the pile and study its influence on the fluidization threshold. Fig.2.8-top shows the sketch of the system consisting of three complete layers as well as one single disk on top of the pile. Each layer has 16 disks with regular gaps $\delta = 0.125$. Surprisingly, the simulation data in Fig.2.8-bottom for the fluidization threshold lie perfectly on the theoretical line for 4 complete layers. Therefore, when the pile is isostatic whether one adds a single disk on top of the pile or one fills up the whole layer, the fluidization threshold shifts to a one higher layer. Adding a single disk on top of an inclined isostatic pile can trigger fluidization. The explanation for this observation is straightforward. *The pile yields at the point where 4 disks are pulling.*

In order to increase the disorder in the system, we make an isostatic pile with a complicated height profile. A sketch of the system depicted in Fig.2.9-top.

One sees that the system consists 6 complete layers as well as 2 incomplete layers, and there are regular gaps between disks $\delta = 0.125$. The 7th incomplete layer has two holes, and 8th incomplete layer is just a single disk. If our observation in Fig.2.8 holds in general, one

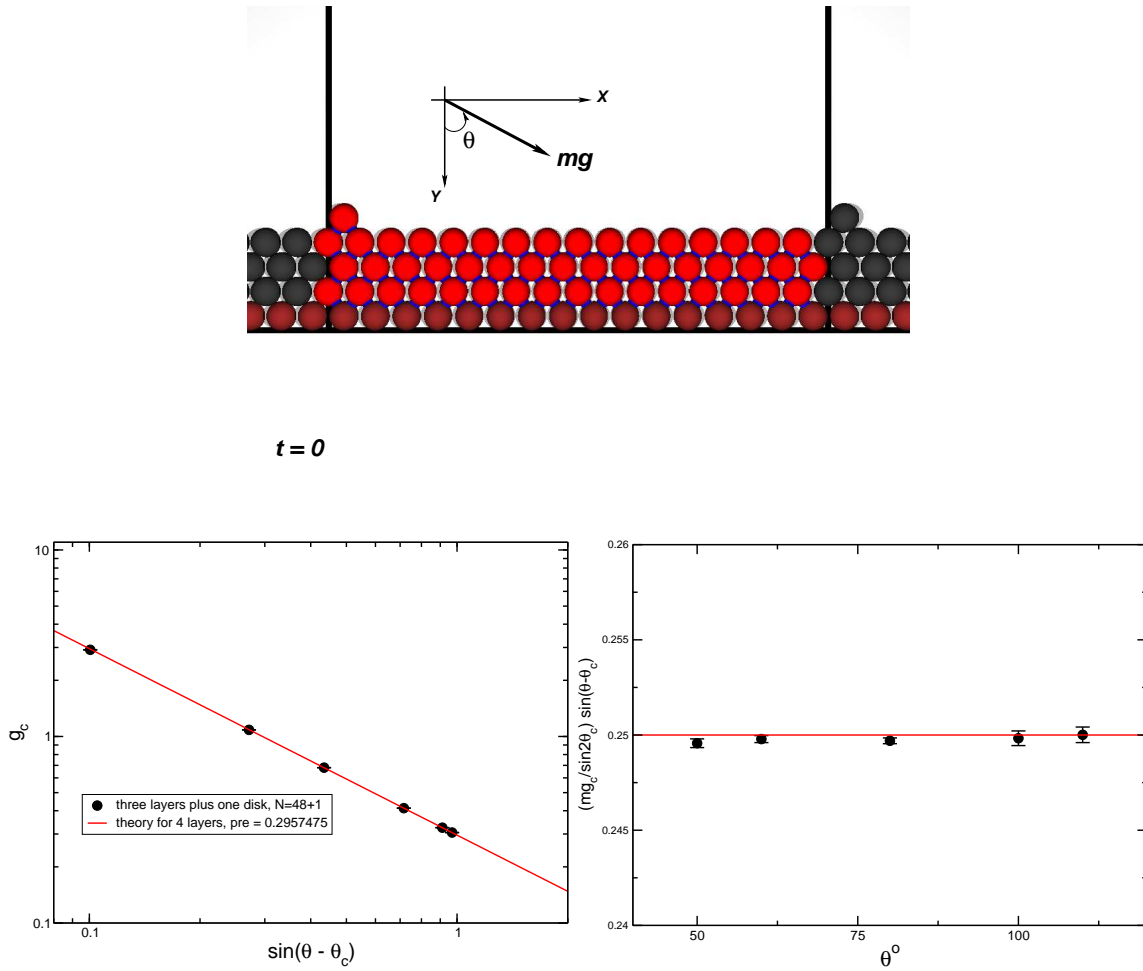


Figure 2.8: Fluidization threshold of an isostatic pile consisting 3 complete layers as well as a single disk on top of it depicted. The black circles are the simulation data and the red line shows the theoretical prediction for 4 complete layers. The deviations are due to the thermal motion of particles. The radius of each particle is $R = 0.5$, the rupture separation is $S_c = 0.01$, the capillary bridge force is $f_{LB} = 1$, the critical angle is $\theta_c = 34.22$, the regular gap $\delta = 0.125$, and the mass of each disk is $m = \pi \cdot R^2$.

should expect that the fluidization threshold of this system lies on the fluidization threshold of 8 complete layers. In Fig.2.9-middle the fluidization threshold of the system is presented. The black circles, which are the simulation data, lie on the theoretical prediction for 8 complete layers. One can see the deviations from the theoretical line more clearly in Fig.2.9-bottom where the theory predicts a horizontal line at height $1/8$. The compressibility of the system results to thermal motion of particles when the gravitational force acts, and the thermal motion entails the deviations of the simulation data from the theoretical prediction. This example proves that Fig.2.8 is not an exceptional case. For isostatic packings adding a single disk on top of a complete layer has the same effect as adding a complete layer. The fluidization threshold of both cases will be identical.

2.3.3 A hyperstatic wet pile

When the coordination number in a two dimensional packing of monodisperse disks is greater than 4 the packing is hyperstatic [64]. Since each particle in a hyperstatic packing has more than 4 contacts, the force distribution in a hyperstatic packing becomes more sophisticated than the force distribution in a static packing. Does the force distribution caused by configuration of the pile affect the stability of the pile? To answer that question, we make initially a hyperstatic pile by setting the gap between disks to zero and study the fluidization threshold in the pile. While the gap between disks in each row is zero the number of the contacts for each particle in the bulk will be 6 such that the pile is hyperstatic.

Fig.2.10-left shows the critical gravitational acceleration versus sine of the subtracted inclination angle, *i.e.* $\sin(\theta - \theta_c)$, in which the radius of each particle is $R = 0.5$, the rupture separation is $S_c = 0.01$, the liquid bridge force is $f_{LB} = 1$, and the mass of each disk is $m = \pi \cdot R^2 = 0.7853$. The black circles show the simulation data of the fluidization threshold for one layer of the wet disks, and the red line is the corresponding theoretical prediction. Subsequently, the black squares and black diamonds are the fluidization points for two and three layers respectively. The blue and violet lines are the corresponding theoretical lines. Although in the theory for stability of a wet pile it is supposed that the pile is isostatic, we still find a perfect agreement between the theoretical prediction for a isostatic pile and the numerical simulations for a hyperstatic pile. Fig.2.10 proves that our simple picture of the balanced forces at the vicinity of the fluidization might also be useful to predict the fluidization threshold of a hyperstatic wet pile in different inclination angles. When the pile is translationally invariant, the forces acting on each particle in a row from its neighbors at the same row do not affect the

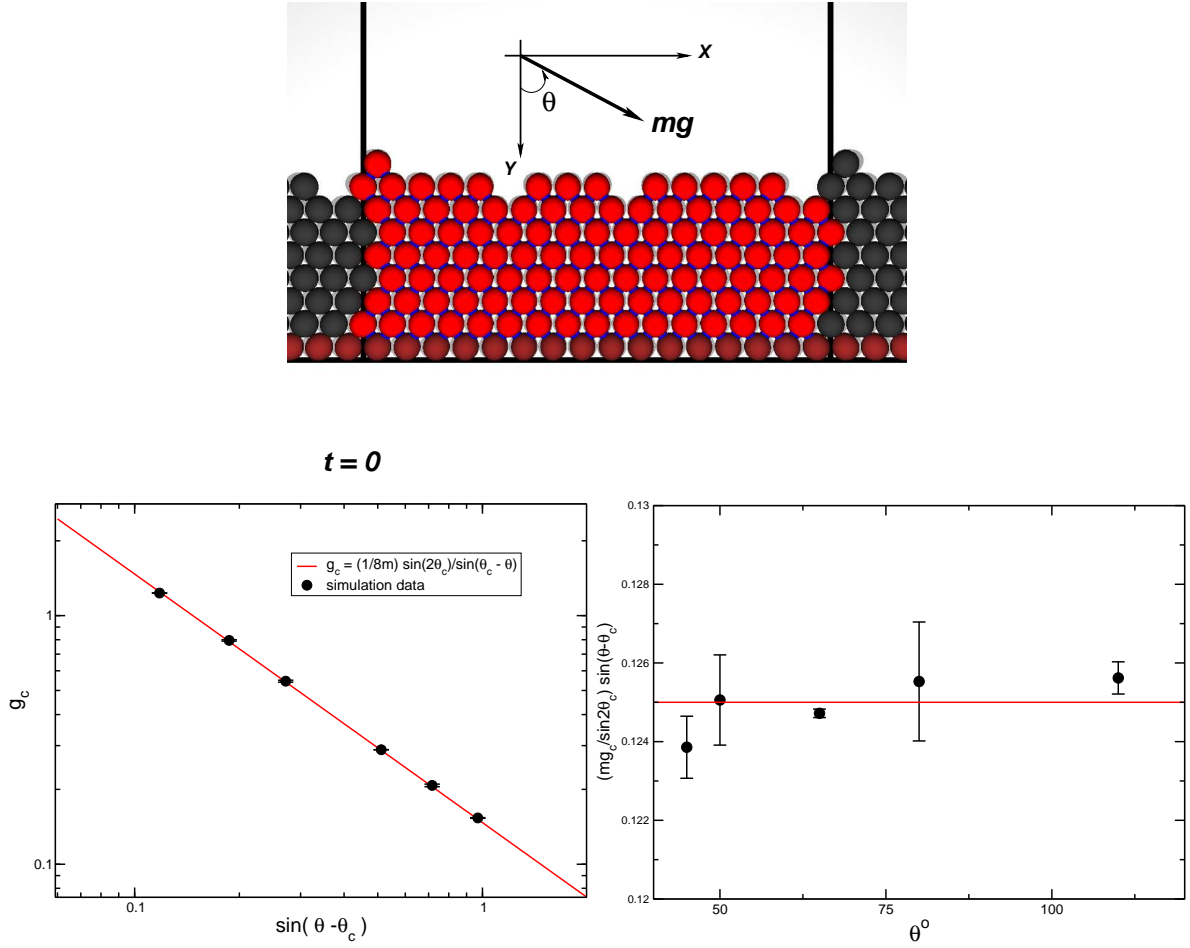


Figure 2.9: Fluidization threshold of 8 incomplete layers in an isostatic pile. The black circles are the simulation data for the system and the red line is the theoretical prediction for 8 complete layers. The radius of each particle is $R = 0.5$, the rupture separation is $S_c = 0.01$, the capillary bridge force is $f_{LB} = 1$, the critical angle is $\theta_c = 34.22$, and the mass of each disk is $m = \pi \cdot R^2$.

stability of that grain.

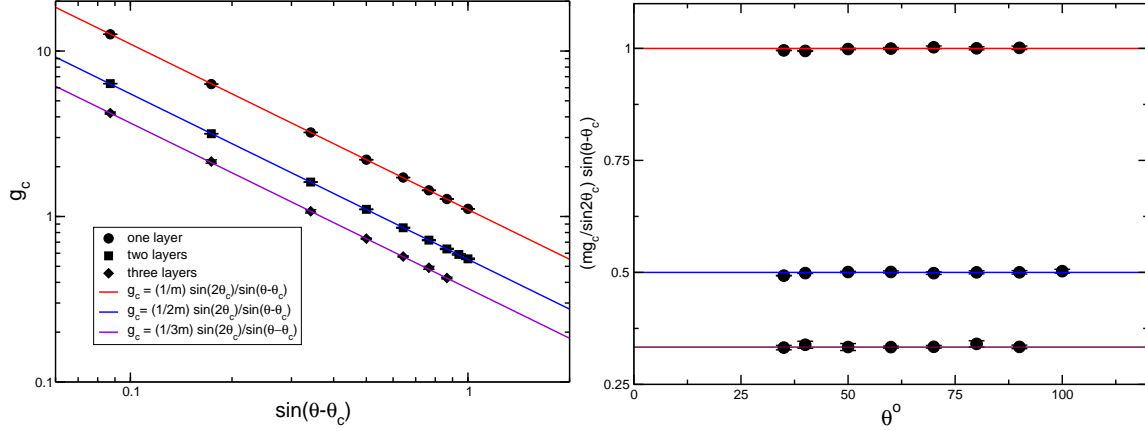


Figure 2.10: Fluidization threshold for one, two, and three layers of the wet disks in a hyperstatic wet pile. The solid points show the simulation data, and the solid lines show the theoretical prediction. The radius of each particle is $R = 0.5$, the rupture separation is $S_c = 0.01$, the capillary bridge force is $f_{LB} = 1$, the critical angle is $\theta_c = 30^\circ$, and the mass of each disk is $m = \pi \cdot R^2 = 0.7853$.

2.3.4 A hyperstatic wet pile with height disorder

We showed that in a hyperstatic pile with translational invariance the simulation data, corresponding to the fluidization of the pile, sit on top of the theoretical prediction for an isostatic pile. By adding one single disk on top of the pile we break the translational invariance and explore whether the simulation data fit on the theoretical curve of $l + 1$ layers. We choose $l = 3$ and add one single disk on top of the pile. Fig.2.11-left shows the fluidization threshold of the system. The solid circles illustrate the simulation data and the red line is the theoretical prediction for only 3 complete layers. In Fig.2.11-right one sees that the simulation data are slightly below the transition line for three layers. Thus, in a hyperstatic pile without translational invariance, the additional contacts tend to support the particles and make the pile more stable. The stability threshold remains close to the value for 3 layers rather than threshold for 4 layers.

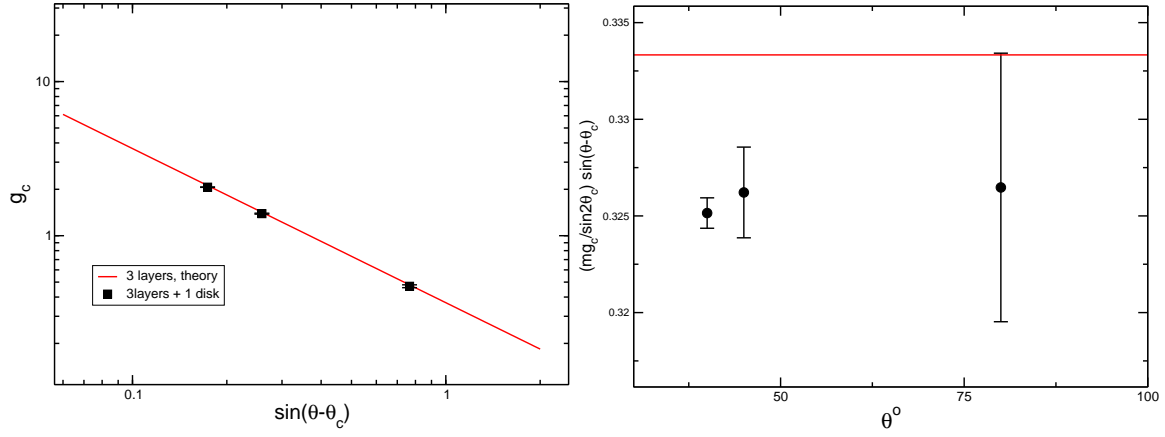


Figure 2.11: Fluidization threshold of a hyperstatic pile consisting of 3 layers as well as one single disk on top of the pile. The black circles show the simulation data, and the red line depicts the theoretical prediction for three layers. The radius of each particle is $R = 0.5$, the rupture separation is $S_c = 0.01$, the capillary bridge force is $f_{LB} = 1$, the critical angle is $\theta_c = 30$, and the mass of each disk is $m = \pi \cdot R^2 = 0.7853$.

2.3.5 Rupture length and stability of a wet pile

Our theoretical considerations on the stability of a wet pile are based on the balance of the forces of each disk in the pile with its supporting disks. The rupture separation of the capillary bridges, which is related to the energy considerations, should not affect the fluidization threshold. To check that fact we performed numerical simulations for ten different rupture separations $S_c = \{0.01, 0.02, 0.03, \dots, 1.0\}$. Fig. 2.12 shows the fluidization threshold of an isostatic wet pile consisting of one, two, and three layers depicted by the red, blue, and brown colors respectively for two different rupture separation $S_c = \{0.01, 0.1\}$. We plotted $mg_c \sin(\theta - \theta_c) / \sin 2\theta_c$ versus θ . The data corresponding to $S_c = 0.1$ are shifted by 90° . For one layer $mg_c \sin(\theta - \theta_c) / \sin 2\theta_c = 1$ and simulation data for $S_c = \{0.01, 0.1\}$ illustrated by the circles and squares respectively. One sees that both data sets lie on the theoretical curve (the red curve). For two and three layers also the data sets corresponding for two different S_c lie on the theoretical lines. In conclusion, the rupture separation does not change the stability of a regular pile.

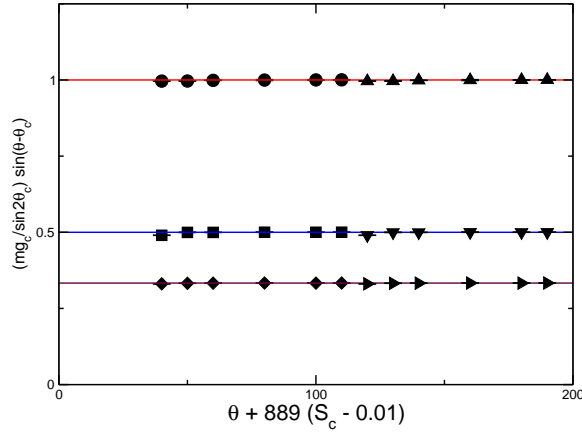


Figure 2.12: Fluidization threshold for one, two, and three layers of an isostatic pile for two different rupture separations $S_c = \{0.01, 0.1\}$. The data corresponding to $S_c = 0.1$ are shifted by 90° . The Y axis is $mg_c \sin(\theta - \theta_c) / \sin 2\theta_c$ and the X axis is θ . The solid symbols show the simulation data and the solid lines show the theoretical line. The radius of each particle is $R = 0.5$, the rupture separation is $S_c = 0.01$, the capillary bridge force is $f_{LB} = 1$, the critical angle is $\theta_c = 34.22^\circ$, and the mass of each disk is $m = \pi \cdot R^2 = 0.7853$.

2.4 Numerical investigations of the stability of bidisperse piles

In the previous section, we started with the simplest possible configuration of a granular pile, *i.e.* monodisperse disks in an isostatic and hyperstatic packing. Step by step by adding a few disks on top of the pile we introduced disorder in the system. In the present section, we consider a much more disordered pile consisting of bidisperse disks. In order to avoid crystallization, we use bidisperse disks with a ratio of radii equal to 1.4. The material properties of dry bidisperse disks have been studied by O’Hern’s group [66] and this type of the systems have been accepted as a standard system for bidisperse spheres in which crystallization and segregation do not occur. The bidisperse soft disks interact via two forces. A non-linear repulsive spring force acts between two disks when they overlap. The particles are wet and we use the minimal capillary force to model the capillary interactions.

2.4.1 Preparation step

Since one can not simply calculate the initial positions of a bidisperse system in a densely packed state, one needs a preparation step. To prepare a dense packing we use a two step procedure:

1. **Random sequential addition:** in each step, a new disk is added at a random position into the box. The new disk is accepted if it does not overlap with the other disks, otherwise it is rejected. Adding new disks will stop once the number of particles reaches the desired amount. We enforce a restriction that the number of the small disks should be equal to the number of large ones².
2. **Sedimentation:** a vertical force acts on each particle. A viscoelastic force is used to dissipate the injected energy by gravity.

After the sedimentation step, the disks touching the bottom layer are immobilized. Periodic boundary conditions are used in horizontal direction.

2.4.2 Protocol of the numerical simulation

We use the units of the simulation as outlined in chapter 1, section 1.2.4. The initial sample is prepared during the sedimentation time $t_{sed.} = 200$, at which a linear drag force as outlined in chapter 1, section 3.2, is applied.

At the end of the preparation interval, the sedimented disks do not move.

Time	Description
Equilibration $0 < t < 67$	$g = 0, \theta = 0, b = 0$
Sedimentation $67 < t < 133$	$g \neq 0, \theta = 0, b = 0.5$
Sedimentation $133 < t < 200$	$g \neq 0, \theta = 0, f_{LB} = 1, b = 0.5$
Inclination $t > 200$	$g \neq 0, \theta \neq 0, f_{LB} = 1, b = 0$
Measurements $t > 1000$	$g \neq 0, \theta \neq 0, f_{LB} = 1, b = 0$

Table 2.1: The total simulation time is divided into several time intervals to prepare the initial state and to measure the physical parameters. The number of particles is $N = 200$.

After sedimentation of the disks, we tilt the gravitational force. Depending on the rupture separation S_c , there is a well defined critical gravitational force above which the material

²In order to avoid crystallization, the number of the large and small disks should be equal.

yields (fluidized state). After a relaxation time, the system reaches a dynamical stationary state which will further be characterized (chap.3).

2.4.3 Critical angle of a bidisperse dry pile

In order to calculate the critical angle, after the preparation procedure we tilt the gravitational force, and we measure the critical angle above which the center of mass of the system runs away. When the capillary bridges are switched off, no capillary force are acting. Thereby the critical angle should not depend on the gravitational acceleration. Fig.2.13 shows how we track center of the mass of the system in order to determine whether it runs away. The initial position of the center of mass should be around $(X = 9, Y = 9)$. At the sedimentation period the center of mass goes down (the red curved arrow shows the direction). At the end of the sedimentation the center of mass reached $(X \approx 9, Y \approx 5)$. The gravitational acceleration at the sedimentational step is $g_{sed.} = 0.3$ which makes enough pressure to prepare a densely packed pile. Afterwards the gravitational acceleration is decremented to $g = 0.15$ and simultaneously it is tilted. The inclination angle, *i.e.* angle between the gravitational force and normal vector of the plane, is $\theta = 4^\circ$. Because the vertical component of the gravitational acceleration is smaller than $g_{sed.}$, *i.e.* $g \cos 4^\circ < g_{sed.}$, the center of mass moves a little up after the sedimentation step. Although the pile is not fluidized, the center of mass moves in the horizontal direction until it stops at about $(X = 6.065, Y = 9.8)$. The inset, which is a blow up around the final position of the center of mass, shows that the center of mass jiggles around and does not run away. Therefore, in this configuration, $\theta = 4^\circ$ is below the critical angle. By incrementing the inclination angle θ to a slightly larger angle, one can calculate the border between the jiggling and runaway of the center of mass which marks the critical angle.

The initial configuration of particles at the first step of the preparation procedure, *i.e.* the random sequential addition, can be changed by the seed of the random number generator in the program. Accordingly, by changing the seed, the configuration of the immobilized particles at the bottom layer will be also changed. On the other hand, each configuration is related to a certain critical angle θ_c . In Fig.2.14 we show the cumulative probability of the critical angle θ_c calculated for simulations on 20 different configurations. We probe angles between $0^\circ < \theta < 10^\circ$, and that interval is divided to 50 equidistance intervals $\delta\theta = 0.2^\circ$. The red and blue colors show the cumulative probability for 200 and 300 disks respectively. In both cases, the critical angle lies almost certainly between $4.2^\circ < \theta_c < 8.6^\circ$, and maridian of the probability for both curves lies at $\theta_c^{max.} = 5.8^\circ$. Hence, the critical angle of the system does not

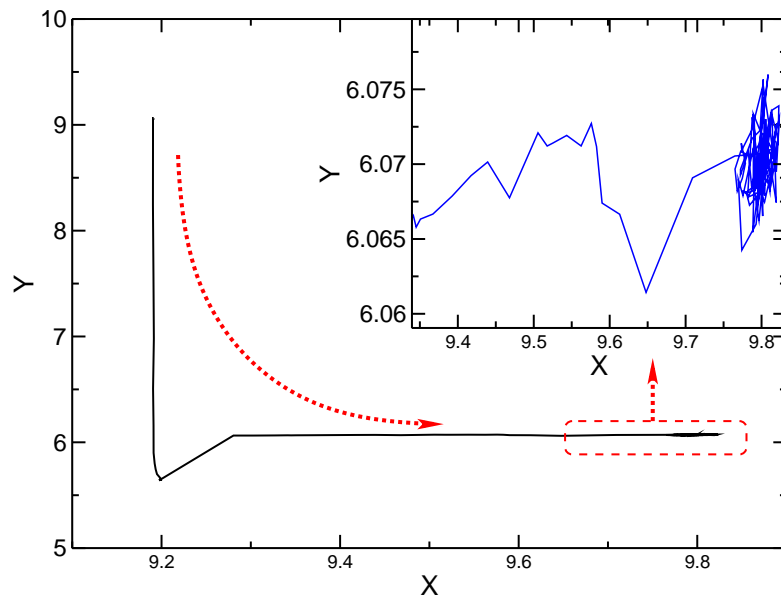


Figure 2.13: Path of the center of mass of the system. The inclination angle is $\theta = 4^\circ$, the gravitational acceleration is $g = 0.15$, the number of disks is $N = 200$, the system size is $L = 18$, and the capillary force is $f_{LB} = 0$. The inset shows how the center of mass jiggles around at the final position.

change when one increases the number of the disks in the system. This shows that this angle is again a universal parameter which is independent of the number of particles.

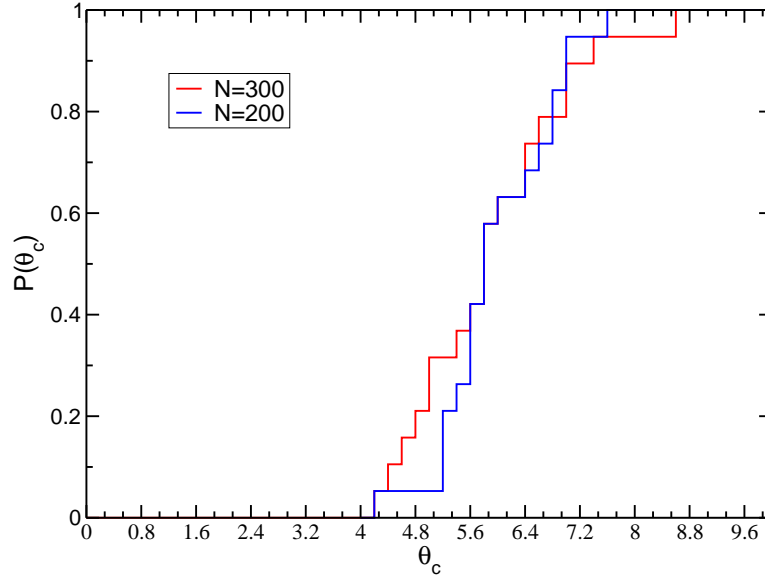


Figure 2.14: Cumulative distribution function of the critical angle θ_c . The red and blue curves correspond to $N = 200$ and $N = 300$.

In conclusion, the center of mass of the system of dry disks on inclined plane has two possibility:

1. **Run away:** it runs away and shows that the inclination angle is larger than the critical angle.
2. **Jiggling:** after a little shift of the center of mass, it jiggles around and does not runaway. This tells us that the inclination angle is smaller than the critical angle.

This observation in dry bidisperse disks, has a very important consequence for the fluidization threshold when the capillary bridges are added. Fluctuation in the system, caused by jiggling of the center of mass, injects a small amount of granular temperature in the system. Therefore, the pile can gain a little granular temperature before the fluidization, and the fluidization threshold of the pile will depend not only on the balance of the forces, but it will depend on the granular temperature as well. If that granular temperature is close to the bound energy, *i.e.* capillary bridge energy $f_{LB} \times S_c$, the pile will fluidize.

2.4.4 Stability of a wet bidisperse pile

In the previous section, we presented measurements on the the critical angle of a pile consisting of bidisperse disks. These information enable us to explore the fluidization threshold of the wet pile. Fig.2.15-top shows the the fluidization transition line of 200 bidisperse disks for 9 different initial configuration. The rupture separation is $S_c = 0.01$. Similar to the measurements on the monodisperse piles, the vertical axis shows the critical gravitational acceleration g_c at which the pile fluidizes and the horizontal axis is the sine of the inclination angle subtracted from the corresponding critical angle. Since each initial configuration is related to a corresponding critical angle, there will be a different fluidization threshold for each critical angle. That is why one sees 9 different simulation data set with different θ_c . A solid black line is drawn to show that g_c scales with $1/\sin(\theta - \theta_c)$, which is similar to the scaling behavior of the fluidization threshold of monodisperse system. The simulation data scatter at small inclination angles, close to the critical angle.

Fig.2.15-bottom shows the fluidization threshold for the same system, except the rupture separation is increased to $S_c = 0.1$. As anticipated in the previous section, the rupture separation in a bidisperse pile can influence the fluidization threshold. The stability of a bidisperse pile increases upon increasing the rupture separation, and the critical gravitational acceleration scales with the inverse sine of the inclination angle subtracted from the the critical angle:

$$g_c \sim \sin(\theta - \theta_c)^{-1} \quad (2.8)$$

So far, we explained quantitatively and qualitatively how piles of wet disks consisting of monodisperse and bidisperse disks respectively fluidize. We showed that adding the disorder to the system, by either considering monodisperse piles that are not translationally invariant or considering bidisperse piles, the critical gravitational acceleration scales with inverse of sine of the subtracted inclination angle. This scaling appears to be a universal scaling. It does not depend on details of the configuration of the pile.

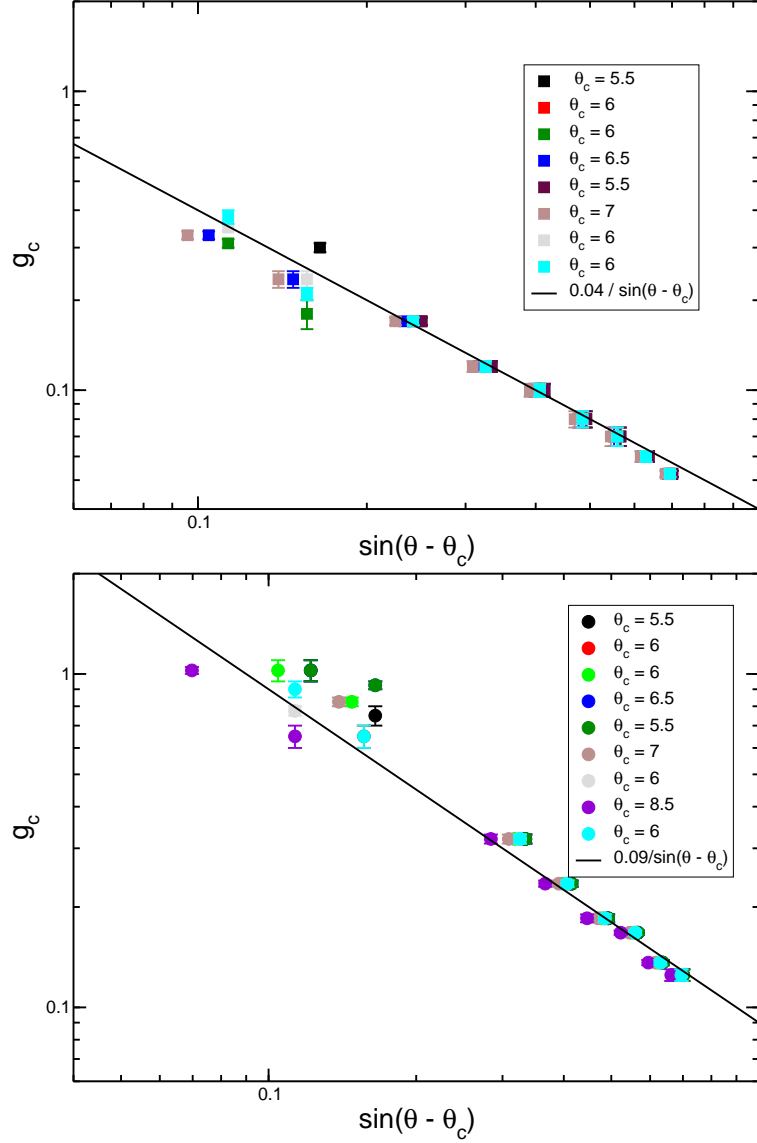


Figure 2.15: The critical gravitational acceleration versus sine of the reduced inclination angle for 9 different critical angles. Top: the fluidization threshold of 9 different critical angles corresponding 9 different configurations for rupture separation $S_c = 0.01$. Bottom: the fluidization threshold of 9 different critical angles corresponding 9 different configurations for rupture separation $S_c = 0.1$. The number of disks is $N = 200$, the average mass is $m = 0.875$, and the system size is $L = 18$.

Chapter 3

Wet disks running down an inclined plane

In the following chapter, we study flow properties of wet bidisperse disks running down on an inclined plane. In the absence of a top wall, such a system never reaches a steady state. It shows a runaway towards a gassy state with ever increasing kinetic energy. The systems are bidisperse and prepared as outlined in chapter 2, section 2.4. To avoid this runaway we study systems with a fixed number of disks set to $N = 200$ and fixed width $L = 18$ and varying channel height between $H = 18$ and $H = 40$. For various heights, we explore properties of the flow. The rheology of the system depends on the height of the channel. For successively lower average density, we observe plastic flow, stable and bistable gas flow, and eventually thermal runaway. Our main concern in this chapter will be to identify of flow properties of fluidized states as solid-fluid transitions.

3.1 Convergence to the steady state

The evolution of the kinetic energy indicates whether the system has settled into a steady state. Appropriate plots of the kinetic energy versus time are depicted in Fig.3.1 for different channel heights $H = \{18, 20, \dots, 40\}$. As one increases the channel height, the kinetic energy of the system increases. As for all, the system becomes more dilute such that the number of collisions and rupture events and hence dissipation rate decreases. Consequently, the system also needs more time to settle down into a steady state. To account for that fact, we renormalized the time in that plot by the rupture frequency per particle:

$$t' = \frac{t \cdot f_R}{N} \quad (3.1)$$

here t is the natural time, f_R is the rupture frequency, and N the is number of particles. t' tells us after how many rupture events per particle the system reaches a stationary state. Almost all the curves reach a plateau after a few thousand rupture events per particle. Irrespective the height of the channel, the system reaches stationary state when each particle ruptures approximately 5000 capillary bridges. We show that in such a stationary state the injected and dissipated energy balance¹.

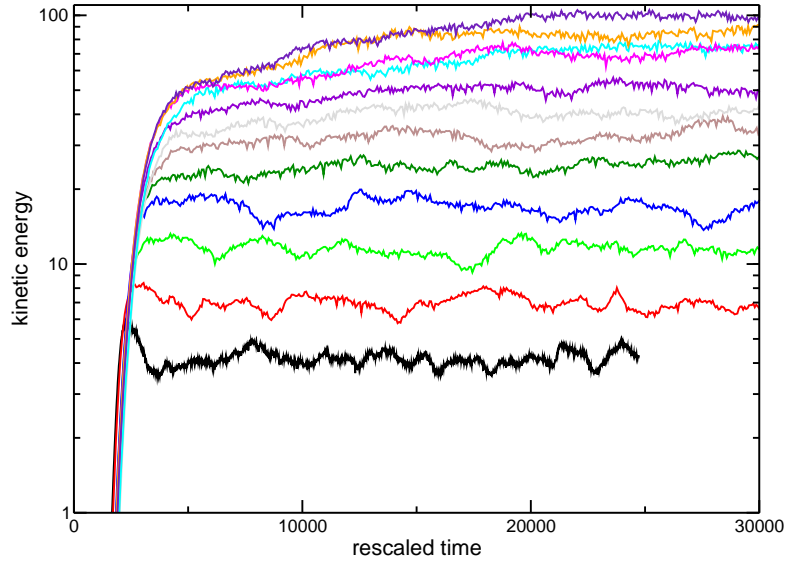


Figure 3.1: Kinetic energy per particle in the system versus rescaled time for different channel height. The black curve, lowermost energy, corresponds to $H = 18$, and for subsequent curves H increases by 2. The uppermost (maroon) curve, corresponds to $H = 40$. The number of particles is $N = 200$, the rupture separation is $S_c = 0.01$, the inclination angle is $\theta = 30^\circ$, and the gravitational acceleration is $g = 1$.

3.2 Profiles

In this section we present spatial profiles of various characteristics of the flow, like the granular temperature, and the local area fraction. The profiles are calculated as outlined in chapter 1, section .

¹More information is given in appendix sec.B

3.2.1 Downhill velocity

Bagnold's law [67] describes the velocity profile of dry frictional grains running down an inclined plane. The Bagnold's law predicts that the downhill velocity should be proportional to height to power 1.5, *i.e.* $V_x(y) \sim y^{1.5}$. However, the Bagnold's law does not hold for wet frictional grains [68]. In the current study, we address whether Bagnold's law can describe the downhill velocity profile of wet frictionless disks.

To measure the velocity profile in the system, we wait for at least $t' = 5000$, and afterwards compute the average drift velocity for different channel height. Fig.3.2 shows the drift velocity versus height for different channel height. Since the relation between shear stress and shear rate in our system is linear with an offset, the velocity profile should have a quadratic profile². The black solid curve shows the quadratic trend $V_x(y) = 0.2 + 0.155y - 0.00255y^2$. Such quadratic profile provides a much better fit to the simulation data rather than the Bagnold profile. Furthermore, it seems that there are two categories for the profiles. The maximum of profiles for $H > 30$ is smaller than the ones for $H < 30$. It seems that upon increasing the channel height, it initially decreased, but then it decreases.

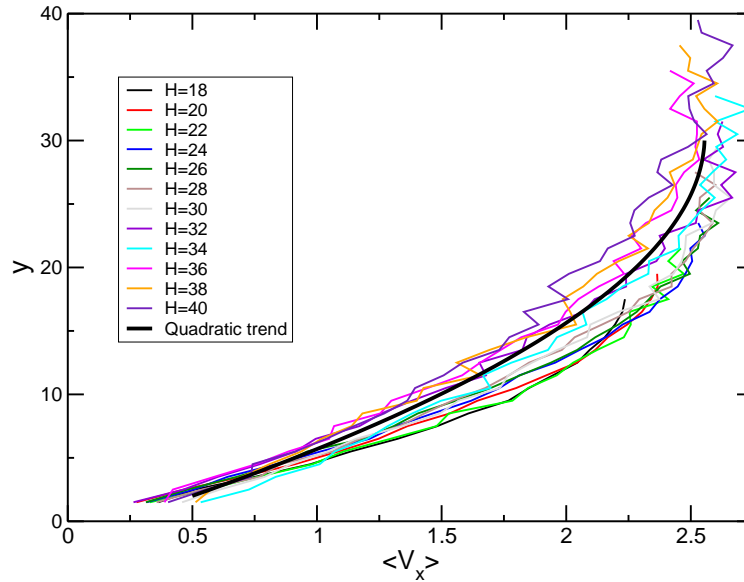


Figure 3.2: Average velocity versus height for different channel height. The black solid line shows the quadratic trend. The number of particles is $N = 200$, the rupture separation is $S_c = 0.01$, the inclination angle is $\theta = 30^\circ$, and the gravitational acceleration is $g = 1$.

²More information in sec.3.7.1

The change of the velocity profiles might be a hint that the rheological properties of the flow changes where crossing $H \approx 30$. To distinguish different rheologies, we look at the static and kinetic parts of the stress tensor³. Fig.3.3 shows the static and kinetic parts of the diagonal elements of the stress tensor. There indeed is a cross over at $H \approx 30$ above which the kinetic part of the stress tensor dominates the static part, and for smaller channel heights the static part becomes dominant. Consequently, for $H < 30$ there is a plastic flow regime and for $H \geq 30$ we are dealing with a granular gas. Furthermore, in Fig.3.3 S_{xx} and S_{yy} sit on top of each other showing that the stress field is isotropic.

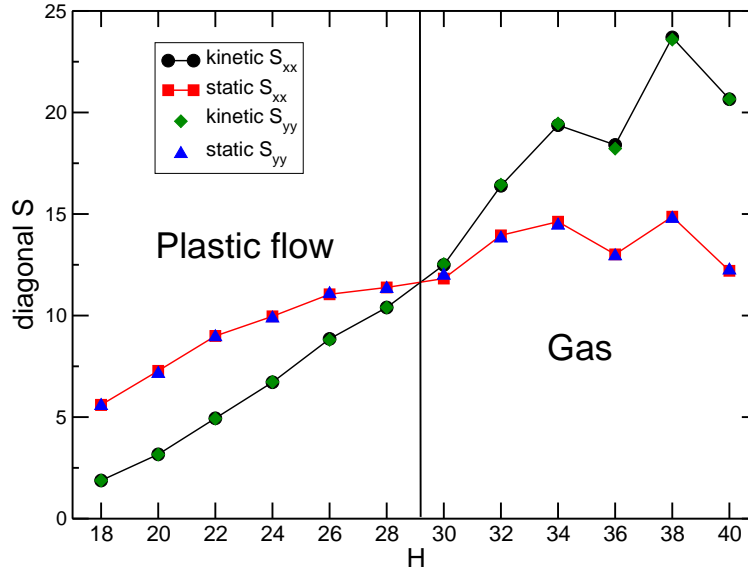


Figure 3.3: The static and kinetic parts of the diagonal elements of the stress tensor versus the channel height. There is a cross over around $H \approx 30$ above which the kinetic part dominates the dynamics of the system. The number of particles is $N = 200$, the rupture separation is $S_c = 0.01$, the inclination angle is $\theta = 30^\circ$, and the gravitational acceleration is $g = 1$.

Next We estimate the total average velocity per particle. The total average velocity \bar{V} is related to the average kinetic energy per particle \bar{K} by the relation:

$$\bar{V} = \left(\frac{2\bar{K}}{\bar{m}} \right)^{0.5} \quad (3.2)$$

where \bar{m} is the average mass. Fig.3.4 shows the average velocity of the system versus the channel height in spite of the fact that the maximum velocity decreases beyond $H \approx 30$. The

³The extensive information on the stress tensor is given in Appendix sec.C

average velocity increases linearly with the channel height for all investigated systems. The average velocity is well described by:

$$\bar{V} \cong 0.58 \cdot (H - 13) \quad (3.3)$$

Therefore, equ.3.3 implies that at $H \cong 13$ the drift velocity should tend to zero. The height of the pile after sedimentation is approximately $200/18 = 11.11$ which is very close to that number. For very shallow channels, there will be no place for the pile to dilate, and the system is frozen in a jammed state.

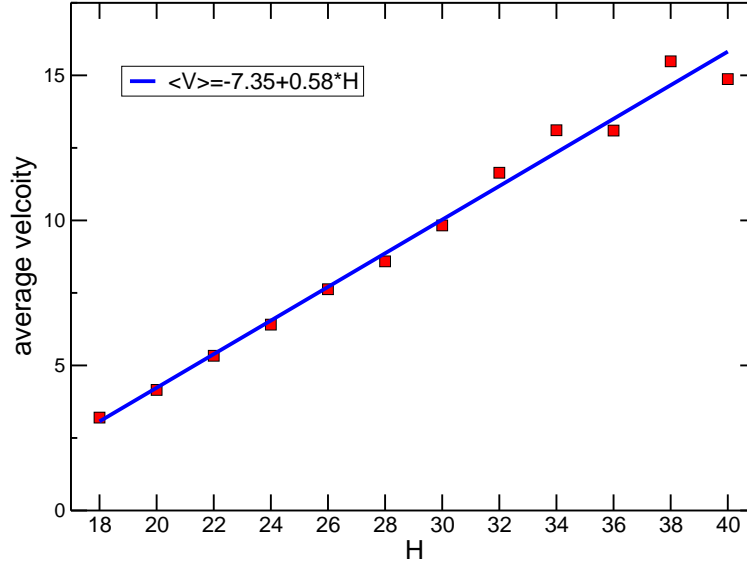


Figure 3.4: Average velocity per particle versus height of the channel. The number of particles is $N = 200$, the rupture separation is $S_c = 0.01$, the inclination angle is $\theta = 30^\circ$, and the gravitational acceleration is $g = 1$.

3.2.2 Local area fraction and granular temperature

The local area fraction is calculated by total area of the particles inside each bin divided by the area of the bin. Width of the bin is one average particle diameter and its length 18 times of average particle diameters. Fig.3.5 shows the local area fraction as a function of height for four different channel heights $H = \{18, 24, 30, 36\}$. The local area fraction of the first immobilized layer is about 0.83 and has been excluded from the data. For the system with the channel height equal to $H = 18$ close to the bottom layer and the top reflective wall, the local

density decreases, whereas it is constant at the bulk. Since the area of the system is 18×18 and there are 200 particles that fill almost half of the box. Accordingly, the average local area fraction is close to 0.5. For $H = 24$ the local area fraction decreases just at first and last bins, and the local area fraction in the bulk is constant. For $H = 30$ and $H = 36$ the local area fraction does not depend on the height. For $H = 36$ since the total area of the box is 18×36 , and the number of particles is 200 which occupy almost 1/4 of the box, hence the average local area fraction is close to 0.25.

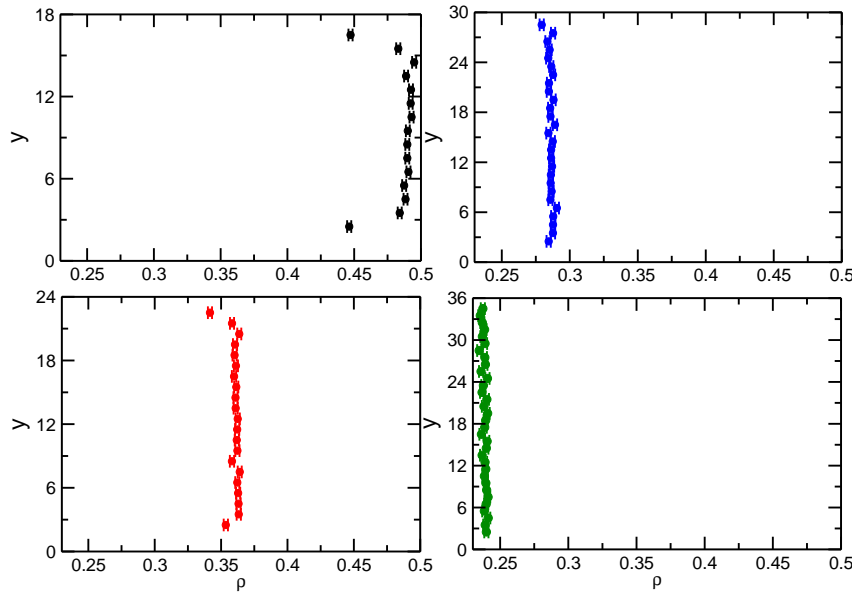


Figure 3.5: spatial profiles of the local area fraction for different channel heights $H = \{18, 24, 30, 36\}$. The number of particles is $N = 200$, the rupture separation is $S_c = 0.01$, the inclination angle is $\theta = 30^\circ$, and the gravitational acceleration is $g = 1$.

Fig.3.6 shows spatial profiles of the local granular temperature for different channel height $H = \{18, 24, 30, 36\}$. The granular temperature stays constant for all the channel heights and is independent of the height.

Comparing profiles of the granular temperature and the local area fraction, one concludes that upon increasing the channel height the system becomes homogeneous. Despite, for the system with channel height at $H = 18$, there are a little inhomogeneity close to the top and bottom walls.

Fig.3.7 shows the average granular temperature as a function of the channel height (the red circles). One can compare the granular temperature and the total average kinetic energy per

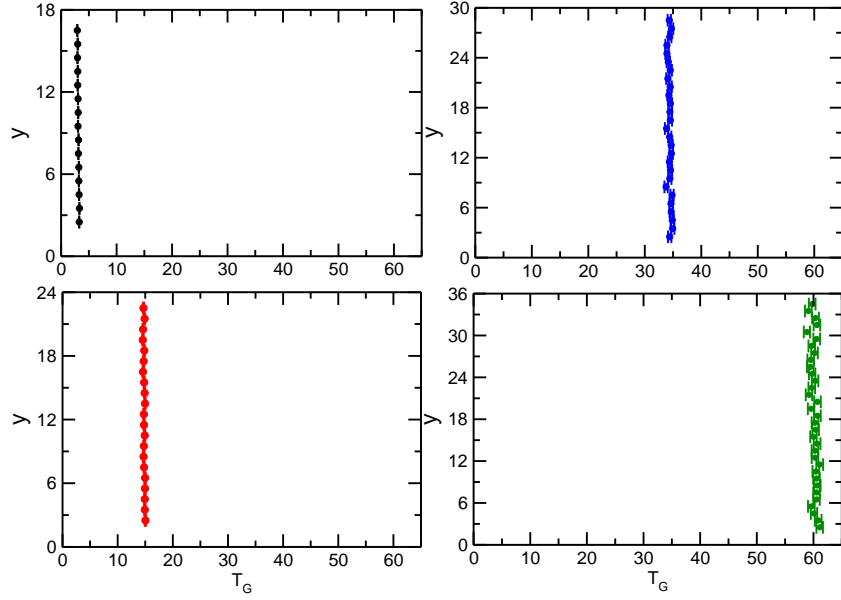


Figure 3.6: spatial profiles of the local granular temperature for different channel heights $H = \{18, 24, 30, 36\}$. The number of particles is $N = 200$, the rupture separation is $S_c = 0.01$, the inclination angle is $\theta = 30^\circ$, and the gravitational acceleration is $g = 1$.

particle from equ.(3.3) as follows:

$$\langle K \rangle = \frac{1}{2} \bar{m} \cdot \bar{V}^2 = \frac{1}{2} \bar{m} (-7.35 + 0.58 \times H)^2 \quad (3.4)$$

this curves is shown by the black curve. The total kinetic energy has two parts: the first part is the granular temperature, and the second part comes from the downhill drift velocity. Accordingly, the average kinetic energy should be larger than the granular temperature, but one sees that both curves are very close to each other. This means that contribution of the downhill drift velocity to the total kinetic energy of the particles is small. The motion in the system is dominated by the random thermal motion of the particles.

3.2.3 capillary bridges

The spatial distribution of capillary bridges is another parameter which is important to explore whether the system is homogeneous. In Fig.3.8 the spatial distribution of the capillary bridge is depicted for different channel heights. One sees that the capillary bridges are homogeneously distributed, except for a little inhomogeneity close to the bottom layer where one

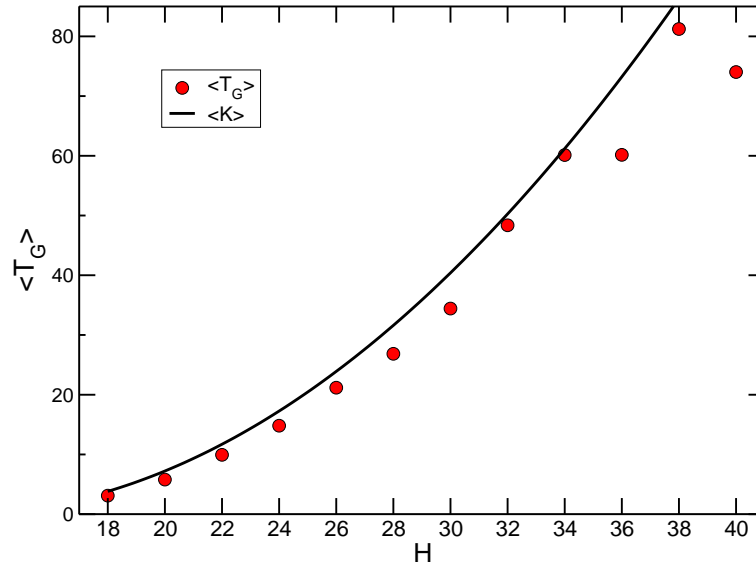


Figure 3.7: The red circles show the average granular temperature versus the channel height, and the black curve is the total kinetic energy of the system. The number of particles is $N = 200$, the rupture separation is $S_c = 0.01$, the inclination angle is $\theta = 30^\circ$, and the gravitational acceleration is $g = 1$.

layer of disks was immobilized.

The average number of capillary bridges decreases as the height of the channel is increased. Since the total number of particles is fixed to $N = 200$, upon increasing the channel height, the number of particles per unit of the area decreases. Accordingly, the number of liquid bridges decreases. One sees that the capillary bridges are homogeneously distributed in the system independently of the channel height.

3.2.4 Stress field

Fig.3.9 shows profiles of S_{xx} , S_{yy} , and S_{xy} , by black, green, and red colors as a function of the channel height. In all the figures, S_{xx} and S_{yy} sit on top of each other, showing that the pressure field is isotropic. As one increases the channel height, the internal pressure increases. On the other hand, the pressure does not depend on the channel height. As expected, the shear stress S_{xy} , which is depicted by red color, takes its maximum in the bottom layer, and it tends to zero as one goes to the upper layers.

To see how the pressure increases with channel height, average of the diagonal elements of

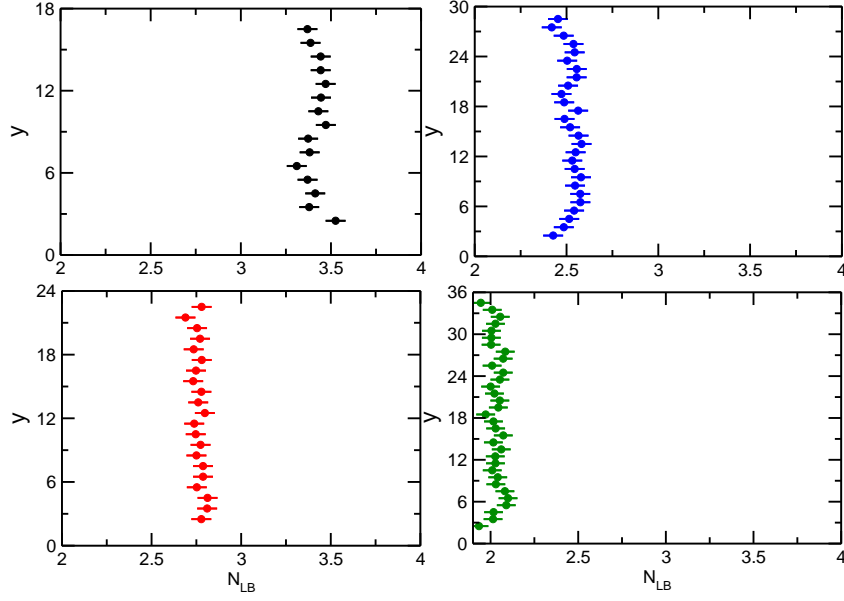


Figure 3.8: Spatial distribution of capillary bridges for different channel heights. The gravitational acceleration is $g = 0.1$, the inclination angle is $\theta = 30^\circ$, the rupture separation is $S_c = 0.01$, and the number of the disks is $N = 200$.

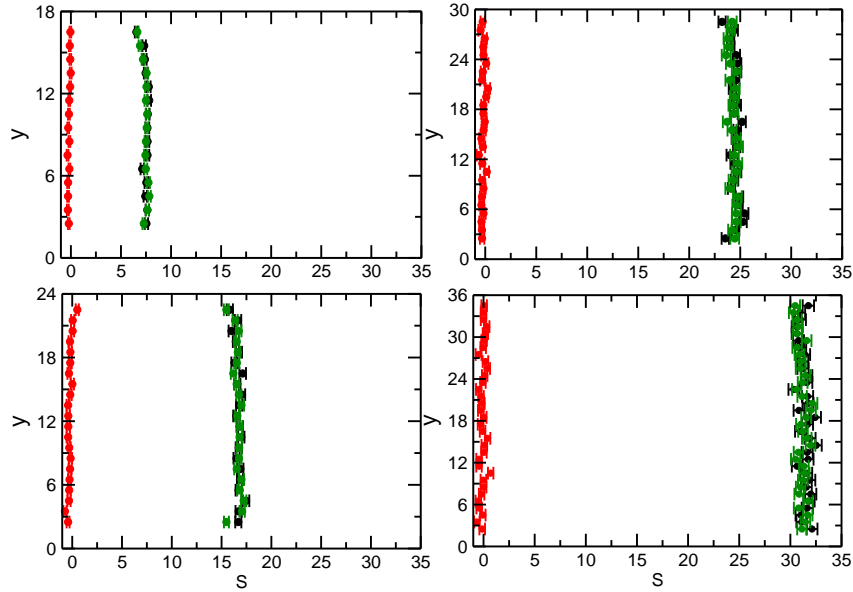


Figure 3.9: The components of the S_{xx} , S_{yy} , and S_{xy} of the stress tensor are shown in black, green, and red colors respectively. The number of disks is $N = 200$, the rupture separation is $S_c = 0.01$

the stress tensor is depicted versus the channel height in Fig.3.10. The pressure, is the average of the diagonal elements of the stress tensor, $P = (S_{xx} + S_{yy})/2$. It increases linearly with the channel height.

$$P \cong 1.36 \cdot (H - 12) \quad (3.5)$$

Accordingly, euq.(3.5) shows that the pressure vanishes at $H \approx 12$.

Just as for the mean velocity of particles, this is very close to the height of the channel after sedimentation which is approximately $200/18 = 11.11$. The physical reason is that when the upper boundary is very close to the pile, there will be no place for the pile to dilate, and therefore the system will no longer be a fluid and there will be a transition from the fluid to the solid state.

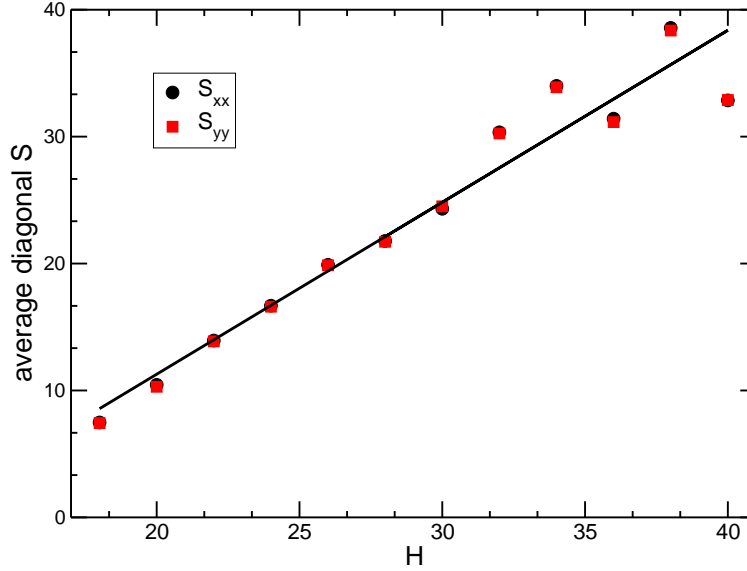


Figure 3.10: The diagonal elements of the stress tensor as a function of the height. S_{xx} and S_{yy} are depicted by black and red colors respectively. The number of disks is $N = 200$, the rupture separation is $S_c = 0.01$

3.3 Longer capillary bridges

So far, we explored the dynamics of the fluidized disks as a function of the channel height for a constant rupture separation $S_c = 0.01$, and we showed that the system settles down into a homogeneous gas state. Now, we are going to increase the rupture separation, and study the

dynamics of the system.

Fig.3.11 shows the local area fraction versus height for different rupture separations. By increasing the rupture separation, the system becomes more heterogeneous, and it seems that the particles tend to accumulate near the top of the channel, and the system becomes dilute close to the bottom layer. Furthermore, the longer the rupture separation, the more the heterogeneous the system becomes. For $S_c = 0.15$ (the violet line), which is the maximum possible rupture separation, the heterogeneity at the local area fractions is dramatically pronounced. By looking at the movies for the heterogeneous states, we observed that these states are not stable. The heterogeneous states switch randomly from one state to another one. In one of the states, a plug on top of the channel appears, and after some times it disappears. However, when there is no plug flow, the system is still heterogeneous, cold on top of the channel and hot in the bottom.

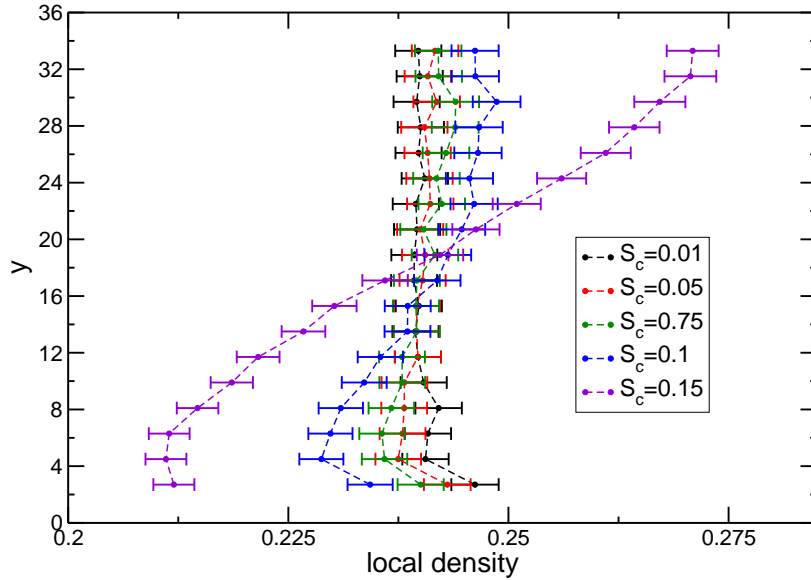


Figure 3.11: Local area fraction vs perpendicular position for five different rupture separations. The inclination angle is $\theta = 30^\circ$, the gravitational acceleration is $g = 0.1$, and the channel height is $H = 36$.

To quantitative amount of the heterogeneity, we define an order $\Delta\rho$ parameter as the difference of maximum $\rho_>$ and minimum $\rho_<$ of the local area fraction:

$$\Delta\rho = \rho_> - \rho_< \quad (3.6)$$

The different flow regions can then conveniently be represented as a function of $\Delta\rho$ and S_c . Fig.3.12 shows the order parameter ($\Delta\rho$), as a function of the rupture separation S_c . Since the transition from the gas state to the bistable state is crossover, one can not build a well defined border between a homogeneous gas state and the bistable state.

In the gas state, the order parameter scatters around very small values. However, in the bistable state, the order parameter increases linearly $\Delta\rho = 0.87(S_c - 0.085)$. The diagram tells us that the dynamics of the wet disks after fluidization does depend strongly on the the rupture separation of capillary bridges. For small rupture separations, we find a homogeneous gas state, and for larger rupture separations we observe a bistable regime while the system becomes heterogeneous.

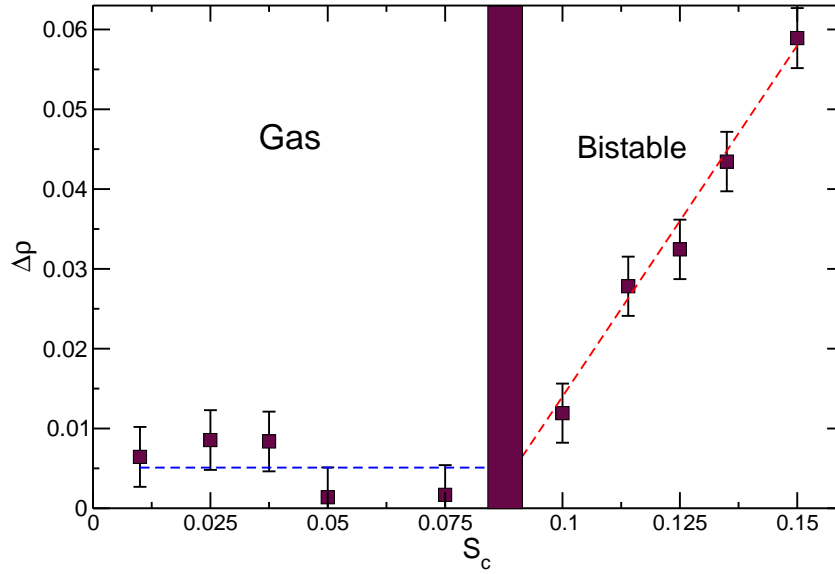


Figure 3.12: Difference $\Delta\rho$ of the local area fraction of the densest and most dilute layers vs rupture separation S_c . The inclination angle is $\theta = 30^\circ$, the gravitational acceleration is $g = 0.1$, and the channel height is $H = 36$.

3.4 Formation of capillary bridges

The formation of capillary bridges in the fluidized state significantly affects the dynamics of the system. First we study the temporal distribution of capillary bridges in the system. In Fig.3.13-inset shows the number of capillary bridge in a steady-state system versus time.

We want to know whether formation of the capillary bridges is a random process. We found that irrespective of channel height the probability distribution of $N_{LB}(t)$ is Poissonian. The Poissonian distribution of $N_{LB}(t)$ is a hint that the formation of the capillary bridges can be considered to be a random process. The autocorrelation function is another parameter that shows in more details the process of the formation of capillary bridges. The autocorrelation function $S(\tau)$ of $N_{LB}(t)$ can be defined as:

$$S(\tau) = \frac{1}{T} \int_0^T dt (N_{LB}(t + \tau) - \overline{N_{LB}})(N_{LB}(t) - \overline{N_{LB}}) / \overline{N_{LB}} \quad (3.7)$$

where τ is the time interval between successive formation of the capillary bridges, $N_{LB}(t)$ is the number of capillary bridges at time t , $N_{LB}(t + \tau)$ is the number of capillary bridges at time $t + \tau$, and $\overline{N_{LB}}$ is the average number of liquid bridges. Fig.3.13 shows the autocorrelation function versus rescaled time $\tau/2dt$ where dt is the time step of the integration ($dt = 10^{-4}$). The correlation drops to zero for $\Delta t > 4dt$. Measurements on the autocorrelation function show that formation of the capillary bridges is a random process. Furthermore, it shows that the life time of each capillary bridge is a very small time, and as soon as a capillary bridge forms, it ruptures after a very tiny time $\Delta t = 4 \times 10^{-4}$, which is just four times of the integration step.

Let us now try to understand the correlation time that came out from Fig.3.13. If we suppose that the system is dilute and hot, which both are the case, one can calculate mean free path from:

$$\frac{1}{l^2} = \frac{N}{LH} \quad (3.8)$$

in which l is the mean free path, $N = 200$ is number of the particles, $H = 36$ is the channel height, and $L = 18$ is the width of the system. We find:

$$l = 1.8 \quad (3.9)$$

On the other hand, one can calculate the average thermal velocity of each particle from:

$$\bar{v} = \left(\frac{2\overline{T}_G}{\bar{m}} \right)^{0.5} \quad (3.10)$$

where \bar{v} is the average thermal velocity, \overline{T}_G is the average granular temperature, and \bar{m} is the average mass of particles. From Fig.3.6 the average granular temperature is $\overline{T}_G \approx 60$. For

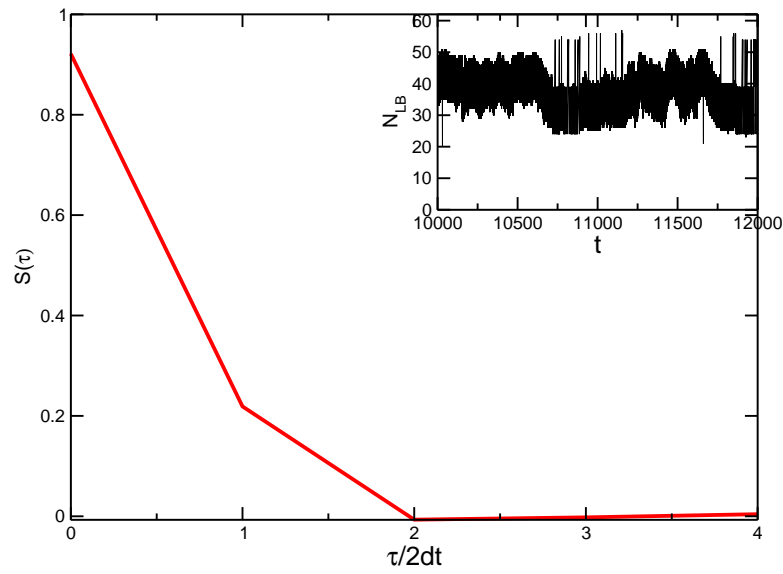


Figure 3.13: Autocorrelation function of formation of capillary bridges versus rescaled time. The integration time step is $dt = 10^{-4}$. Inset: temporal profile of the number of capillary bridges. The correlation length is equal to four times of the integration time step. $\theta = 30^\circ$, $g = 0.1$, $H = 36$, $S_c = 0.01$, The time interval is chosen between 10000 and 12000, during which the system has reached the stationary state.

a average mass $\bar{m} \approx 0.807$, we hence obtain:

$$\bar{v} = 13 \quad (3.11)$$

Therefore, the mean time between two collisions can be calculated as:

$$\bar{t} = \frac{l}{\bar{v}} = 0.15 \quad (3.12)$$

Subsequently, if one multiplies the correlation time to the number of the particles, in order to find the time to go to the next configuration, one obtains:

$$\Delta t \times N = 4 \times 10^{-4} \times 200 \approx 0.1 \quad (3.13)$$

which is a number very close to that of the mean time between two collisions. Therefore, one concludes that the formation of liquid bridges is a random process, and can be understood from a simple mean field approximation of the collisions in a dilute-hot gas.

3.5 Hysteretic solid-fluid transitions

3.5.1 Phase diagrams

In this section, we explore whether the solid-fluid transitions of wet disks on an inclined plane is hysteretic. Once the disks are sedimented, there is a percolation cluster of liquid bridges. As discussed in sec.3.2 this percolation cluster has a certain mechanical yield stress, above which the liquid bridge network breaks. Subsequently, the system fluidizes. We choose the average drift velocity of the particles as an order parameter to characterize the flow. According to chap.2, the control parameter is the gravitational acceleration in the direction of the inclined plane. Fig.3.14 shows the drift velocity versus $g \sin \theta$. The tilt angle θ increases stepwise for $\Delta t = 5000$ after each step. The gravitational acceleration is $g = 0.1$. The red squares show the beginning of the process from the horizontal level $\theta = 0^\circ$. Doing so, is a unique way to measure the yield point of the system.

As expected (in sec.3.2), the red squares end up at $\theta_F = 30^\circ$, where the material fluidized, and the order parameter, jumps from zero to a finite value. Therefore, fluidization transition is a discontinuous nonequilibrium process.

After fluidization of the system, we decrease the tilting angle stepwise, from $\theta = 30^\circ$ to

the horizontal level $\theta = 0^\circ$, in order to solidify the system (blue diamonds). As one decreases the tilting angle, the average drift velocity of the disks decreases linearly, and it jumps to zero at $\theta = 5^\circ$, where the system freezes to a disordered state. Apparently, the solidification transition is also a discontinuous transition. Hence, regarding the fact that $|\theta_F - \theta_S| \neq 0^\circ$, we conclude that the wet disks on an inclined plane undergo to a **hysteretic discontinuous phase transition**.

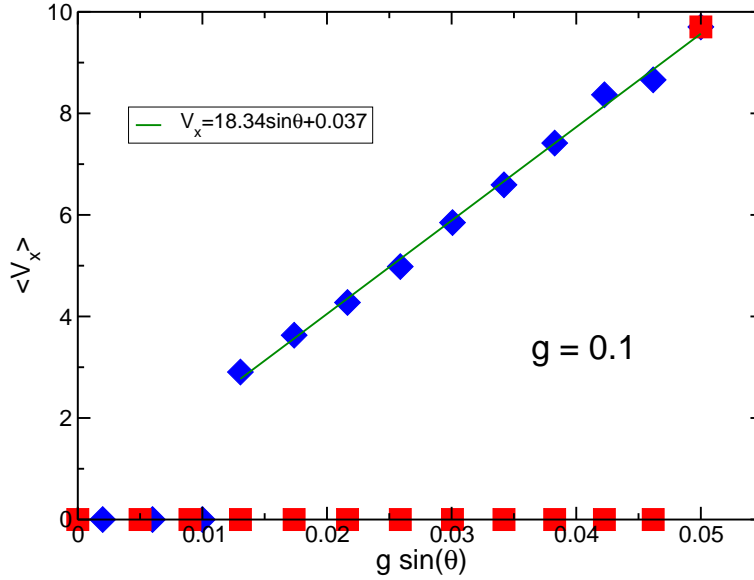


Figure 3.14: Average velocity as a function of the gravitational acceleration in the direction of the plane. The gravitational accelerations is $g = 0.1$, and the inclination angle is changed stepwise. The fluidization transition line (the blue diamonds) shows a linear behavior $V_x = 18(\sin \theta + 0.0002)$. The channel height is $H = 36$, the average mass is $\bar{m} = 0.807$, and $S_c = 0.01$.

In Fig.3.14 the drift velocity is proportional to the gravitational downhill acceleration $g \sin \theta$. This linear dependence is a hint that one can model such a system with a linear drag force with background. Keeping in mind such a linear dependence, we assume that there is a drag force in the system which depends linearly to the velocity:

$$ma_x = -\gamma V_x + F_x \quad (3.14)$$

Where m is the average mass of the disks, γ is the friction coefficient, V_x is the average velocity of the disks along the horizontal axis X, and $F_x = mg \sin \theta$ is the downhill gravitational force.

In the stationary state, one expects that $a_x = 0$, then $0 = -\gamma V_x + F_x$. Therefore, the fraction coefficient can be obtained as:

$$\gamma = \frac{mg \sin \theta}{V_x} \quad (3.15)$$

Since $m = 0.807$, $g = 0.1$, and $V_x/(g \sin \theta) \approx 18$ is the slope of the line in Fig.3.14, and equals to 18.398, the coefficient of the friction is:

$$\gamma = 0.0044 \quad (3.16)$$

Hence, the drag force in the stationary state can be written as:

$$F_{drag} = -0.0044 \cdot V_x \quad (3.17)$$

We will show later in the current section in Fig.3.16, where we explore the hysteretic transition by changing the gravitational acceleration at a fixed inclination angle, that equ.3.17 fits our data.

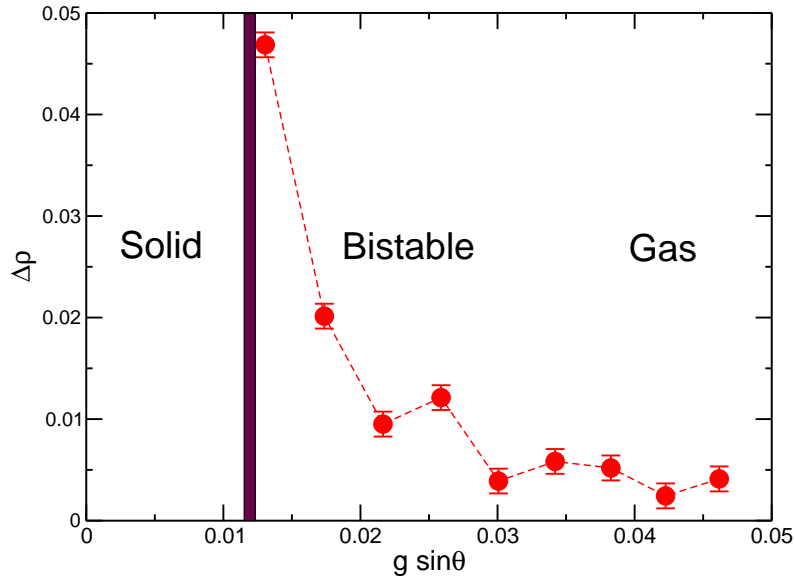


Figure 3.15: The largest variation of the density $\Delta \rho$ as a function of $g \sin \theta$. The channel height is $H = 36$, the average mass is $\bar{m} = 0.807$, and $S_c = 0.01$.

To interpret this data we check whether the system is homogeneous. We look again at the difference of the local area fraction between densest and most dilute regions in the system as a function of the inclination angle for the fluidized state (Fig.3.15). For large $g \sin(\theta)$ the

system is homogeneous, but for small $g \sin(\theta)$ the inhomogeneity gradually becomes larger, and finally it solidifies at $g \sin(\theta) \approx 0.013$. As described in sec.3.3, these heterogeneous states are bistable. However, one can not distinguish the border between homogeneous and bistable states. One can summarize these regions as the following:

Gas \implies Bistable \implies Solid

- **Gas regime:** For large $g \sin \theta$, after the fluidization, system is homogeneous without any gradient in the local area fraction.
- **Bistable regime:** For small $g \sin \theta$ close to the solidification point, the system becomes heterogeneous.
- **Solid regime:** For $\theta < 5^\circ$, the material is solidified.

The fluidized wet disks do not turn directly from a fluidized state into a solidified one. Whereas there is an intermediate step between the solidified and fluidized states in which the system becomes heterogeneous and bistable.

If one looks at the gap between the fluidization and the solidification angles $|\theta_F - \theta_S| = 25^\circ$, one finds an astonishing big gap. Why does the system have such a big memory (or hysteresis)? To answer to that question, we refer to the dissipation mechanism of the system. Dissipation occurs when a capillary bridge ruptures, and capillary bridges rupture in the gas-like state when the relative kinetic energy of two adjacent colliding disks is larger than the energy barrier caused by the capillary bridge interaction. However, in the gas-like state close to θ_F the average granular temperature of the system is already about 600 times larger than the capillary bridge energy. One has to go to much smaller downhill accelerations $g \sin \theta$ to reach systems with temperatures where the bridge energy is strong enough to allow for the formation of stable capillary bridges.

As it is described in the phase diagram of bidisperse disks on inclined plane (Fig.2.15), we chose two parameters as the principal parameters to describe the phase diagram of the tilted wet disks. Namely the gravitational acceleration g , and the tilting angle θ . In the current section, we study the existence of the hysteresis for a case in which, the gravitational acceleration is set to $g = 0.1$, and the tilting angle is the control parameter. Now we set the tilting angle to $\theta = 30^\circ$, and explore the hysteresis by stepwise incrementing and decrementing the gravitational acceleration. Fig.3.14 shows the hysteretic loop for that case. After the sedimentation of the wet disks, the gravitational acceleration is increased stepwise from $g = 0$, until the pile is

fluidized. Subsequently, namely the red squares, at $g_F = 0.1$, the gravitational acceleration is decremented stepwise in the same way (blue diamonds). The drift velocity decreases linearly with $g \sin \theta$, and now we can check whether the theoretical prediction of equ.(3.17) fits to our simulation data. According to equ.(3.17) the relation between the gravitational downhill force and the drag force should be:

$$F_{drag} = -0.0044 \cdot V_x = -mg \sin(\theta) \quad (3.18)$$

Since we have $\theta = 30^\circ$, the relation between the average velocity and $g \sin \theta$ should be:

$$V_x \approx 180g \sin(\theta) \quad (3.19)$$

Therefore, the theory predicts that slope of the blue diamonds in Fig.3.14 should be 180. The green line in Fig.3.14 shows such a slope, and one can see that the slope perfectly fits to the data.

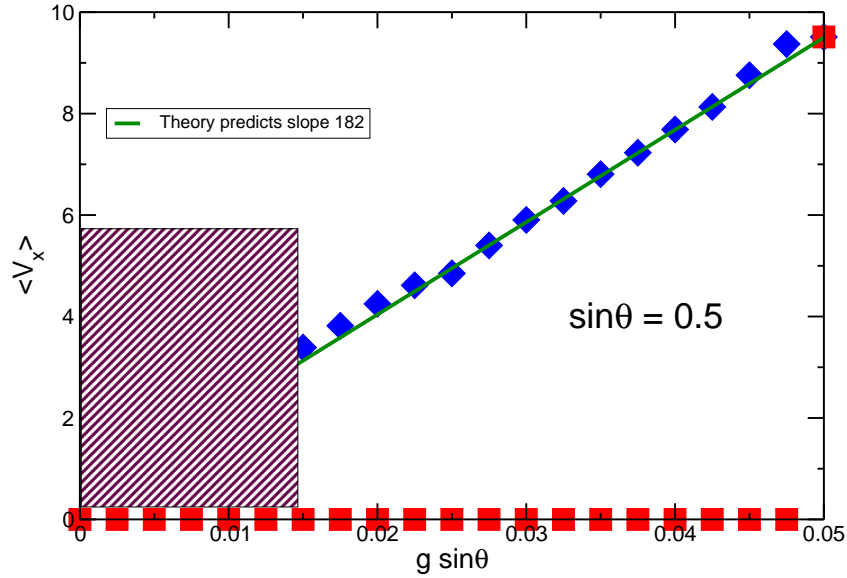


Figure 3.16: Average velocity vs the gravitational downhill acceleration $g \sin \theta$. The rectangle box shows the region in which $g \sin \theta$ is small and the system needs a very long time to settle down into a stationary state. The inclination angle is fixed to $\theta = 30^\circ$, the channel height is $H = 36$, the length of the system is $L = 18$, the rupture separation is $S_c = 0.01$, and the average mass is $m = 0.807$.

We look again on the order parameter $\Delta\rho$ to see whether the system remains homogeneous.

Fig.3.17 shows $\Delta\rho$ versus $g \sin \theta$. Fig.3.15, for $g \sin \theta > 0.3$, the order parameter $\Delta\rho$ is very small. The system is homogeneous. However, for $0.01 < g \sin \theta < 0.03$ the order parameter increases dramatically, and the system becomes again dense in the top of the channel, and dilute close to the bottom layer.

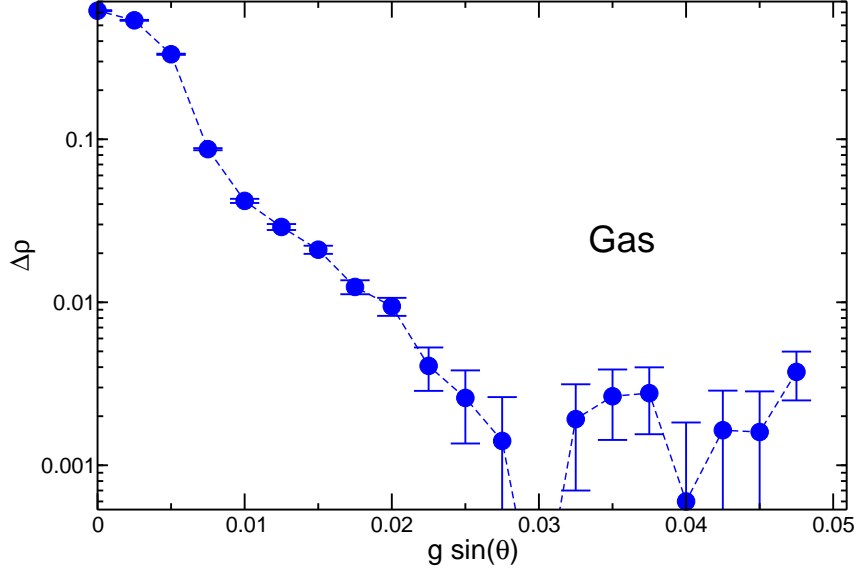


Figure 3.17: Difference of the maximum and minimum of the local area fraction in the system ($\Delta\rho$) as a function of $g \sin \theta$ in the hysteretic loop. The inclination angle is fixed to $\theta = 30^\circ$, the channel height is $H = 36$, the length of the system is $L = 18$, the rupture separation is $S_c = 0.01$, and the average mass is $m = 0.807$.

3.6 Leidenfrost state

In order to look at details of the bistable states, we discuss now the density profiles in the gas-like state. Fig.3.18 shows the local area fraction as a function of the height. One can see for large gravitational accelerations the system is homogeneous, but as one approaches towards the solidification point by decreasing the gravitational acceleration, the particles tend to accumulate near the upper wall. This accumulation of particles in a high density phase floating on top of a low-density phase is reminiscent to a Leidenfrost state [69].

We argued in the last section that such a heterogeneous state is bistable. To prove this idea, in Fig.3.19 we show snapshots at the end of the hysteresis transition where the gravitational

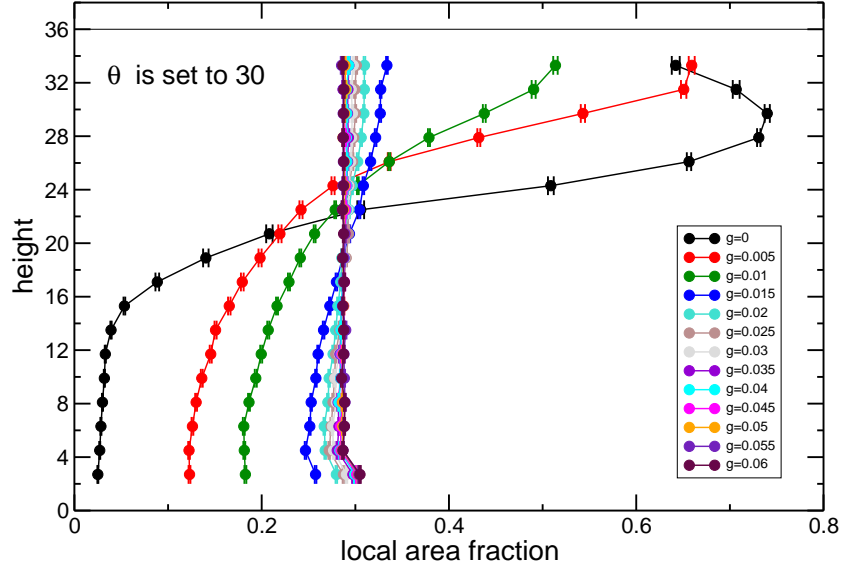


Figure 3.18: Profiles of the local area fraction for different gravitational accelerations. The tilting angle is set to $\theta = 30^\circ$. As one decreases the gravitational acceleration the system becomes more heterogeneous.

acceleration is $g = 0.005$, and the inclination angle is $\theta = 30^\circ$. There are three different colors for the disks:

1. **Blue**: If a particle has a capillary bridge.
2. **Red**: If a particle has no capillary bridge.
3. **Maroon**: Immobilized disks in the bottom layer.

Fig.3.19-top is snapshot of the system at $t = 96071$. There are a lot of particles accumulated in the top layers. The granular temperature close to the bottom layer is much higher than the granular temperature near the top wall. The bottom-right panel is snapshot of the system at $t = 96316$. Although the plug on top of the system has become thinner, there are still a lot of particles accumulated on top of the system, and there is still a gradient in the granular temperature. The bottom-left panel is taken at $t = 96716$. The plug on top of the system is gone, but the system is still heterogeneous. This process in Fig.3.19 repeats irregularly in time, and it is not an oscillation with a certain period.

To get more insight into the temporal evolution states, we look at the kinetic energy of the system as a function of the time. Fig.3.20 shows the kinetic energy of the system in the bistable

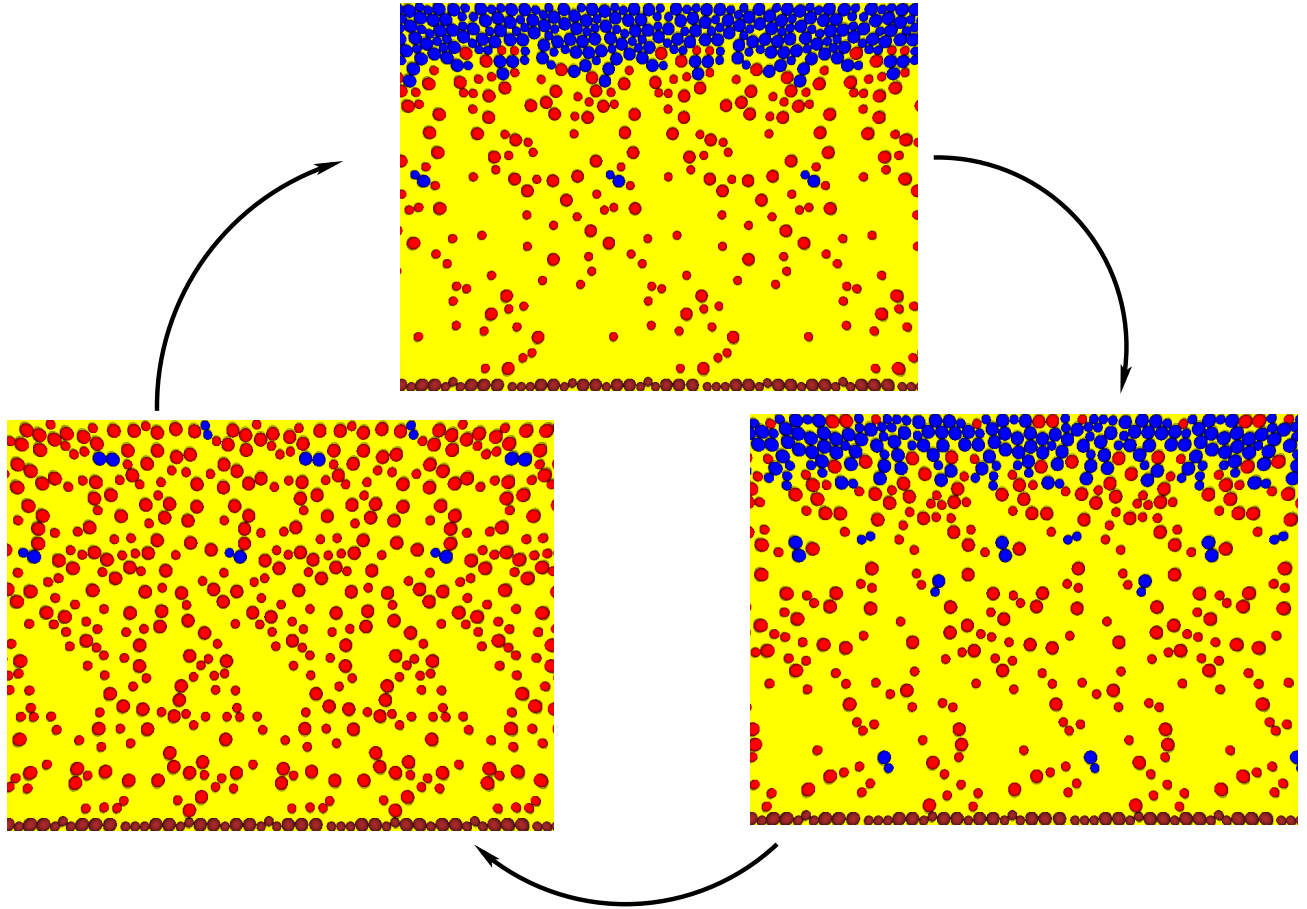


Figure 3.19: Snapshots of the system at $t = 96071$ (top), $t = 96316$ (bottom-right), and $t = 96716$ (bottom-left). The gravitational acceleration is $g = 0.005$, the inclination angle is $\theta = 30^\circ$, and the rupture separation is $S_c = 0.01$.

state. The time where the snapshots are taken in Fig.3.19 are marked. The figure demonstrates that the switching shown in the Fig.3.19 is not an oscillation. The system switches randomly from one state, in which a plug flows on top of the system, to another state, where the plug is gone.

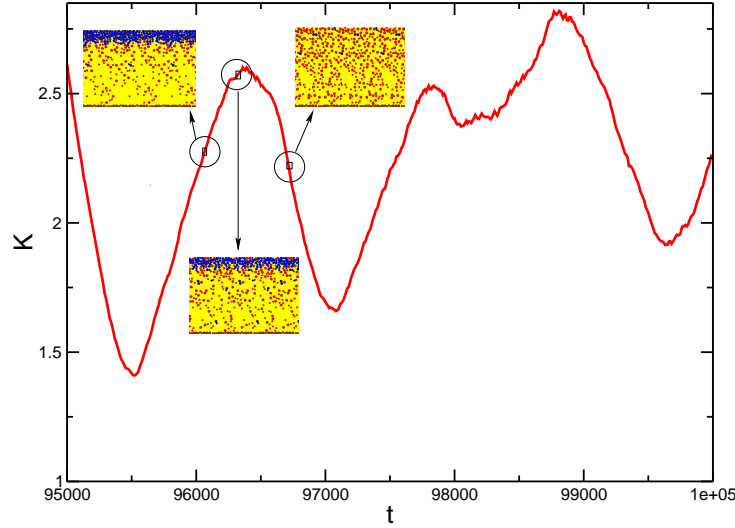


Figure 3.20: Kinetic energy per particle K versus time. Snapshots show how the system looks like at different times. The gravitational acceleration is $g = 0.005$, the inclination angle is $\theta = 30^\circ$, and the rupture separation is $S_c = 0.01$.

Let us explain Fig.3.20 in more details. At the first snapshot where $t = 96071$, a plug on top of the system slides over a hot gas, and one can see that the kinetic energy increases. At the same time the drift velocity of the plug increases too.

At $t \approx 96316$, where the second snapshot is taken, the kinetic energy reaches its local maximum. By that time, the plug on the upper side of the system has become thinner. After the second snapshot, the kinetic energy decreases resulting to an increase in the random motion of the disks. At $t = 96716$ the plug is gone, and the random motions of the particles is increased. It means that the granular temperature is increased. Therefore, one can explain the bistable state as the following:

1. A plug slides over a gas, and the velocity of the plug increases.
2. Due to the collisions between the plug and the gas, the temperature of the gas increases.
3. The hot gas melts the plug such that it disappears.

4. Since the gravity is relatively low, the particles tend to escape from the bottom layer where the granular temperature is very high, and eventually a plug forms again in the upper side of the system.

3.6.1 Summary

We saw that for small gravitational accelerations the system becomes bistable. At the end of the loop where $g = 0$ the system enters to a free cooling scenario in which the plug on top of the system moves for an arbitrary long time on a hot gas. Since the force-based MD simulations are not appropriate to study the free cooling, we can not explore that state. Finally, we summarize the hysteretic transition as the following:

Gas \implies Bistable \implies Free cooling

- **Gas regime:** For large gravitational accelerations, the fluidized disks are homogeneously distributed in the system. There are no granular temperature gradient, or the local area fraction gradient.
- **Bistable regime:** For small gravitational accelerations, the system becomes bistable. We observed a Leidenfrost state and the system becomes visibly heterogeneous.
- **Free cooling:** For $g = 0$, one deals with a free cooling scenario. The hot gas layer interacts with the immobilized disks in the bottom, as well as the sliding plug. One expects that as the hot gas cools down the bloc in the upper side of the system becomes larger and absorbs the gas.

In conclusion, if one fixes the gravitational acceleration and changes the inclination angle, for small gravitational downhill accelerations the material solidifies. Whereas, if one fixes the inclination angle, and changes the gravitational acceleration, for small gravitational downhill accelerations the material does not solidifies and a free cooling scenario begins.

3.7 Appendix

3.7.1 Quadratic velocity profile

As we mentioned earlier in this chapter, the best fit to the velocity profile of wet disk running down on an inclined plane is a quadratic profile. In this section, we attempt to derive

such a profile. The shear stress $S_{xy}(y)$ in the system can be given as:

$$S_{xy}(y) = mg \sin \theta (H - y) \quad (3.20)$$

where $mg\theta$ is the gravitational downhill force, H is the channel height, and y is the vertical component to the plane. Subsequently, since the system possesses a yield stress, then the relation between the shear stress and the shear rate $\partial_y V_x(y)$ can be written as:

$$S_{xy}(y) = S_{xy}^* + \eta \partial_y V_x(y) \quad (3.21)$$

here S_{xy}^* is the yield stress of the system, and η is the viscosity. Using equ.(3.20) and equ.(3.21) the velocity profile can be derived as:

$$V_x(y) = c_1 y^2 + c_2 y + c_3 \quad (3.22)$$

where $c_1 = -\frac{mg \sin \theta}{2\eta}$, $c_2 = \frac{1}{\eta}(mgH \sin \theta - S_{xy}^*)$, and c_3 is a constant depending on the boundary conditions. equ.(3.22) shows that the velocity profile of the system can be expressed as a quadratic function.

Chapter 4

Isochoric model for avalanches

In the last chapter, we presented the results of a simple avalanche model for a 2D wet granular pile on a rough inclined plane. As the inclination angle is changed the system undergoes a discontinuous-hysteretic dynamic phase transition between a fluidized and a solid state. We want to know whether the discontinuity and the hysteresis are universal features of solidification and fluidization transitions in wet disks.

Using the same bidisperse disks that were being used in chapter 3 we will investigate an isochoric model for avalanches in wet disks, *i.e.* in systems where the total area fraction is conserved. We drive the system with a spatially heterogeneous external force and follow the same procedure which we used in chapter 3 to study the dynamics of a wet pile of disks on an inclined plane. At first, we will explain the preparation of a dense assembly of wet disks in the isochoric system. Subsequently, we will study spatial and temporal profiles of the drift velocity, the granular temperature, the area fraction and other relevant physical quantities.

There are several open questions to be answered for the isochoric system. First of all, is the fluidization transition under isochoric conditions still discontinuous? Is there an up-down transition, *i. e.* fluidized-to-solid transition [70, 71]. Does the system reach a stationary state in which the injected power and the dissipated power balance or does the system exhibit a temperature runaway in a certain range of control parameters?

4.1 Description of the model

The simulation under isochoric conditions were performed using the 2D model employed in the simulation of a wet granular pile on an inclined plane, see chapter 2. In order to prevent

crystallization and segregation we use a bidisperse mixture of disks with a ratio between the large radius R_s and the small radius R_l of 1.4. Overlapping disks interact via a soft core repulsive interaction and a short ranged hysteretic capillary force. The value of the prefactor ϵ controlling the hardness of the disks is set to 10^3 , while the rupture length S_c of the capillary bridges is varied. In the sequel we make use of dimensionless rescaled units for time, length and mass as outlined in chapter 1, section 1.2.4. The simulation box is a square of size $L \times L$. Periodic boundary conditions are applied in both horizontal and vertical directions. A predictor corrector method is used to integrate Newton's equation of motion. The time step of integration is set to $dt = 10^{-4}$.

In order to agitate the disks we apply an external force similar to the gravitational force driving the disks down the inclined plane as described in chapter 3. Here, we employ an external force as it has been used by Schultz *et al.* in Ref. [11] to study the fluidization transition in a three dimensional assembly of wet spheres. It is given by

$$\mathbf{F}_i^{ex} = \mathbf{e}_y F_0 \cos\left(\frac{2\pi x_i}{L}\right), \quad (4.1)$$

where \mathbf{F}_i^{ex} is the external force acting on particle i , \mathbf{e}_y the unit vector pointing into y-direction, F_0 the amplitude of the external force, x_i the x-coordinate of particle i , and L the dimension of the simulation box. The number of disks in the system is generally set to $N = 506$ if not stated otherwise.

Because of the spatial heterogeneity of the external force one may expect that the distribution of physical observables in the system will be as well heterogeneous. Hence, physical quantities such as granular temperature, area fraction, components of the stress tensor, and density should be calculated locally. A definition of these quantities can be found in chapter 1.

In the regime of strong driving the fluidized assembly of disks may undergo the Kolmogorov flow instability leading the system being heterogeneous into y-direction, see *e. g.* Refs. [72, 73]. At moderate strength of the external force, however, we expect the system to remain homogeneous into the y-direction and we divide the system into several bins along the direction of the flow, *i. e.* into the vertical direction. The width of each bin equals the average disk diameter $\langle D \rangle$. We will calculate local physical quantities in each bin as time averages.

4.1.1 Preparation

In the previous chapters 2 and 3 we investigated the stability and dynamics of assemblies of disks that have sedimented on a plane under the action of gravity. In the isochoric system considered here we have to apply a different preparation method in order to produce spatially homogeneous disk packings. This can be achieved in two main steps:

1. **Random sequential addition:** disks are randomly added to the box and are accepted as new disks if the added disk does not overlap with any of the disks that have already been successfully deposited. In order to obtain a bidisperse packing with the same number of small and large disks the type of disk is alternated once a disk has been successfully placed. The largest area fraction that can be reached by this method is approximately $\phi \simeq 0.62$. To reach larger area fractions a further mechanism should be engaged.
2. **Lubachevsky-Stillinger algorithm:** since we want to span a wide range of area fractions up to $\phi = 0.84$, being the limit of random close packing we use the Lubachevsky-Stillinger algorithm to reach area fractions above $\phi \simeq 0.62$. The algorithm can be simply expressed as blowing up the disks at thermostated temperature [74].

Figure 4.1(top) displays a snapshot of the system after random sequential addition with a total area fraction of $\phi = 0.62$. At this point the simulation time is set to $t = 0$. Because random sequential addition generates disk packings which are free of overlaps there are no liquid bridges present. By applying the Lubachevsky-Stillinger algorithm the area fraction of the system is increased until the desired value is reached. Figure 4.1(bottom) shows a packing with an area fraction of $\phi = 0.72$ which has been generated by the Lubachevsky-Stillinger algorithm. Blue spots illustrate capillary bridges between touching disks.

During the blow up of disks a certain amount of energy is injected into the system and since we want to obtain an initial packing of resting disks, the injected energy should be dissipated before the external driving force according to equ. (4.1) is switched on. We use a viscous friction as outlined in chapter 1, section 3.2, to dissipate the injected energy.

The blow up of disks takes from $t = 0$ to approximately $t_1 = 20$. The dissipative force according to equ. (1.5) is switched on until $t_2 = 100$ in order to ensure that most of the injected energy has been dissipated.

The actual simulation starts at time t_2 where the external driving force is switched on. Time averaging of local quantities such as the granular temperature, components of the stress tensor, drift velocity, rupture frequency of capillary bridges, and area fraction of small and large disks

Time	Description
$0 < t < t_1$	$F_0 = 0, b \neq 0, f_{LB} = 0, \langle D \rangle < 1$
$t_1 < t < t_2$	$F_0 = 0, b \neq 0, f_{LB} = 0, \langle D \rangle = 1$
$t_2 < t$	$F_0 \neq 0, b = 0, f_{LB} = 1, \langle D \rangle = 1$
$t_3 < t$	Averaging starts

Table 4.1: Protocol of the numerical simulations.

starts at time $t_3 = 500$. Definitions and details of the way these quantities are calculated are given in chapter 1, section 1.2.5. A short summary of the simulation times is found in table 4.1.1.

4.2 Results

4.2.1 Time evolution

Figure 4.2 shows the local drift velocity in the first and central bin as a function of time. The box is divided into 18 bins along the vertical direction

The drift velocity is zero until $t = t_2 = 100$ during which the initial packing is prepared. The external driving force is applied at $t = t_2$ when the disks in the first bin start to move upwards (black curve) while the disks in the central bin begin to move downwards (red curve). However, at about $t \approx 114$ the magnitude of the drift velocity start to decrease. At times larger than $t \approx 135$ the drift velocity in both the first and the central bin fluctuate around a value close to zero. The same fluctuations can be observed for the drift velocity in the remaining bins.

A closer inspection of the data reveals that all drift velocities fluctuate around the same value which increases linearly in time. From this observation one may conclude that the whole system behaves like a rigid body which is accelerated due to a non-zero total force acting on the disks. Owing to the disorder in the assembly there will always be an imbalance between the magnitude of forces pulling the disks up and pushing them down. Hence, the direction of the drift is randomly distributed among different realizations of the system. The global drift clearly indicates the existence of a rigid cluster which comprises the majority of disks.

After switching on the external driving force, the system needs a certain finite time to reach a solid state. This relaxation time decreases as one increases the total area fraction of the disks. During relaxation, the disks rearrange and finally form a percolating network of

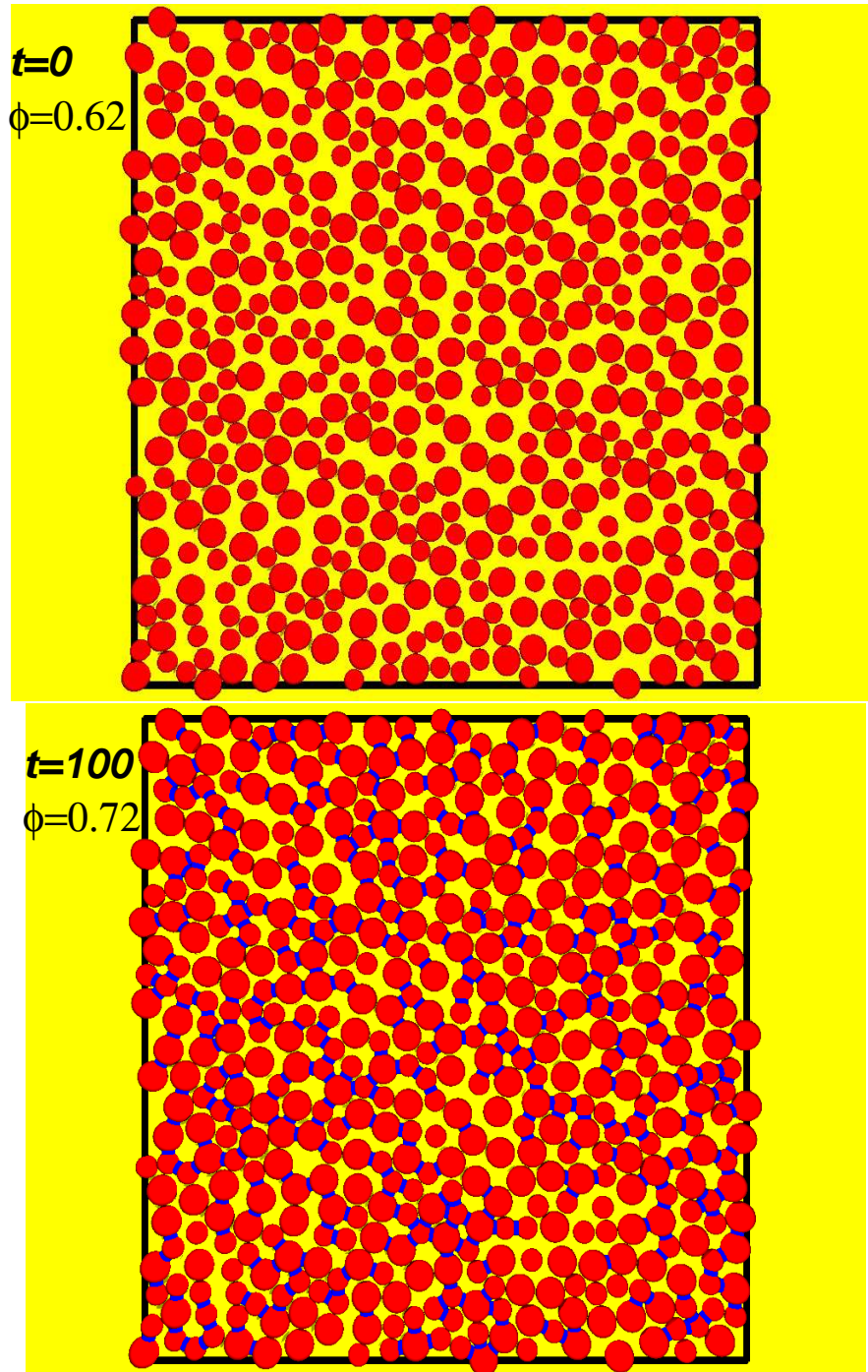


Figure 4.1: (Top) At $t = 0$ a pre-initial packing with an area fraction of $\phi = 0.62$ is generated using random sequential addition. The disks do not overlap. (Bottom) The area fraction of the system is increased to $\phi = 0.72$ employing the Lubachevsky-Stillingr algorithm [74]. The number of particles is $N = 506$, the system size $L = 18$, and the rupture separation $S_c = 0.01$.

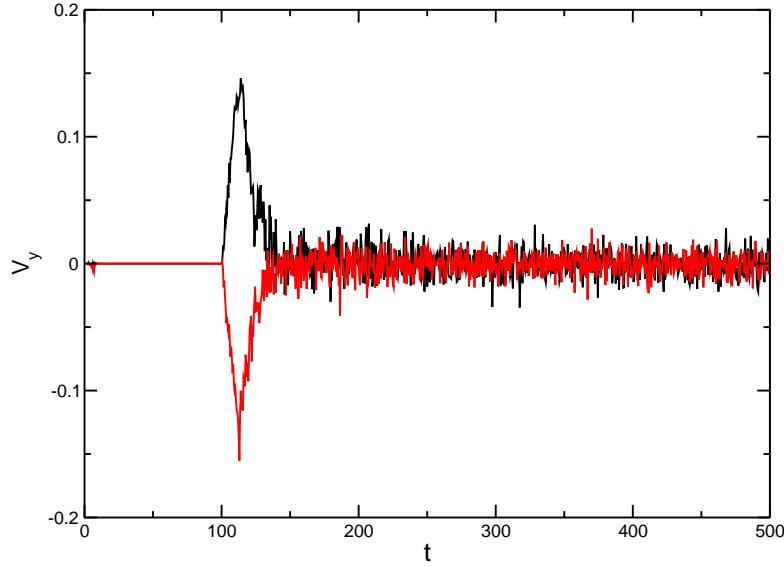


Figure 4.2: Drift velocity in the first and central bin as a function of time as depicted by the black and red curves, respectively. The number of particles is $N = 506$, the system size $L = 18$, the rupture separation $S_c = 0.01$, the amplitude of the external force $F_0 = 5 \cdot 10^{-3}$, and the area fraction $\phi = 0.72$.

capillary bridges which is strong enough to sustain the stress created by the external force. As one can see in Fig. 4.2 the drift velocities in the final solid state exhibit large fluctuations. This observation can be explained by the work received from the external field in the transient fluidized state. During the formation of the solid network this work is dissipated into thermal energy and as long as the granular temperature is smaller than the energy ΔE required to break a capillary bridge this thermal energy will remain in the system.

At small amplitudes $F_0 = 5 \cdot 10^{-3}$ of the external driving force the system is found in a transient fluidized state before it eventually reaches a solid state, cf. Fig4.2. For an amplitude $F_0 = 1 \cdot 10^{-2}$, however, the system does not relax into a solid state. The time evolution of the drift velocity in Fig. 4.4 illustrates that the system instead remains in a fluidized state in which the magnitude of the drift velocity in the first bin (black curve) almost equals the magnitude of the drift velocity in the central bin (red curve). Therefore, by increasing the amplitude of the external driving force, the system can be held in a fluidized state.

The long time evolution of the drift velocity demonstrates (up to $t \approx 10^3$ and longer) that the fluidized state can be viewed as a stationary state. Fluctuations of the drift velocities may become strong for dense systems close to the RCP limit and it becomes necessary to average over relatively long periods of time. Furthermore, we checked for the balance of injected

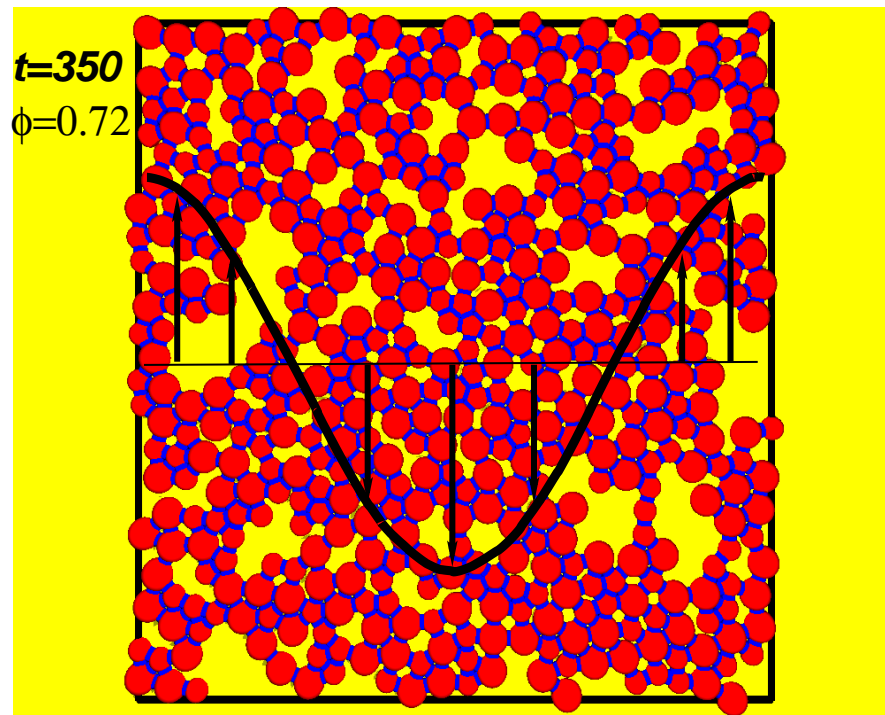


Figure 4.3: Snapshot of the system at $t = 350$ in which the system reached a solid state and moves like a rigid body downwards. The spatial variation of the external driving force depicted by the black curve. The number of particles is $N = 506$, the system size $L = 18$, the rupture separation $S_c = 0.01$, and the area fraction $\phi = 0.72$.

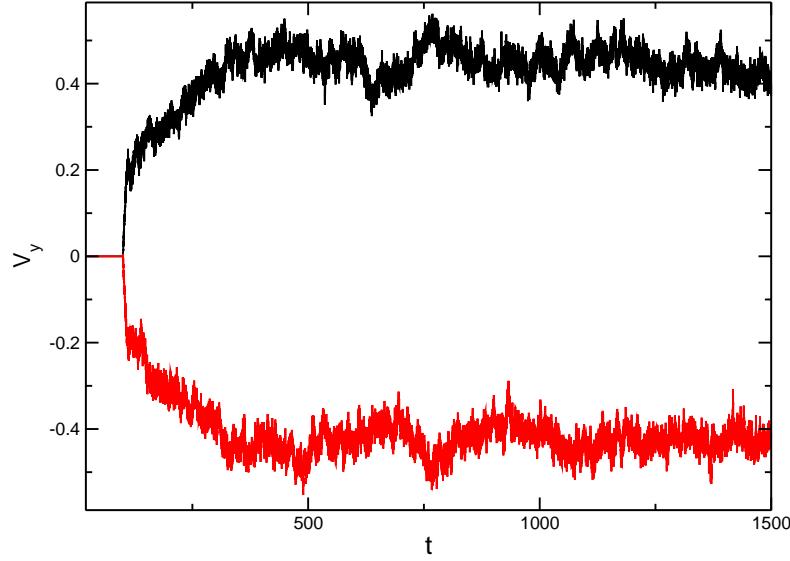


Figure 4.4: Local drift velocity as a function of time in the first and central bin as depicted by the black and red curves respectively. The number of particles is $N = 506$, the system size $L = 18$, the rupture separation $S_c = 0.01$, the amplitude of the external force $F_0 = 1 \cdot 10^{-2}$, and the area fraction $\phi = 0.72$.

power, *i.e.* the work received from the external driving field, and the power dissipated in the rupture of capillary bridges. Both quantities are almost constant in time and match within a small relative error. This corroborates the stationarity of the fluidized state on the one hand and validates the simulation code on the other hand¹. The results and a detailed discussion of the power balance is found in Appendix B.

4.2.2 Fluidized-to-solid transition

In the last sections, we showed that once the external driving force is applied to the assembly of wet disks the system eventually reaches either a solid or fluidized state after a certain relaxation time. The final state depends on the magnitude of the external field. This observation immediately poses a number of questions: What is the smallest amplitude F_0^{min} of the external force field for the system to reach a fluidized state? Does the fluidization point change if we start the simulation from a solid state at small F_0 ? And, does the system solidify at the same point if we start with a fluidized system at a sufficiently large F_0 .

Besides the conditions under which the initial state of the system is created there are four

¹A detailed discussion is given in Chapter B

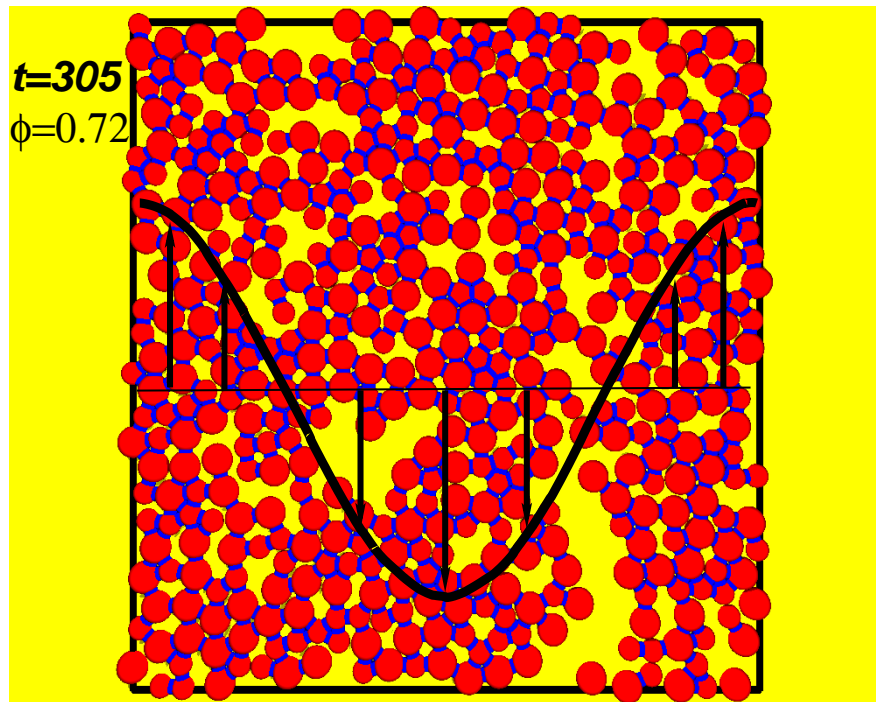


Figure 4.5: Snapshot of the system at $t = 305$ where the system reaches a fluidized state. The spatial variation of the external driving force is illustrated by the black curve. The number of particles is $N = 506$, the system size $L = 18$, the rupture separation $S_c = 0.01$, and the area fraction $\phi = 0.72$.

obvious control parameter of the system: the amplitude of the driving force F_0 , the global area fraction of disks ϕ , the system size L , and the rupture length of the capillary bridges S_c . To distinguish between the solid and the fluidized state we choose the average difference

$$\Delta v_y = \langle v_y \rangle_{x=L} - \langle v_y \rangle_{x=L/2}, \quad (4.2)$$

of the y-components of drift velocities at the side of the box, $\langle v_y \rangle_{x=L}$, and in the center of the box, $\langle v_y \rangle_{x=L/2}$, as an order parameter of the transition. Here, we assume that the system follows the symmetry of the external field, *i.e.* that there will be non component of the drift velocity into the x-direction. This assumption has to be checked during the simulation. If the final state is solid, the disks move as a rigid body and we have $\Delta v_y = 0$. If the material is partially or fully fluidized we should observe $\Delta v_y \neq 0$.

Figure 4.6 shows the order parameter Δv_y as a function of time for a series of amplitudes of the external force $F_0 = \{4.5 \cdot 10^{-3}, 8 \cdot 10^{-3}, 8.5 \cdot 10^{-3}\}$. In those cases, the system can be found in a transient fluidized state before it finally reaches a permanent solid state at times larger than $\Delta t_{relax} \approx \{33, 180, 180\}$, respectively. Here, Δt_{relax} is the relaxation time during which the disks rearrange and build a network of capillary bridges that can bear the applied shear stress. However, at amplitude of the external force $F_0 = \{9 \cdot 10^{-3}, 1.3 \cdot 10^{-2}, 1.8 \cdot 10^{-2}\}$, we observe a relaxation into a fluidized state, cf. Fig.4.6.

The order parameter as function of the strength of the external field is shown in Fig. 4.7. For solid states we have $\Delta v_y = 0$. For the fluidized states, a long time average of the order parameter is computed, cf. Fig. 4.6. It is rather obvious that the transition from the fluidized state to the solid state is a *discontinuous transition*. The order parameter as function of the control parameter is obtained via the inverse function $F_0 = C_0 + C_1 \Delta v_y + C_2 \Delta v_y^2 + C_3 \Delta v_y^3 + O(\Delta v_y^4)$ with $C_0 = 0.03798$, $-C_1 = 0.1377$, $C_2 = 0.1875$, and $C_3 = -0.0667$ shows that the drift velocity exhibits a square root scaling with a finite offset at the transition point. According to the fit, the transition point is approximately at an amplitude of the external force of $F_c = 8.75 \cdot 10^{-3}$.

Accordingly, the transition of the system from the fluidized to the solid state appears to be a subcritical bifurcation of dynamic states [75]. Hence, we expect that the branch of solid states continues to amplitudes of the external force being larger than the value at the solidification transition at F_c .

Since the transition point is the smallest driving amplitude where the system ends up in a fluidized state and since for driving amplitudes slightly smaller than F_c the system reaches

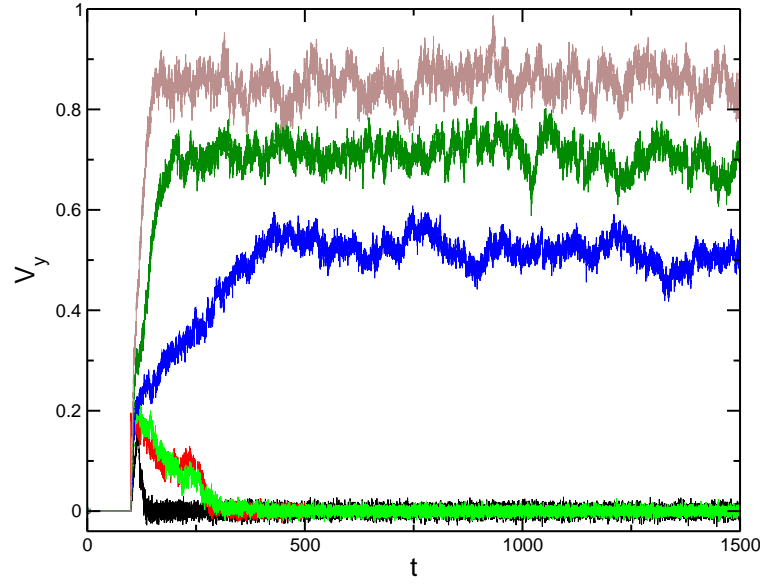


Figure 4.6: The order parameter Δv_y as a function of time for solid and fluidized states. The black, red and green curves correspond to an amplitude of the external force $F_0 = \{4.5 \cdot 10^{-3}, 8 \cdot 10^{-3}, 8.5 \cdot 10^{-3}\}$ where the system is found in a solid state. The blue, dark green, and brown curves correspond to $F_0 = \{9 \cdot 10^{-2}, 1.3 \cdot 10^{-2}, 0.18 \cdot 10^{-2}\}$, respectively, where the system is in a fluidized state. The total area fraction is $\phi = 0.7$, the system size $L = 18$, the number of particles $N = 506$, and the rupture separation $S_c = 0.01$.

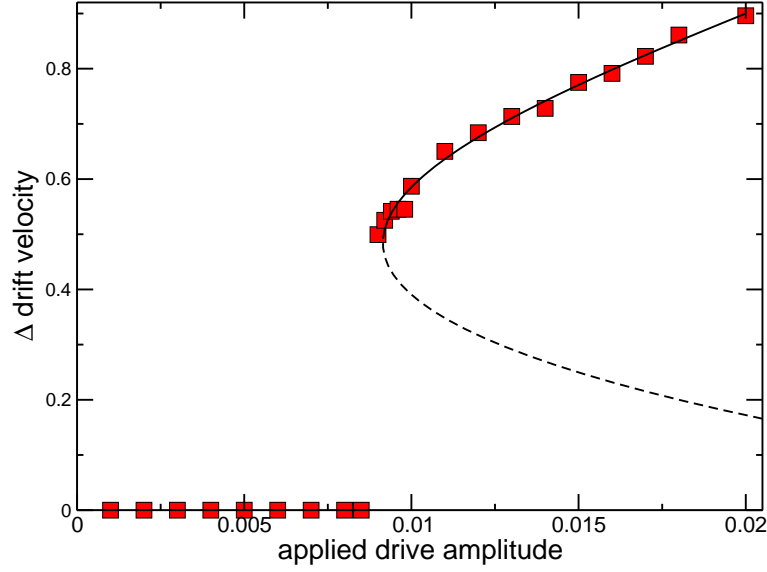


Figure 4.7: Illustration of the fluidized-to-solid transition. In the fluidized state, the drift velocity shows a square root scaling close the the transition point. The total area fraction is $\phi = 0.7$, the system size $L = 18$, the number of particles $N = 506$, and the rupture separation $S_c = 0.01$.

a final solid state, we argue that the transition which is depicted in Fig. 4.7 is a transition between a stationary fluidized state and a solid state.

There are several open question about this fluidized-to-solid transition: Is the solidification under an applied shear stress due to a jamming of disks, *i.e.* is there a build up of permanent compressive forces chains which prevent moving of the disks? Does the fluidized-to-solid transition depend on the rupture distance S_c of the capillary bridges? Does the system size L influence the critical transition point? How does the transition point depend on the total area fraction ϕ ? If one starts from a solid state, is there a solid-to-fluidized transition, and if so, does this transition occur at the same value of driving strength F_0 ? We will address those questions in the sequel of this chapter.

4.2.3 Dry disks under external driving

We claimed that the fluidized-to-solid transition of wet disks being subject to an external driving force is due to the network of capillary bridges between the disks. To test this idea, we switch off the capillary bridge forces and apply the external driving force to an assembly of ‘dry’ disks. All the steps that are detailed in the protocol of the simulation for wet disks hold

also for the simulation of the dry disks, except that the minimal capillary force is set to zero.

To prevent heating, *i.e.* accumulation of kinetic energy in the system, an alternative dissipation mechanism is implemented. Here, we made use of an additional viscous force that is effective as long as two disks interact. The elastic part is still given by the non-linear spring force as outlined in chapter 1, section 1.2.2. The trajectories of the disks are obtained by solving Newtons equation of motion

$$m_i \frac{d^2 \mathbf{r}_i}{dt^2} = \sum_j \left[F_{ij}^r - \frac{\mathbf{v}_i - \mathbf{v}_j}{R_i + R_j} \cdot \mathbf{e}_{ij} \right] \mathbf{e}_{ij} + \mathbf{F}^{ex}, \quad (4.3)$$

where m_i and \mathbf{r}_i are the mass and position of disk i , F_{ij}^r is the non-linear spring repulsive force, R_i and R_j are the radii of the disks, \mathbf{v}_i and \mathbf{v}_j are the corresponding velocities, $\mathbf{e}_{ij} = (\mathbf{r}_i - \mathbf{r}_j)/|\mathbf{r}_i - \mathbf{r}_j|$ the unit vector pointing from particle i to particle j , and \mathbf{F}^{ex} the external driving force. The sum \sum_j runs over all disks j that overlap with i .

Figure 4.8 shows the order parameter Δv_y as a function of the applied driving amplitude F_0 . We probed six decades of the driving amplitude, starting from $F_0 = 10^{-5}$ and ending at $F_0 = 1$, and computed the corresponding order parameter Δv_y once a stationary state has been reached. In contrast to the dry case we still find the assembly of disks in a fluidized state at the smallest amplitude $F_0 = 10^{-5}$ of our simulations, and no transition between a fluidized and a solid state. The order parameter as function of the driving strength presented in Fig. 4.8 is well described by a power law

$$\Delta v_y = A F_0^\eta, \quad (4.4)$$

with $A = 9.24$ and $\eta = 0.64$. This shows that the order parameter Δv_y should be zero only if the applied driving force is switched off. As long as the control parameter F_0 is not equal to zero the system is in the fluidized state.

This is a clear proof that assemblies of frictionless viscoelastic disks under isochoric conditions do not exhibit a yield stress below the limit of random close packing. However, if one introduces a hysteretic short ranged attractive interaction such as the minimal capillary force, the system will develop a yield stress below the limit of random close packing.

4.3 Distribution of physical quantities

Applying a spatially heterogeneous force to the assembly of disks will lead to a heterogeneous distribution of observables in the system. As mentioned at the end of section 4.1 we expect the

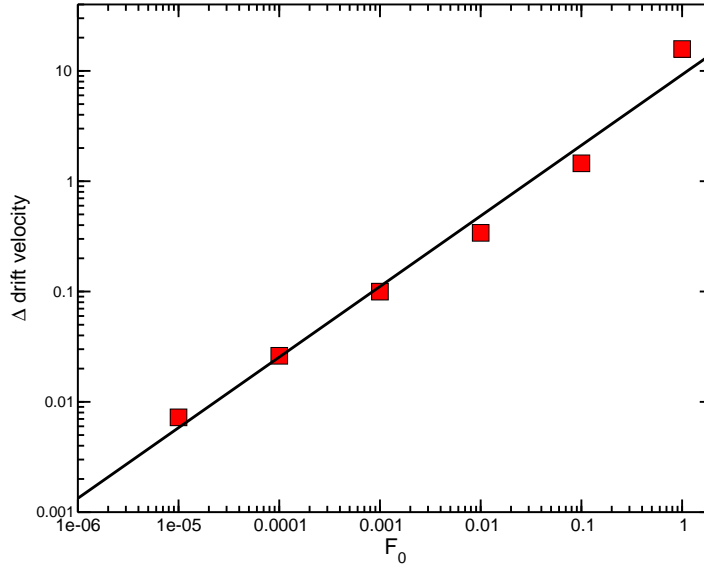


Figure 4.8: ΔV_y as a function of the amplitude of the external driving force F_0 for viscoelastic disks without capillary bridges. The system is fluidized and no transition from a fluidized to solid state is observed. The total area fraction is $\phi = 0.70$, the system size $L = 18$, the number of particles $N = 506$, and the rupture separation $S_c = 0.01$.

system to follow the symmetry of the external field at small amplitudes of the driving force. The exact shape of the profiles is determined by the dissipation rate, *i.e.* the rupture frequency of capillary bridges. On the one hand the dissipated power depends on the local shear rate, $\dot{\gamma}$, the local granular temperature, T_G , and the local density of disks, ρ , and, on the other hand on the transport coefficients of energy and momentum, *i.e.*, heat conductivity and viscosity, respectively. The latter will also depend on $\dot{\gamma}$, T_G and ρ . In particular, we will focus on the local viscosity of the wet disk fluid.

In the sequel we present spatial profiles and probability distributions of certain observables in both the solid and the fluidized state. If not explicitly stated, the system size is set to $L = 40$, the number of particles to $N = 1540$, while the the rupture separation is $S_c = 0.01$. The total area fraction equals $\phi = 0.70$.

4.3.1 Profiles of drift velocity and shear rate

Figure 4.9(left) shows a comparison of the time averaged drift velocity $\langle v_y \rangle$ into the y-direction as function of the lateral position x in the solid and fluidized state. The black circles show the velocity profile in the solid state where the amplitude of the external force is set to $F_0 = 1 \cdot 10^{-3}$

F_0	A_0	A_1	A_2	A_3
0.0066 (red)	-0.0405	0.8181	-0.11023	0.02086
0.0132 (blue)	0.084	1.1571	-0.104	0.00117

Table 4.2: Fitting parameters of co-sinusoidal harmonics on velocity profiles corresponding to two different applied driving amplitudes.

and the drift is almost zero. Squares and diamonds indicate the velocity profile in the fluidized state for amplitudes of the external force $F_0 = \{6.6 \cdot 10^{-3}, 1.32 \cdot 10^{-2}\}$, respectively. It is apparent that a harmonic or, to be precise, a cosine shaped velocity profile does not fit the simulation data. Therefore we employ the second and third odd harmonics

$$\langle v_y \rangle(x) = A_0 + A_1 \cos\left(\frac{2\pi x}{L}\right) + A_2 \cos\left(\frac{6\pi x}{L}\right) + A_3 \cos\left(\frac{10\pi x}{L}\right) \quad (4.5)$$

where L is the system size. One sees that the red and blue curves fit perfectly to the data. The fitting coefficients are obtained as: Coefficients of the second and third odd harmonics decrease as one increases the amplitude of the external driving. This observation tells us that the spatial variation of the drift velocity approaches the profile of the external driving force at height driving strength.

Figure 4.9(right) shows the local shear rate as a function of the lateral position. Because the drift velocity $\langle v_x \rangle$ into the direction of the applied external force is zero the local shear rate can be simply obtained as the spatial derivative $\dot{\gamma} = \partial_x \langle v_y \rangle$. The black curve shows the shear rate in the solid state in which $F_0 = 1 \cdot 10^{-3}$ while the red and blue curves display the shear rate in the fluidized state where $F_0 = \{6.6 \cdot 10^{-3}, 1.32 \cdot 10^{-2}\}$ respectively. The shear rate has a maximum at the inflexion points of the drift velocity profile where $\langle v_y \rangle \approx 0$. The shear rate increases as the applied driving amplitude increases. Furthermore, the width of shear rate curve also increases by increasing the applied driving amplitude. The shear rate in the solid state is on the order of $\dot{\gamma} \approx 10^{-5}$, which shows that the shear rate is negligible in the system.

4.3.2 Area fraction and granular temperature

Figure 4.10(left) shows the local area fraction ρ as a function of the lateral position x for both a solid and a fluidized state. The blue curve is the local area fraction of the solid state for

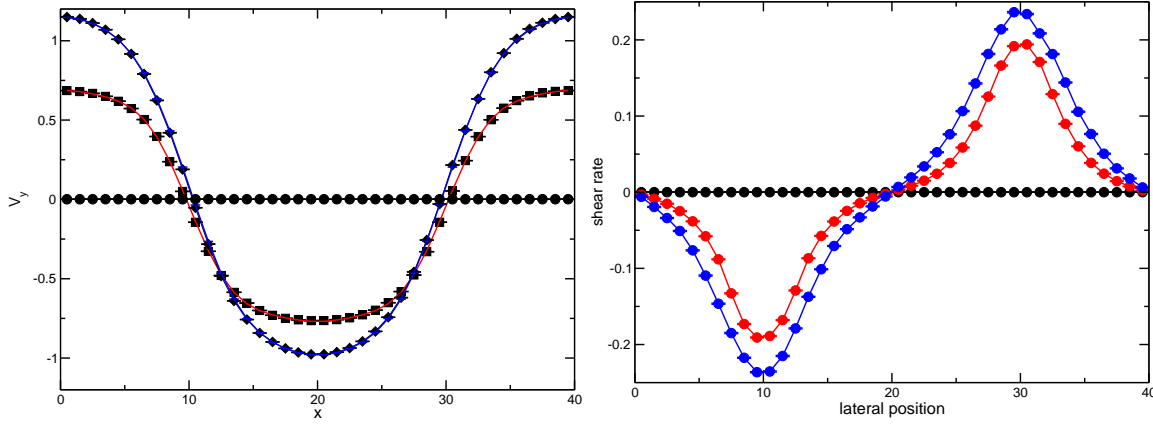


Figure 4.9: (Left) Drift velocity $\langle v_y \rangle$ as function of the lateral position x in the solid (black) and fluidized (red and blue) states. (Right) shear rate as function of the lateral position. The applied driving amplitudes are $F_0 = \{1 \cdot 10^{-3}, 6.6 \cdot 10^{-3}, 1.32 \cdot 10^{-2}\}$ for the black, red, and blue curve respectively. The total area fraction is $\phi = 0.7$, the rupture separation $S_c = 0.01$, and the system size $L = 40$.

$F_0 = 10^{-3}$. The average of the blue curve equals $\bar{\rho} = 0.7$ which is the total area fraction ϕ of the system. The width of the fluctuation around the average value is about 14% of the total area fraction ϕ . Therefore, one can conclude that the system is homogeneous in the solid state.

The top black and red curves show the local area fraction ρ in the fluidized state for amplitudes of the external driving force $F_0 = \{6.6 \cdot 10^{-3}, 1.32 \cdot 10^{-2}\}$, respectively. The local area fraction attains a minimum where the shear rate has a maximum, *i.e.* at about $x \approx 10$ and $x \approx 30$. However, at $x = 0$ and $x = 20$, where the shear rate is in a minimum, disks accumulate. The local density around those points is about $\rho \approx 0.8$. Since this value is smaller than the value at random close packing $\phi_{RCP} \approx 0.84$, these disks are still mobile. The local area fraction in the dense regions does not change significantly as the driving strength is increased while the local area fraction increases in the dilute regions.

One may suspect that in the fluidized state the small and large disks of the bidisperse mixture segregate, as it the case in the ‘dry’ and ‘wet’ brazil nut effect, cf. Refs. [76, 77]. Therefore, we calculated the local area fraction for small and large disks separately. The result is shown in Fig. 4.10(left). The bottom curves show the area fraction for the small disks and the central curves show the area fraction for the large disks (the color code is same as for the top curves). Both the area fraction for small and for large disks exhibit the same trend and as one increases the amplitude of the external force (red curves), the trend does not significantly change. Therefore, bidisperse disks do not segregate in the fluidized state.

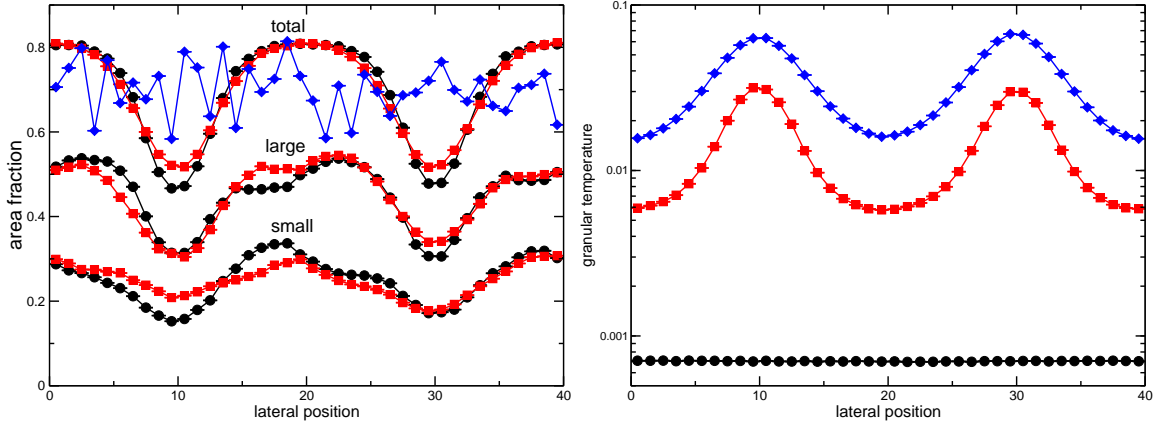


Figure 4.10: (Left-top) the local area fraction for the solid (blue) and fluidized states (black and red). The local area fraction for large and small disks depicted in left-middle and left-bottom. (Right-top) the granular temperature as a function of the lateral position for two fluidized states. (Right-top) the granular temperature as a function of the lateral position for solid state. The total area fraction is $\phi = 0.7$, the rupture separation is $S_c = 0.01$, and the system size is $L = 40$.

Profiles of the local granular temperature are illustrated in Fig. 4.10(right). The black curve shows that the granular temperature in the solid state does not depend on the lateral position and that the granular temperature is non-zero. Compared to the solid state the granular temperature increases one order of magnitude in the fluidized state. The spatial distribution of the granular temperature has two maxima which coincide with the maxima of the shear rate, *i.e.* at around $x = 10$ and $x = 30$. For the particular values of the control parameter in our example the ratio between the amplitude of the external driving amplitudes is almost two. The ratio of the granular temperatures, however, is approximately five. This significant change in the granular temperature between the solid and fluidized state shows the dramatic difference concerning the granular temperature.

4.3.3 Liquid bridge number and rupture frequency

In addition to the drift velocity, the local area fraction and the granular temperature we calculated the density of capillary bridges and their rupture frequency as function of the lateral position. Figure 4.11(left) displays profiles of the density of capillary bridges. In the solid state (black curve) this density does not depend on the lateral position and we find an average number of capillary bridges per disk of $\bar{N}_{LB} = 4$. The red and blue curves in Fig. 4.11 display

the number of capillary bridges in the fluidized state for amplitudes $F_0 = \{6.6 \cdot 10^{-3}, 1.32 \cdot 10^{-2}\}$ of the external driving force. A comparison of Fig. 4.10 and Fig. 4.11(left) shows that the local average number of capillary bridges per disk, \bar{N}_{LB} , exhibits the same behavior as the local area fraction, ρ . The average number of capillary bridges per disk reaches $\bar{N}_{LB} \approx 4$ in the solid state (black curve) where the local area fraction is $\rho \approx 0.8$ at around $x = 0$ and $x = 20$ in the solid state (black curve). The number of capillary bridges per disk decreases until $N_{LB} \approx 1$ where the system is rather dilute with a local area fraction of $\rho \approx 0.45$. The total number of capillary bridges in the system decreases by increasing the amplitude of the external driving force.

Figure 4.11(right) illustrates the rupture frequency of capillary bridges as a function of the lateral position. One may expect that there would not be any rupture event in the solid state. However, there are some rare rupture events, and the black curve shows that the spatial distribution of these events is homogeneous. The red and blue curves show the rupture frequency in a series of fluidized states at $F_0 = \{6.6 \cdot 10^{-3}, 1.32 \cdot 10^{-2}\}$, respectively. The rupture frequency decreases more than two orders of magnitude as the material transforms from the fluidized state to the solid state. In general, the rupture frequency in the fluidized state is heterogeneously distributed and attains its maximum where the system is dilute and hot. The global rupture frequency in the system increases as one increases the amplitude of the external driving force.

A data collapse of the local number of capillary bridges per disks as a function of the local area fraction is displayed in Fig. 4.12. The data were obtained from a series of simulations for a system size of $L = 40$. We chose values for the amplitude of the driving force $F_0 = \{F_s, 1.5 F_s, 2 F_s, 3 F_s\}$, where F_s is the amplitude at the solidification transition. The total area fraction was varied between $\phi = 0.62$ and $\phi_{RCP} = 0.84$, while the rupture separation was $S_c = 0.01$ in all simulations. The color code indicates the granular temperature.

On the one hand, the number of capillary bridges per disk, N_B , shown in Fig. 4.12 displays a well defined boundary to small values of N_B where a large fraction of the data points accumulate. On the other hand, N_B does not exceed 4.1 while the local density stays below $\rho \approx 0.85$. These values coincide with the number of contacts in a isostatic packing of frictionless hard disks (*i.e.* in two dimensions), and the limit of random close packing $\phi_{RCP} = 0.84$ for the bidisperse mixture used in our simulations.

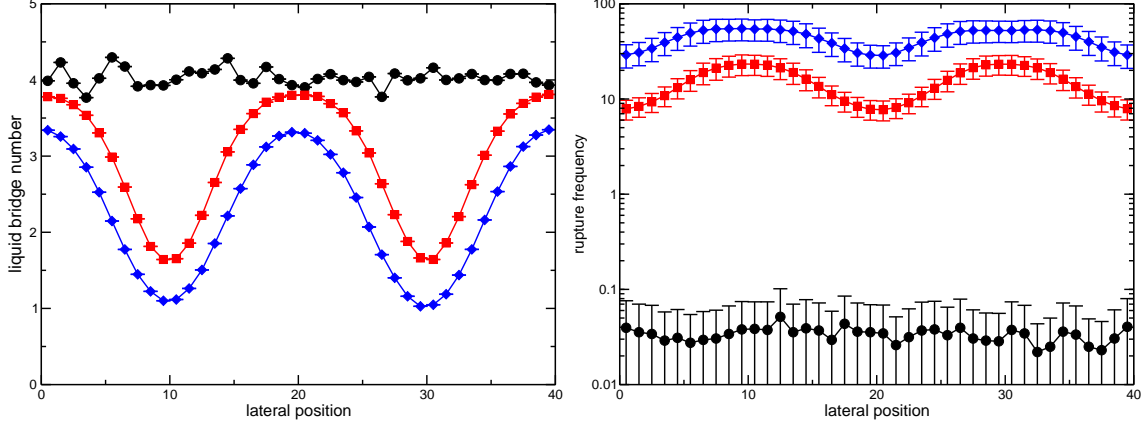


Figure 4.11: (Left) Average number of capillary bridges as function of the lateral position for a solid (black) and a fluidized (red and blue) state. (Right) Average rupture frequency as function of the lateral position. The color code is the same as for the left plot. The total area fraction is $\phi = 0.7$, the rupture separation $S_c = 0.01$, and the system size $L = 40$.

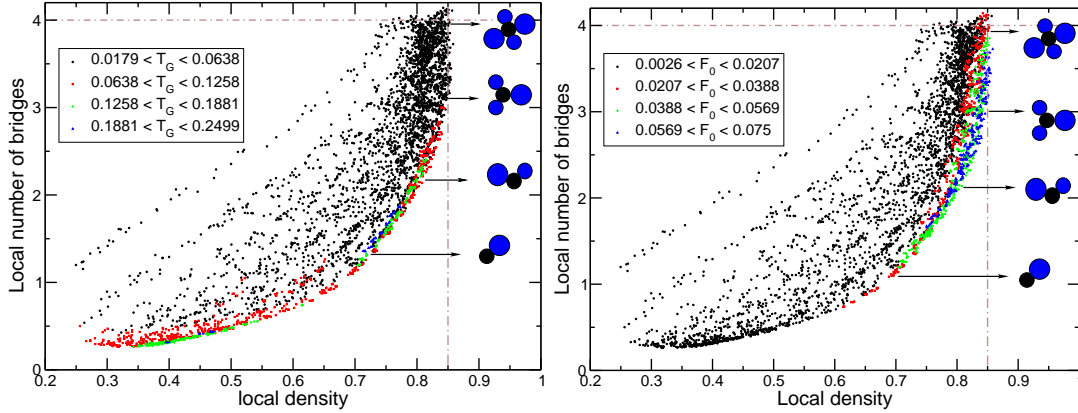


Figure 4.12: (Left) Local liquid bridge number as a function of the local area fraction for the fluidized wet discs. The data are sorted according to their local granular temperature. The hottest points form a well defined boundary. (Right) Local liquid bridge number as a function of the local area fraction for the fluidized wet discs. The data are sorted according to their applied driving amplitude. Two limits are found: 4 liquid bridges, and the random-close packing. System size $L = 40$, and rupture separation $S_c = 0.01$.

4.3.4 Stress field

Figure 4.13(right) shows components of the stress tensor in the solid state for an amplitude of the driving force of $F_0 = 10^{-3}$. The red squares are simulation data of the shear stress S_{xy} as a function of the lateral position x . In a stationary state the shear stress caused by the applied driving force $\mathbf{F}^{ex}(x) = \mathbf{e}_y F_0 \sin(2\pi x/L)$ can be calculated from a balance of forces. Assuming a homogeneous density n of particles per area one obtains

$$S_{xy}(x) = \frac{n L F_0}{2\pi} \sin\left(\frac{2\pi x}{L}\right), \quad (4.6)$$

where L is the system size. A derivation of equ. (4.6) can be found in the appendix 4.5.1.

Inserting numbers into the prefactor of equ. (4.6) leads to an estimate

$$\frac{n L F_0}{2\pi} \approx 0.006, \quad (4.7)$$

which is depicted by the black curve. The calculated shear stress fits quite well to the shear stress that has been directly measured in the simulation. The diagonal elements of the stress tensor, S_{xx} and S_{yy} , are depicted in the inset as black and blue curves. Compared to S_{yy} , the stress component S_{xx} exhibits smaller spatial fluctuations and does not depend on the lateral position. This finding is as expected since the stationary state follows the symmetry of the external field. The latter observation together with the continuity of momentum transfer into x -direction leads to the conclusion that the stress component S_{xx} has to be independent on x (it is trivial to mention that none of the stress components depend on y).

Figure 4.13(right) shows components of the stress tensor in the fluidized state. The red squares indicate the shear stress as a function of the lateral position. It appears that the shear stress has a sinusoidal shape as well but because the system is heterogeneous one cannot use equ. (4.6) to explain the profile of the shear stress. As one expects S_{xx} corresponding to the back curve does not depend on the lateral position x . The remaining diagonal element S_{yy} has two maxima around $x = 10$ and $x = 30$ coinciding with the maxima of the granular temperature. A comparison of the profiles for S_{xx} and for S_{yy} clearly demonstrates that the pressure field is not isotropic.

As mentioned before, the system becomes heterogeneous in the fluidized state and the number of disks per unit area, n , depends on the lateral position x . Starting from the general

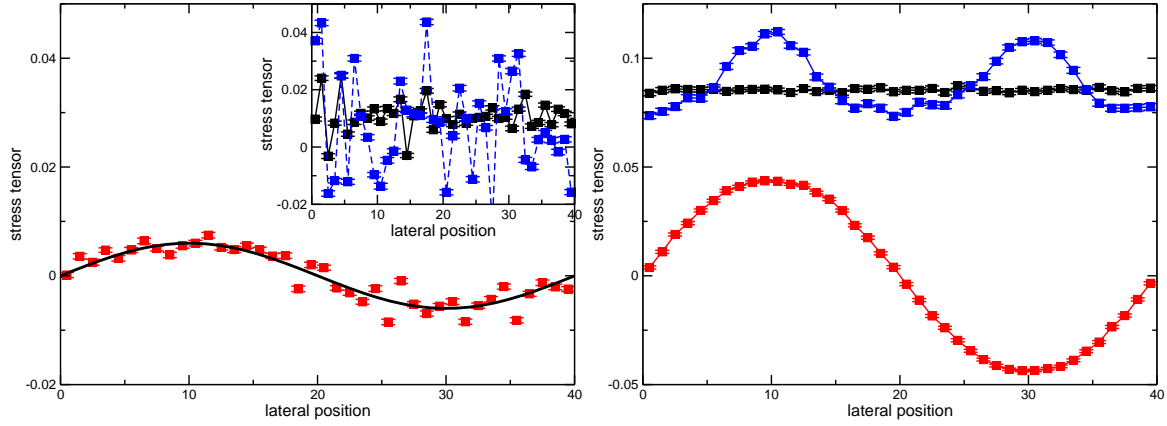


Figure 4.13: (Left) Profiles of components of the stress tensor in the solid state for $F_0 = 10^{-3}$. Red squares are simulation data of the shear stress while the solid black curve is a prediction according to equ. (4.9). The inset shows the diagonal elements S_{xx} and S_{yy} of the stress tensor. (Right) profiles of components of the stress tensor in the fluidized state at $F_0 = 6.6 \cdot 10^{-3}$. The red, black, and blue squares correspond to S_{xy} , S_{xx} , and S_{yy} . The total area fraction is $\phi = 0.7$, the rupture separation $S_c = 0.01$, and the system size $L = 40$.

form of the transport equation of momentum one arrives at the simple form

$$\partial_x S_{xy}(x) = n(x) F_y(x) \quad (4.8)$$

for a stationary state being homogeneous into y -direction and with $F_x = 0$. Details of the derivation can be found in Appendix 4.5.1.

Integration of equ. (4.8) leads to a shear stress

$$S_{xy}(x) = \int_0^x d\tilde{x} n(\tilde{x}) F_y(\tilde{x}) + S_{xy}^0. \quad (4.9)$$

Periodic boundary conditions in principle allow the constant S_{xy}^0 to be non-zero. Inspection of our simulation data shows that S_{xy}^0 equals zero within statistical errors. Equation (4.9) can be solved numerically as the number density $n(x)$ can be calculated directly from the simulation. Figure 4.14 displays n as a function of the lateral position x .

The red curve shown in Fig. 4.15 shows the numerical solution of the integral equ. (4.9) while the black circles correspond to direct measurements of S_{xy} from the simulation. One observes that the red curve fits onto the black circles. Therefore, equ. (4.9) is well suited to describe the relation between the applied driving force and the shear stress in the fluidized state.

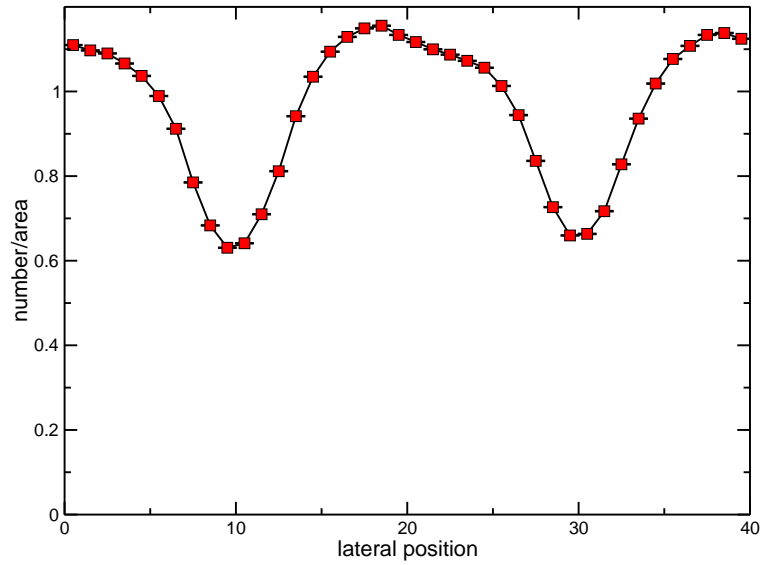


Figure 4.14: The number of particles per unit of area, n , in the fluidized state. The total area fraction is $\phi = 0.7$, the rupture separation $S_c = 0.01$, the amplitude of the external force $F_0 = 6.6 \cdot 10^{-3}$, and the system size $L = 40$.

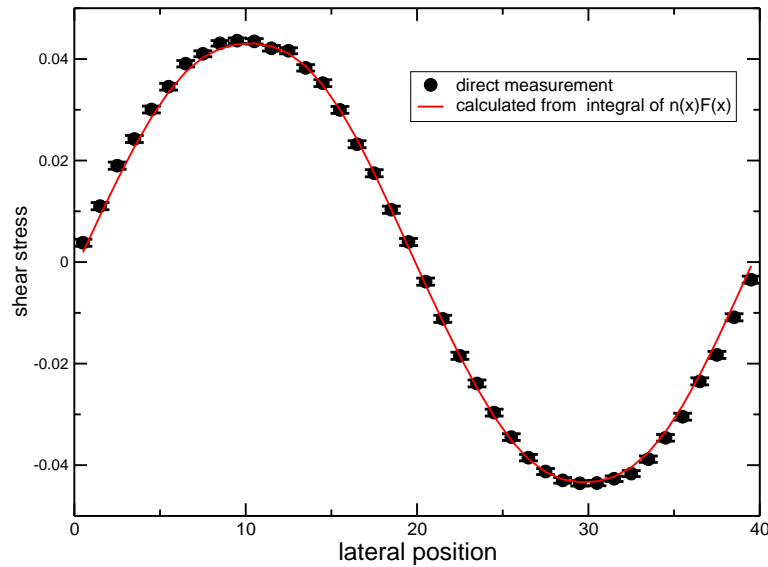


Figure 4.15: The black circles show the direct measurements of the shear stress in the fluidized state while the red curve corresponds to the integral equ. (4.8). The total area fraction is $\phi = 0.7$, the rupture separation $S_c = 0.01$, the applied driving amplitude $F_0 = 6.6 \cdot 10^{-3}$, and the system size $L = 40$.

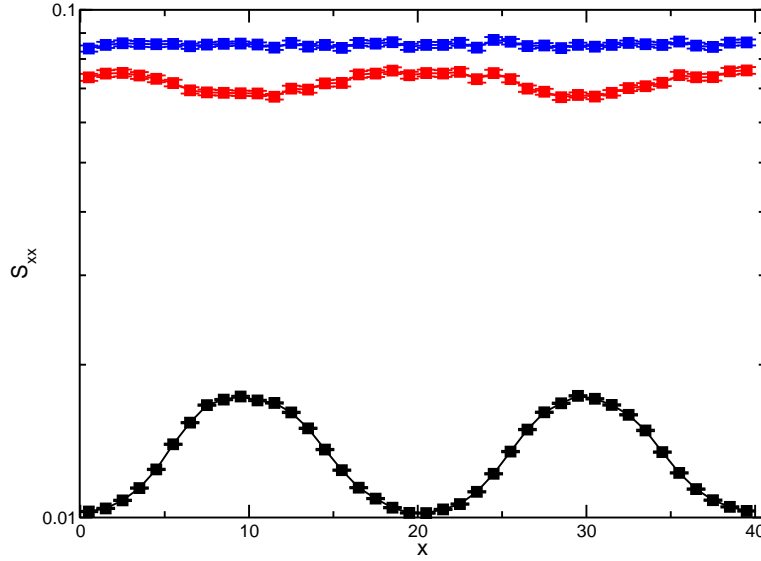


Figure 4.16: The black, red, and blue squares are the kinetic, static, and total stress component S_{xx} as function of the lateral position x in the fluidized state. The total area fraction is $\phi = 0.7$, the rupture separation $S_c = 0.01$, the applied driving amplitude $F_0 = 6.6 \cdot 10^{-3}$, and the system size $L = 40$.

The stress tensor can be decomposed into two parts. This is, on the one hand, the kinetic part of the stress tensor which depends only on the momenta and velocity of the disks, and, on the other hand, the static part being fully determined by the position of the disks and their mutual forces. In our simulation we computed the spatial distribution of both parts separately. Because the driving force is applied into y -direction, one intuitively expects that S_{xx} does not depend on the lateral position. The blue squares in Figure 4.16 show that the total stress component S_{xx} is indeed independent on x . As mentioned before this observation can be explained by the continuity of the momentum flux.

However, the kinetic part of the component S_{xx} as indicated by the black squares in Fig. 4.16 is position dependent and appears to be correlated to the local granular temperature. For the total area fraction of $\phi = 0.70$, the static part is approximately six times larger than the kinetic part. Because the disks are in enduring mutual contact and because the inter-particle diffusion of the disks is rather slow the static part of the stress tensor should be the dominant contribution in the total momentum transfer.

In Figure 4.17 the kinetic and static parts of the stress component S_{yy} as well as their sum is depicted by black, red, and blue squares, respectively. The kinetic part exhibits two maxima, one at $x = 10$ and a second at $x = 30$, similar to the spatial distribution of granular

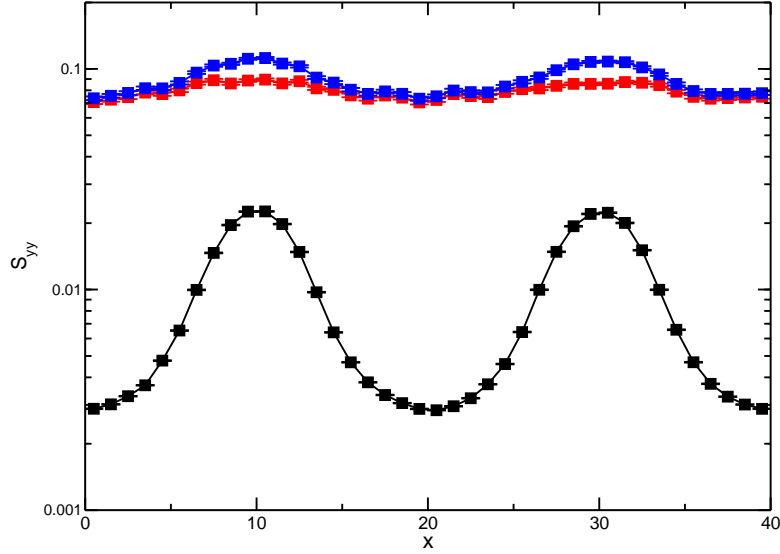


Figure 4.17: The black, red, and blue squares are the kinetic, static, and total S_{yy} versus the lateral position in fluid state. The total area fraction is $\phi = 0.7$, the rupture separation is $S_c = 0.01$, the applied driving amplitude is $F_0 = 6.6 \cdot 10^{-3}$, and the system size is $L = 40$.

temperature. The static part, which is almost one order of magnitude larger than the kinetic part increases at around $x = 10$ and $x = 30$. This observation is also true for the sum of both parts.

Figure 4.18 shows the kinetic, the static, and total shear stress S_{xy} as a function of the lateral position x as the black, red, and blue curve, respectively. As it was the case for the stress components S_{xx} and S_{yy} , the magnitude of the kinetic part is smaller than the magnitude of the static part. The kinetic part has a maximum at around $x = 10$ and $x = 30$ where the shear rate $\dot{\gamma}$ is maximal. The static part (red squares) increases as one approaches the center but reaches a plateau for $5.5 < x < 14.5$. For values $x > 14.5$ it decreases and approaches zero. The symmetry of the static part of S_{xy} in the first half of the simulation box is repeated in the second half, and there is again a plateau for $25.5 < x < 35.5$.

4.3.5 Viscosity

In a Newtonian fluid the shear stress is proportional to the local shear rate. The corresponding proportionality constant is the shear viscosity or simply the viscosity of the fluid ². Coming

²The second viscosity is related to a pressure contribution during a compressive or dilative motion of a compressible fluid

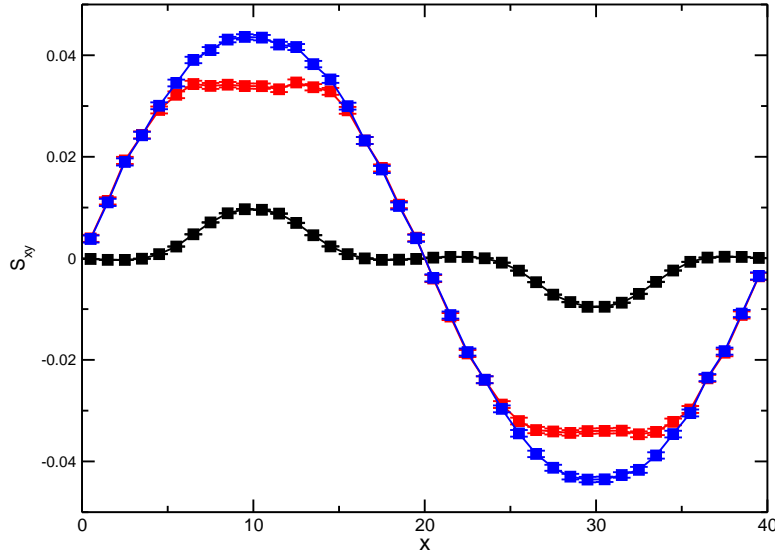


Figure 4.18: The black, red, and blue squares are the kinetic, static, and total shear stress S_{xy} as function of the lateral position x in fluidized state. The total area fraction is $\phi = 0.7$, the rupture separation $S_c = 0.01$, the applied driving amplitude $F_0 = 6.6 \cdot 10^{-3}$, and the system size $L = 40$.

from a microscopic picture one can define the viscosity as a transport coefficient related to the diffusion of momentum. In an ideal gas the viscosity increases with temperature because the average velocity of the gas particles increases with temperature which implies an increase of the collision frequency. Most liquids exhibit the opposite behavior. Their resistance against shearing decreases as the temperature increases. In a shear flow the liquid particles have to be thermally activated in order to change their relative position.

In this subsection we are going to discuss the viscosity of an assembly of fluidized wet disks under isochoric conditions. At first, we present the generic form of a viscosity profile in the fluidized state. A collapse of data from a series of simulations for different total area fraction and amplitudes of the driving force allows us to assess the dependence of the viscosity on the local area fraction and the granular temperature.

The viscosity of granular material is defined as the ratio of sum of off-diagonal elements of the stress tensor to twice of the shear rate [78]:

$$\eta = \frac{S_{xy} + S_{yx}}{2\dot{\gamma}}, \quad (4.10)$$

where S_{xy} and S_{yx} are the off-diagonal elements of the stress tensor, and $\dot{\gamma}$ is the local shear

rate. Because our particles are symmetric and frictionless, the stress tensor is symmetric and we have

$$\eta = \frac{S_{xy}}{\dot{\gamma}}. \quad (4.11)$$

Hence, the viscosity can be calculated as the ratio of the local shear stress to the local shear rate. The viscosity profile according to the definition equ. 4.11 is depicted in Fig. 4.19 for two amplitudes of the external force $F_0 = \{6.6 \cdot 10^{-3}, 1.32 \cdot 10^{-2}\}$ as red and blue squares, respectively. It is obvious that the viscosity decreases where the shear rate increases and vice versa. Errors become large around $x = 0$ and $x = 20$ where the shear rate is small.

To explore the dependence of the viscosity η on the density ρ and granular temperature T_G we employ a data collapse of a series of simulations for different total area fractions and driving strengths similar to the plot shown in Fig. 4.12. The parameter of the simulations are identical to those given in subsection 4.3.3.

Figure 4.20(top) displays the viscosity of the fluidized wet discs as a function of the local reduced area fraction $\rho_c - \rho$. The color code corresponds to the local granular temperature. It is apparent from Fig. 4.20(top) that the overwhelming majority of data points fall into a narrow band. The distribution of granular temperatures in this band seems not to follow a visible rule. A comparison to the dashed line, however, indicates an approximate scaling $\eta \sim (\rho_c - \rho)^{-1}$ of the viscosity with the local area fraction ρ .

Figure 4.20(bottom), however, shows the same data as in Fig. 4.20(top) but now the granular temperature is on the abscissa while the density is encoded in the color of the data points. In contrast to Fig. 4.20(top), the data points are spread over a wide region. From the distribution of colors one can anticipate the existence of isolines of constant local density ρ in the plane spanned by T_G and η . A comparison of the plots Fig. 4.20(top) and Fig. 4.20(bottom) reveals that the local density of disks has a much stronger impact on the viscosity compared to granular temperature. Furthermore, the viscosity appears to diverge when approaching the limit of random close packing at $\phi_{RCP} = 0.84$.

Interestingly, a similar divergence in the shear viscosity with an exponent around -1 was found by Luding *et al.* in a fluid of monodisperse elastic hard disks in thermal equilibrium [79]. The area fraction of disks at the divergence, however, is $\phi = 0.71 \pm 0.01$, *i.e.* much lower than the value of random close packing of our bidisperse disks. In addition to the divergence of viscosity, the coefficient of self diffusion tends to zero at the same area fraction [79].

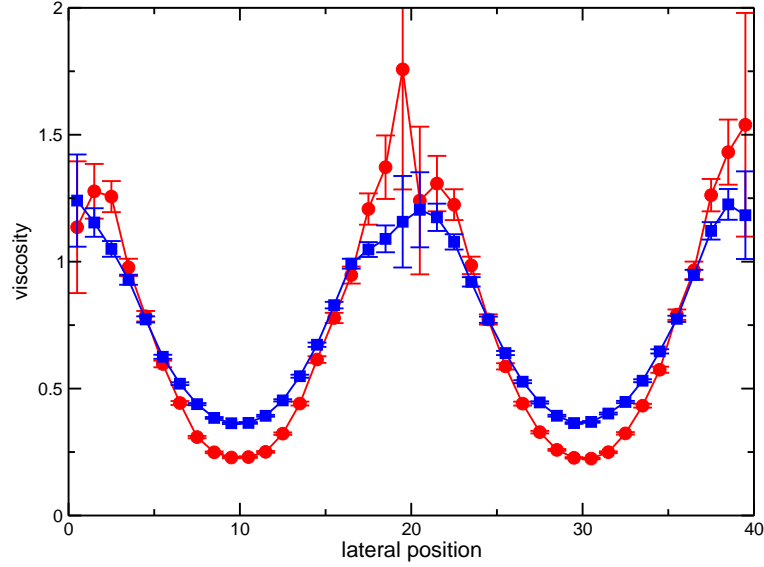


Figure 4.19: Viscosity η as function of the lateral position x in fluidized state. The red and blue squares correspond to amplitudes of the external force $F_0 = \{6.6 \cdot 10^{-3}, 1.32 \cdot 10^{-2}\}$ respectively. The total area fraction is $\phi = 0.7$, the rupture separation $S_c = 0.01$, and the system size $L = 40$.

4.3.6 Interparticle forces

The statistics of interparticle forces crucially determine the bulk properties of the assembly, *e.g.* its load bearing capability, sound transmission, and shock propagation [80–87]. In granular systems the stress transmission is spatially heterogeneous and occurs in the form of force chains [88–90]. Since the discovery of force chains the probability distribution of compressive forces in a granulate has been a subject of granular physics [91–93]. Several model calculations [94–96], computer simulations [97–99], and experiments on shear cells [100–102] have proven the existence of exponential tail in the limit of large compressive forces.

Studying of force distributions in granular material became of significant importance when the dynamic arrest in granular systems was linked to the presence of force chains between the grains. In Ref. [103] O’Hern *et al.* studied the distribution of normal contact forces near the jamming transition. They have found that the probability distribution of forces develops a peak whose height increases with increasing total packing fraction and decreasing shear stress. They propose that the appearance of that peak signals to development of a yield stress.

In our simulations we measured the probability distribution of interparticle forces for a series of total area fractions and amplitudes of the external driving force in both the fluidized and in the solid state. To obtain a satisfactory statistics we use a system size $L = 30$ with up to

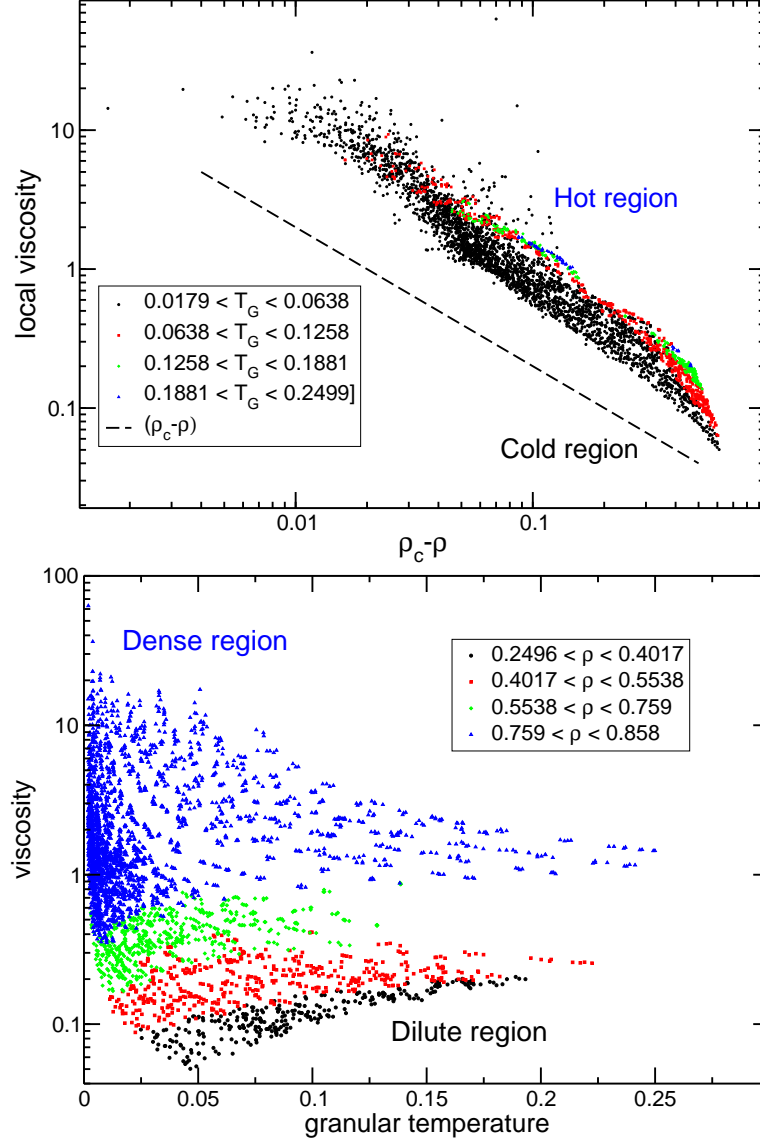


Figure 4.20: Local viscosity, η , as function of the local reduced area fraction, ρ (top) and granular temperature, T_G (bottom). The color encodes the local granular temperature (top) and the local density (bottom). The dashed line indicates a scaling $\eta \sim (\rho_c - \rho)^{-1}$. The system size is $L = 40$, and rupture separation $S_c = 0.01$.

$N = 1500$ disks. As it was mentioned in the last chapter, we solidify and fluidize the assembly of wet disks using a spatially heterogeneous external driving force.

Figure 4.21 shows the probability distribution $P(F)$ of normal force F between two disks. While our wet discs interact via attractive (negative sign) and repulsive (positive sign) forces, F varies from -1 until F_{max} . The smallest value of the force is given by $F_{min} = -1$ corresponding to a capillary bridge between two non-overlapping disks.

A finite fraction of the forces between two neighboring disks is due to the presence of a capillary bridge only. The corresponding pair of disks has collided in the past but does not overlap anymore. A finite fraction of all pairs of disks with a non-zero force exhibit such a ‘stretched’ capillary bridge. The probability to find a stretched capillary bridge is depicted in Fig. 4.22 as function of the amplitude of the external force and for a series of total area fractions. Here, we used the standard preparation protocol described in section 4.1.1 such that the system is initially in a fluidized state.

Inspection of Fig. 4.22 reveals a sharp drop of the number of stretched capillary bridges in the assembly of disks as the amplitude of the applied external force is lowered. Apparently, this drop is associated with the fluidized-to-solid transition. For total area fractions $\phi = 0.62$ and $\phi = 0.7$, we find a plateaus of the probability at $P \approx 0.38$ in the fluidized and a probability of $P \approx 0.24$ in the solid state, cf. Fig.4.22. At high total area fractions $\phi = 0.82$, however, the probability in both the fluidized and the solid state are significantly smaller. In addition, the drop appears to be ‘rounded off’, *i. e.* one observes a decrease in the probability in the fluidized state close to the step.

Moreover, we are interested in the spatial probability density to find the contact with the largest force in the system. Figure 4.23 shows the probability density in both the solid and the fluidized state. The green circles illustrate that an extreme event in the solid state can appear everywhere in the system because there is no a systematic dependence of the probability density on the lateral position. However, the red squares show that these extreme events in the fluidized state are localized where the shear rate and the granular temperature are maximal.

The observation that the largest force between disks is more or less equally distributed in the solid state can be viewed as a contradiction to continuum mechanics. One would expect that the extreme events are localized in regions where the magnitude of the stress components are large. This is indeed the case for the spatial distribution of extreme forces in the fluidized state. We can argue that this difference is due to chains of compressive forces between the disks which build up in the solid state. In the fluidized state, however, these force chains are absent or at least exist for such a short period of time that on average their effect cannot be

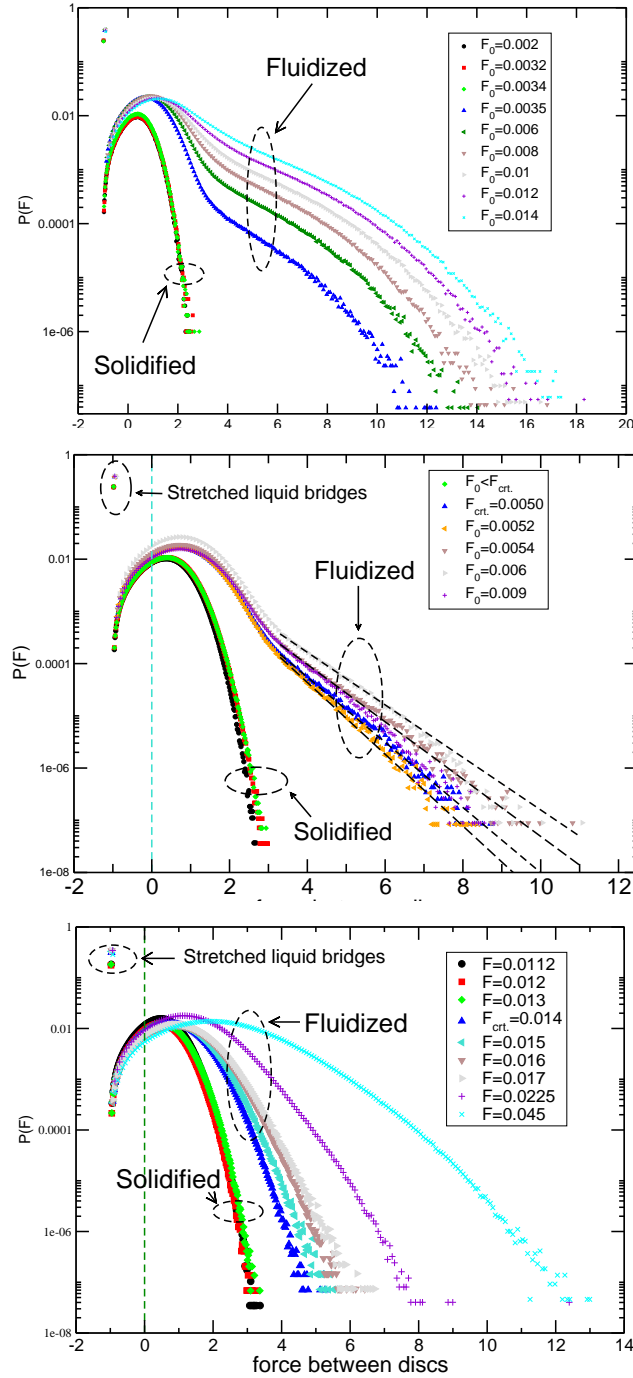


Figure 4.21: Probability distribution, $P(F)$, of normal forces F . (Top) The total area fraction is $\phi = 0.62$. In the solid state the distribution is semi-Gaussian. A shoulder appears in the fluidized state which is followed by an exponential tail to larger values of F . The amplitude of the external force at the solidification point is $F_s = 3.5 \cdot 10^{-3}$. (Middle) Area fraction $\phi = 0.70$ and force amplitude $F_s = 5 \cdot 10^{-3}$. The shoulder seen in (top) has disappeared. (Bottom) Area fraction $\phi = 0.82$ and force amplitude $F_s = 1.4 \cdot 10^{-2}$. No shoulder is visible.

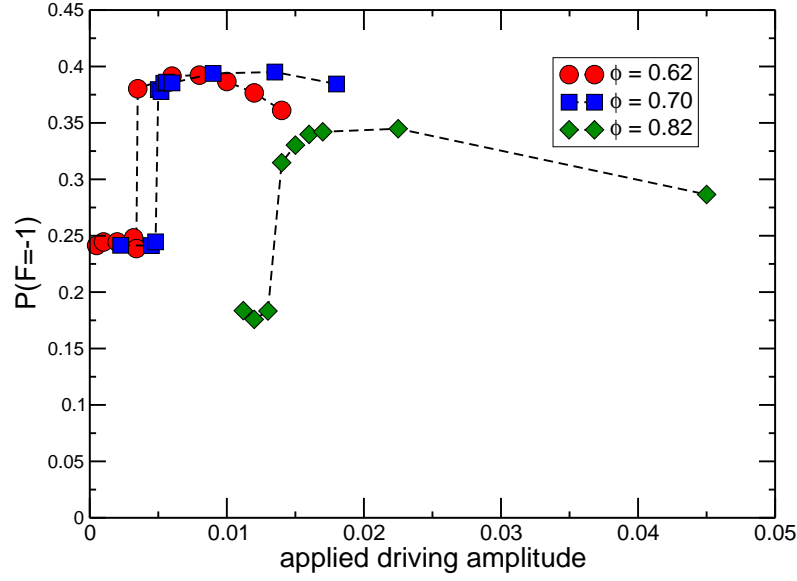


Figure 4.22: Probability to find a stretched capillary bridge among all pairs of interacting disks as function of the amplitude of the external force. A sharp transition is found for the fluidized-to-solid transition. The total area fraction are $\phi = \{0.62, 0.7, 0.82\}$ with corresponding amplitudes of the external force at the fluidized-to-solid transition are $F_s = \{3.5 \cdot 10^{-3}, 5.0 \cdot 10^{-3}, 1.4 \cdot 10^{-2}\}$. The system size is $L = 30$, the rupture separation $S_c = 0.01$.

observed.

4.4 Hysteretic transitions

In the last chapter we observed that wet disks on an inclined plane go through a hysteretic fluidization transition as the inclination angle is changed. In other words, there is a range of control parameter where the dynamic state of the system is not uniquely defined by the values of the control parameter. The system can be found in one out of two or more possible dynamic states.

The observation made for wet disks on an inclined plane poses the important question whether the hysteresis of the solid-to-fluidized transition is a universal property of wet disks. Does this hysteresis depend on the driving mechanism that shears the system? Is the hysteresis caused by the fact that the capillary bridge interaction is itself a hysteretic interaction?

Let us first explain how we will explore the existence of a hysteretic transition under isochoric conditions. The initial driving amplitude should be large enough to go beyond the fluidized-to-solid transition, the system eventually should reach fluidized state. Afterwards,

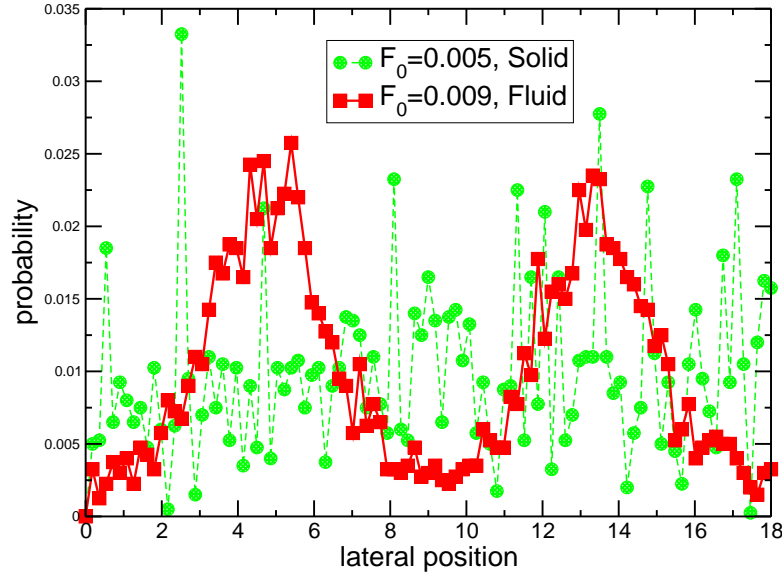


Figure 4.23: Spatial probability density to find the strongest force between two disks as function of the lateral position. The extreme events are randomly distributed in the solid state (green circles). However, in the fluidized state (red squares), these extreme events are localized where the shear rate has its maxima. The total area fraction is $\phi = 0.70$, the number of particles $N = 506$, and the rupture separation $S_c = 0.01$.

we decrease the amplitude of the external force in small steps. At each step we give the system enough time to let the system reach a stationary state. The magnitude of the steps should be sufficiently small. Large changes in the external force would pose a perturbation to the system.

Starting from a stationary fluidized state at high external driving force we continuously decrement its magnitude until the material has fully solidified. The value of the amplitude of the external force at which the material solidifies is shown by F_s . Once the material is solidified, we again increase the magnitude of the external force in small steps. A solid-to-fluidized transition should occur while increasing the external force when the shear stress in the system exceeds the yield stress of the disk packing. The corresponding amplitude of the external force at which the material fluidizes is denoted by F_f . Whenever we find that F_f is larger than F_s and we will be able to say whether hysteresis exists in this system.

In order to answer this question we chose our standard simulation parameter, *i.e.* we set the total area fraction to $\phi = 0.70$, the rupture separation to $S_c = 0.01$, the number of particles to $N = 506$, and the system size to $L = 18$. Figure 4.24 shows the order parameter Δv_y as a function of the time. The initial amplitude of the external force is $F_0 = 8.8 \cdot 10^{-3}$. For this setting the relaxation time of the system to reach a stationary fluidized state is approximately

$\Delta t_{relax} \approx 4 \cdot 10^2$. After each decrement of the applied driving amplitude we waited a time $\Delta t_{step} = 10^3$. The step width of the external force was $\Delta F_{step} = 2 \cdot 10^{-4}$. The red curve shows Δv_y as function of time while decrementing F_0 while the violet curve shows the amplitude of the external force as function of time. The amplitude of the external force is decremented until $t = 4 \cdot 10^3$ with an amplitude $F_0 = 8 \cdot 10^{-3}$ where the order parameter $\Delta v_y = 0$, *i.e.* the material has solidified. Note, that this value is identical to the amplitude of the external force at the fluidized-to-solid transition described in section 4.2.2. Therefore, we chose the solidification point to be at $F_s = (8.1 \pm 0.1) \cdot 10^{-3}$.

In order to find the fluidization point we increased the amplitude of the external force, F_0 , at times $t > 4 \cdot 10^3$ by the same procedure, *i.e.* with a waiting time of $\Delta t_{step} = 10^3$ and in steps of $\Delta F_{step} = 2 \cdot 10^{-4}$. If there would not be any hysteresis in the system the material should fluidize at $F_0 = 8.2 \cdot 10^{-3}$. However, the system is still solid at $t = 9 \cdot 10^3$. Finally, at $t = 1.4 \cdot 10^4$ where $F_0 = 1.3 \cdot 10^{-2}$, the system fluidizes. In order to save computational time we set the magnitude of the step in the external force to $\Delta F_{step} = 10^{-3}$. We chose $F_f = 1.25 \cdot 10^{-2}$ as the fluidization point and the corresponding error bar is $\Delta F_f = 5 \cdot 10^{-4}$. The ratio of the amplitude of the external force at the fluidization and the solidification points is $F_f/F_s \approx 1.54$. Therefore, the fluidized-to-solid transition (solidification) and the solid-to-fluidized transition (fluidization) occur at different applied driving amplitudes which proves the hysteretic nature of this transition.

Figure 4.25 displays the dynamic order parameter Δv_y , as a function of the amplitude of the external force, F_0 . The red squares show the first part of the hysteretic transition where we started by applying $F_0 = 8.8 \cdot 10^{-3}$ and decremented the amplitude in steps of $\Delta F_0 = 2 \cdot 10^{-4}$. The material solidified at $F_s = 8.1 \cdot 10^{-3}$. Subsequently, we incremented the amplitude of the external force until the material fluidized at $F_f = 1.25 \cdot 10^{-2}$.

4.4.1 Phase diagram

In the last section, we presented data for the strength of the external driving at the solidification and the fluidization point for a total area fraction of $\phi = 0.70$. It is obvious that both values should depend on the total area fraction, ϕ , the rupture separation S_c , and the system size L . First of all we will focus on the area fraction while we keep the remaining parameter of the system fixed. Hence, we construct a phase diagram that is based on the total area fraction of disks, ϕ , and the amplitude of the external force, F_0 .

Figure 4.26 shows the solidification and the fluidization transition lines as function of the

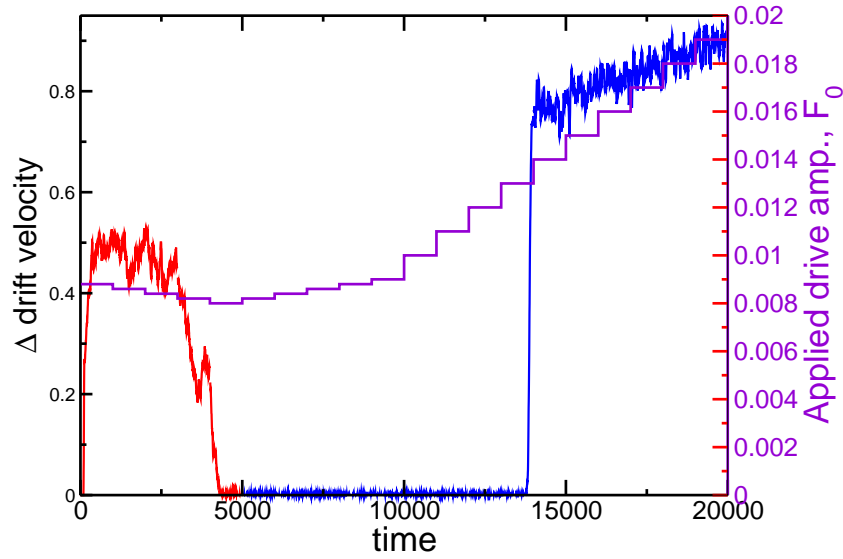


Figure 4.24: The dynamic order parameter Δv_y (the red and blue curves) and amplitude of the external force F_0 (the violet curve) as function of time. The total area fraction is $\phi = 0.7$, the rupture separation $S_c = 0.01$, and the system size $L = 18$.

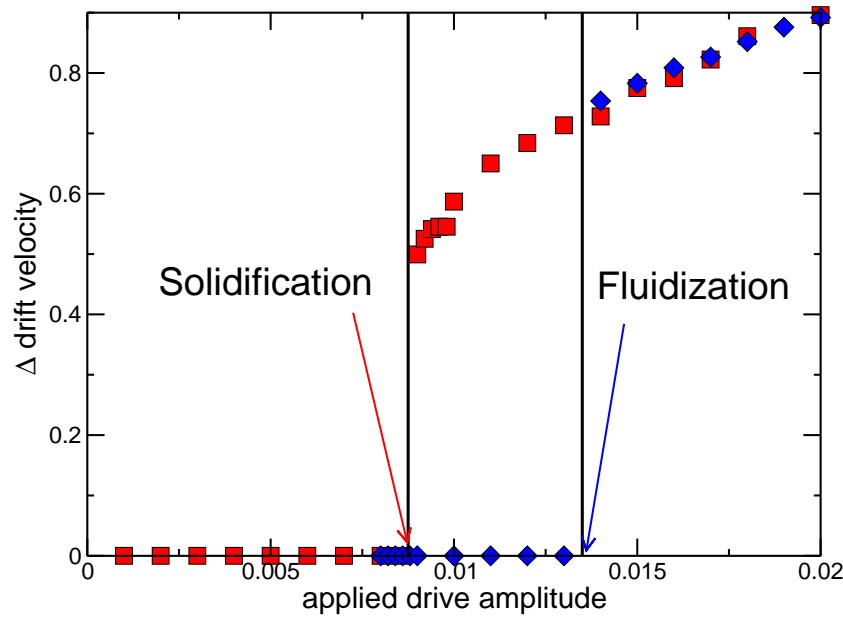


Figure 4.25: The dynamic order parameter, Δv_y , as function of the amplitude of the external force, F_0 . The solidification occurred at $F_0 = F_s = 8.1 \cdot 10^{-3}$ and the fluidization at $F_0 = F_f = 1.25 \cdot 10^{-2}$. The total area fraction is $\phi = 0.70$, the rupture separation $S_c = 0.01$, and the system size $L = 18$.

total area fraction. We probe the area fraction from $\phi_{min} \simeq 0.525$ to $\phi_{max} \simeq 0.84$. For $\phi > \phi_{max}$ fluctuations in the drift velocity become so large that one can not measure δv_y with a reliable error-bar. The value of ϕ_{max} coincides with the RCP limit $\phi_{RCP} = 0.84$ for the bidisperse system under consideration [104]. At total area fractions $\phi < \phi_{min}$ it may happen that the initially randomly distributed disks condense into two solid bands, one moving up while the other band is moving down. The evolution of the system can be totally different: On the one hand, the bands may collide and heat up. In this case, the system is attracted to a stationary fluidized state. On the other hand, the bands may not touch. In this case, the system stays cool and the two solid bands persist. Therefore, for $\phi < \phi_{min}$ the dynamics of the system depends on the initial configuration of the disks. However, for area fractions $\phi > \phi_{min}$ the stationary state is independent from the particular realization of the system in the initial state, *i.e.* after preparation.

Figure 4.26 displays the dynamic phase diagram for a system of wet disks under isochoric conditions being subject to a spatially heterogeneous external driving force. The plane is spanned by the amplitude of the external driving force multiplied to the system length $F_0 L$ on the y-axis and the total area fraction ϕ on the x-axis. We will show in appendix 4.5.1 that the force amplitude F_0 at both the fluidization and solidification point exhibit a simple scaling $F_0 \sim L^{-1}$ with the system size L .

The black curve in Fig. 4.26 indicates the solidification transition while the red curve in Fig. 4.26 corresponds to the fluidization transition. As discussed in section 4.2.2 we can estimate the amplitude of the external force at the solidification point from the time evolution of an ensemble of systems for different values of the driving force. We checked for different area fractions that the alternative protocol, where the driving force is slowly reduced until the disks solidify, and the ensemble method lead to identical values. This observation can be explained by the nature of the initial state in the ensemble method. Due to the preparation the system is found in a fluidized at the beginning of the simulation. Depending on the magnitude of the driving force, the system may be permanently fluidized or the fluidized state may only be a transient state.

Determining the fluidization line takes more computational efforts. The preparation of the solid state requires a slow decrease of the external driving force. Fluidization, or yielding, of the solidified disks requires a sufficiently slow increase of the external driving force. Hence, each point on the red curve takes more than one month of computational time. One sees that as one approaches to the limit of random close packing the amplitude of the external force at fluidization increases.

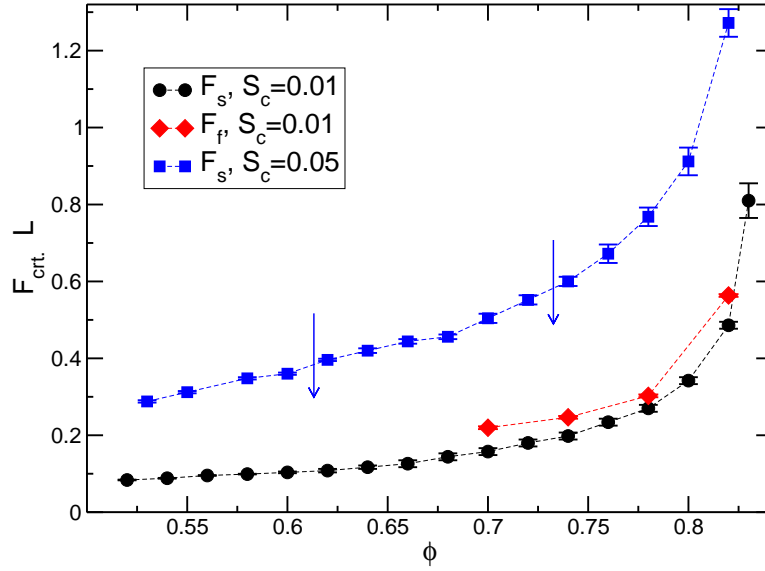


Figure 4.26: The rescaled amplitude of the external force, $F_0 \cdot L$, as a function of the total area fraction ϕ . The black curve shows the solidification line. The red curve is the corresponding fluidization curve. The rupture separation for the black and red line is $S_c = 0.01$. The Blue curve is the solidification line for $S_c = 0.05$.

The rescaled amplitude at the solidification point for a rupture separation $S_c = 0.05$ is depicted by the blue curve. The blue curve lies above the red curve. This is a clear indication that wet disks with a larger rupture length solidify already at larger driving forces when compared to wet disk with a smaller rupture length.

Now we would like to explore how the amplitude of the external force at solidification depends on the rupture separation of capillary bridges for a given total area fraction. Figure 4.27 shows the rescaled driving force $F_s \cdot L$ as a function of the rupture separation S_c . The total area fraction is fixed to $\phi = 0.70$ while the rupture separation is chosen in the range between 10^{-4} and 0.1 . The blue squares are the solidification thresholds for different rupture separations. We find an excellent collapse of our data into a power law scaling

$$F_s \sim S_c^\xi \quad (4.12)$$

with the exponent $\xi = 0.74 \pm 0.03$. This plot shows that as the rupture separation tends to zero the solidification threshold vanishes.

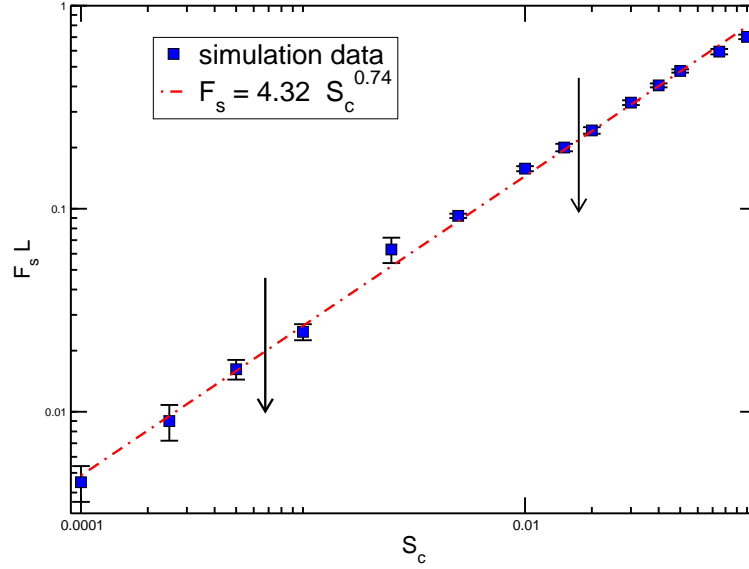


Figure 4.27: The rescaled amplitude of the external force at solidification, $F_s \cdot L$, as function of the rupture separation S_c . We find a power law behavior for the solidification line with an exponent 0.74 ± 0.03 .

4.4.2 Why hysteretic-discontinuous transition?

So far, by studying dynamics of wet disks on inclined plane (in last chapter) as well as wet disks driven by cosine shearing force, we observed that wet disks undergo through a hysteretic-discontinuous transition in both cases. Is the hysteretic-discontinuous transition caused by the fact that the liquid bridge force is in principle a discontinuous-hysteretic interaction (discontinuous in the sense that as soon as two grains touch each other a liquid bridge forms and entails to an attractive force). The answer is, however, “No”. Furthermore, to explain why the answer is no, we refer to series of earlier reports about the similar issue. Daniel Bonn et al.[70, 71] explored the rheological properties of dry granular matter, gels, foams, and emulsions. They showed that these materials, i.e. dry grains, gels, emulsions etc., undergo through a hysteretic-discontinuous transition between fluidized and solid states³ and they argued that such transition, i.e. hysteretic-discontinuous transition, belong to all the athermal materials that possess *yield stress*. Our results show that wet granular material should be also included into that category [105].

³Or in their language jamming and unjamming transition.

4.5 Appendix

4.5.1 Relation between driving force and shear stress

In this section we will derive a relation between the external force and the shear stress being valid for a stationary state bearing a certain symmetry. Let us first consider the Navier-Stokes equation:

$$\rho (\partial_t \mathbf{v} + \mathbf{v} \cdot \nabla \mathbf{v}) = -\nabla P + \nabla \cdot \underline{\mathbf{S}} + \mathbf{f} , \quad (4.13)$$

where \mathbf{v} is the velocity, ρ the fluid density, P the pressure, $\underline{\mathbf{S}}$ the stress tensor, while \mathbf{f} represents the body forces (per unit volume) acting on the disks, and ∇ the nabla operator.

In a stationary state, the first term on the RHS of equ. (4.13) vanishes while the second term is zero owing the particular symmetry of the velocity field. The velocity field depends exclusively on the lateral position x and has a non-zero component only into y -direction, *i.e.* the direction of the applied force. Hence, equ. (4.13) simplifies to a balance

$$\nabla \cdot \underline{\mathbf{S}} = \mathbf{f} \quad (4.14)$$

between the mechanical stress tensor and the external force. In Cartesian components, equ. (4.14) assumes the form

$$\partial_x S_{xx} + \partial_y S_{yx} = f_x \quad \text{and} \quad \partial_x S_{xy} + \partial_y S_{yy} = f_y . \quad (4.15)$$

Due to the translational invariance in y -direction, we have $\partial_y S_{yy} = 0$ and $\partial_y S_{xy} = 0$. Then, together with $f_x = 0$ it follows from equ. (4.15) that

$$\partial_x S_{xx} = 0 \quad \text{and} \quad \partial_x S_{xy} = f_y . \quad (4.16)$$

An integration of equ. (4.16) leads to

$$S_{xx} = \text{const.} \quad \text{and} \quad S_{xy}(x) = \int_0^x d\tilde{x} n(\tilde{x}) F_y(\tilde{x}) , \quad (4.17)$$

where $n(x)$ is the number of disks per area and $F_y(x)$ the y -component of the external driving force according to equ. (4.1) as function of the lateral position x . The dependence of the

Total area fraction	Linear fit
$\phi = 0.70$	$F_{crt.} = 0.148L^{-1}$
$\phi = 0.82$	$F_{crt.} = 0.46L^{-1}$

Table 4.3: Relation between the critical driving amplitude and the system size for two different area fractions.

external force on the coordinate x is given by:

$$F_y(x) = F_0 \cos\left(\frac{2\pi x}{L}\right) \quad (4.18)$$

where F_0 is the amplitude of the external force and L the dimension of the simulation box.

Inserting the RHS of (4.18) into the integral in equ. (4.17), we arrive at

$$S_{xy}(x) = \frac{n L F_0}{2\pi} \sin\left(\frac{2\pi x}{L}\right), \quad (4.19)$$

where we assumed the density n to be position independent.

In the fluidized state, n may become a function of the lateral position and the integral in equ. (4.17) cannot be evaluated in form of a closed analytical expression. In this case, we have to employ numerical data from our MD simulation and evaluate the integral (4.19) numerically.

In the following we will assume that the concepts of continuum mechanics apply to the isochoric system of sheared wet disks under consideration. Locality requires that the points of solidification and fluidization should be related to a certain characteristic value of the shear stress being a function of purely local quantities such as density, granular temperature. Whenever this is the case and, in addition, these quantities are system size independent, the prefactor of the sine in equ. (4.19) shows that the amplitude of the driving force at the fluidization and solidification point should scale as $F_0 \sim L^{-1}$.

We checked the dependence of the amplitude of the external force at fluidization and solidification for three different values of the system size $L = \{18, 24, 30\}$ and two different total area fraction $\phi = \{0.70, 0.82\}$. Figure 4.28 shows the amplitude of the external force at solidification, F_s , as a function of the inverse system length, L^{-1} . The red circles correspond to $\phi = 0.70$, and the blue squares correspond $\phi = 0.82$.

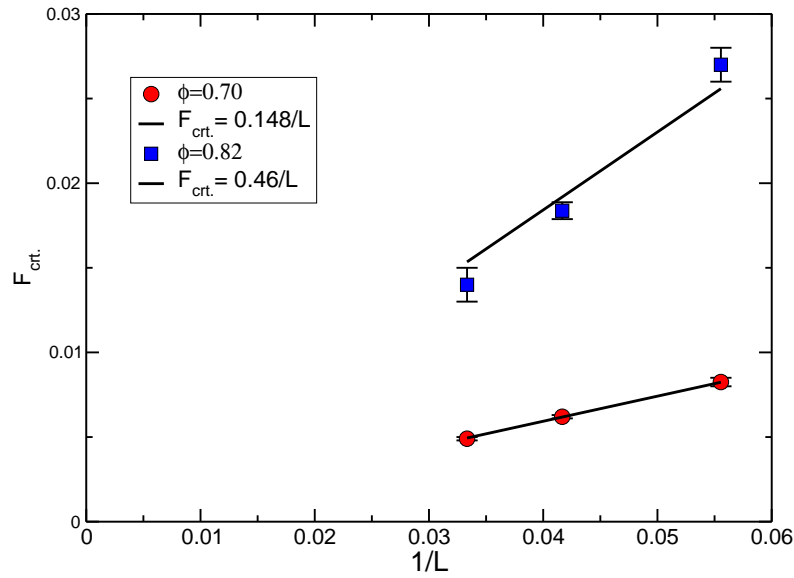


Figure 4.28: Using the assumption that the yield stress should not depend on the system size, one can predict that F_f has to scale linearly with L^{-1} . In this figure, F_f depicted as a function of L^{-1} . The blue and red squares correspond to $\phi = \{0.70, 0.82\}$ respectively. We find a perfect agreement with the theoretical prediction based on continuum mechanics. The rupture separation is $S_c = 0.01$.

Chapter 5

Conclusion

In this thesis, we studied the stability and the dynamics of wet granular material under shear. Our goal was to show that the hysteresis and the discontinuity of the fluidization transition are generic features of wet granular materials. In chapter 2 we compare and explore the stability of dry and wet granular piles. A dry granular pile fluidizes if the inclination angle exceeds a critical angle which depends on the configuration of the particles. At a certain critical angle the fluidization occurs simultaneously everywhere in regular frictionless dry piles. In contrast, when the pile is wet, it can be tilted beyond the critical angle due to support of the capillary bridges between particles. For inclination angles beyond the critical angle, the highest tensile force acts on the capillary bridges in the bottom layer supporting the pile. The pile fluidizes when the tensile force becomes larger than the strength of the capillary bridges. Accordingly, *a wet granular pile yields in the bottom layer*. This changes our thoughts about yielding of granular piles where traditionally surface fluxes are considered. Extensive MD-type simulations prove the predictive power of the theory.

In chapter 3 we studied the dynamics of wet disks in a channel. The fluidized system is homogeneous for small rupture separations S_c and becomes heterogeneous for larger S_c . The solidification occurs if the inclination angle is sufficiently decreased below the fluidization point. The difference between the solidification and fluidization points shows that wet disks undergo a hysteretic dynamic transition. For small gravitational downhill forces, the system becomes heterogeneous. It is dilute close to the stick boundary and packed near the upper wall such that it resembles a *Leidenfrost state*.

The dynamics of wet disks under a spatially heterogeneous driving force is explored in chapter 4. There is a well defined applied force amplitude below which the system undergoes

a fluidized-to-solid transition. The solidified system re-fluidizes if the applied driving force can overcome adhesion due to the capillary bridges. A phase diagram showing the fluidization and solidification transition thresholds is presented. From our perspective the phase diagram is an example of a jamming phase diagram. It proves that interactions between particles influence the structure of the jamming phase diagram. Above $\phi \approx 0.525$ a percolation cluster developing yield stress emerges after a fluidized-to-solid transition irrespective of the initial position of the particles. Furthermore, F_s and F_f are independent from the initial configuration of particles. Below, the dynamics of the system strongly depends on the preparation process at the beginning of the simulation. We truly believe that $\phi \approx 0.525$ is a point that has unique physical properties which has not yet fully been explored and is a subject for future studies. Viscosity is another physical quantity that has been intimately studied in chapter 4. We showed that local viscosity of the fluidized state is dominated by the local area fraction ϕ and not the granular temperature T_G . We found an approximate scaling $\eta \sim (\rho_c - \rho)^{-1}$ of the viscosity with the local area fraction ρ . In chapter 4 we also studied the force distribution in the solid and fluid states. The force distribution is a key tool to study the force chains in a granular systems. We showed that in the solidified state the stability of the assembly is dominated by the stretched capillary bridges. The probability to find a stretched capillary bridge sharply increases as the system fluidizes.

Appendices

Appendix A

Symbols and notations

Symbol	Description
P_L	Laplace Pressure
RCP	Random Close Packing
f_{LB}	Capillary Force
S_c	Rupture Separation
ϕ	Total Area Fraction
ϕ_c	Area Fraction of RCP
T_G	Granular Temperature
g	Gravitational Acceleration
$g_{sed.}$	g of Sedimentation
$t_{sed.}$	Sedimentation Time
\mathbf{F}_{drag}	Background Drag Force
ϕ	Total Area Fraction
ρ	Local Area Fraction
$\delta\rho$	Difference of Local Area Fraction
N_{LB}	Number of Liquid Bridges
f_R	Rupture Frequency
$\hat{\mathbf{S}}$	Stress Tensor
S_{xy}	Shear Stress
S_{yy}	Normal Stress
S_{xx}	Tangential Stress
S_{xy}^*	Yield Stress
g	Gravitational Acceleration
g_c	Critical Gravitational Acceleration
θ	Inclination Angle
θ_c	Critical Inclination Angle
δ	Gap Between Disks
$Dtime$	Damping Time
F_s	Solidification Driving Amplitude
F_f	Fluidization Driving Amplitude
n	Number of Particles in Unit Area
$\dot{\gamma}$	Shear Rate
$\dot{\Gamma}$	Shearing Tensor
β	Effective Compressibility

Appendix B

Energy balance

In the current section, we explore the balance of the injected and dissipated energies in fluidized states both for the cosine shearing and for wet disks running down on an inclined plane.

Fig.B.1 shows the dissipated and the injected powers as a function of the time by the black and red curves respectively. The total area fraction is $\phi = \{0.60, 0.70\}$ for the top and bottom graphs respectively. One sees that the dissipated power fluctuates more than the injected energy but both seem to have the same average. Integration of the injected and dissipated powers with respect to the time is shown by the green and blue curves respectively.

A quantitative explanation for the energy balance comes out when one calculates the relative difference of the injected and the dissipated energies. FigB.2 shows the relative difference of the injected and dissipated energies as a function of the total area fraction. There is no any systematic dependence on the total area fraction. Subsequently, the average relative difference is:

$$\left\langle \frac{\int P_{inj} \cdot dt - \int P_{diss} \cdot dt}{\int P_{inj} \cdot dt} \right\rangle = 0.000543577 \quad (B.1)$$

The equ.(B.1) proves that our integration scheme is very accurate, and on the other hand, it shows that as one intuitively expects, in the stationary state, the injected and dissipated energies balance.

Similar calculations are done for wet disks running down on an inclined plane. We have shown that the same accuracy also holds for such a system.

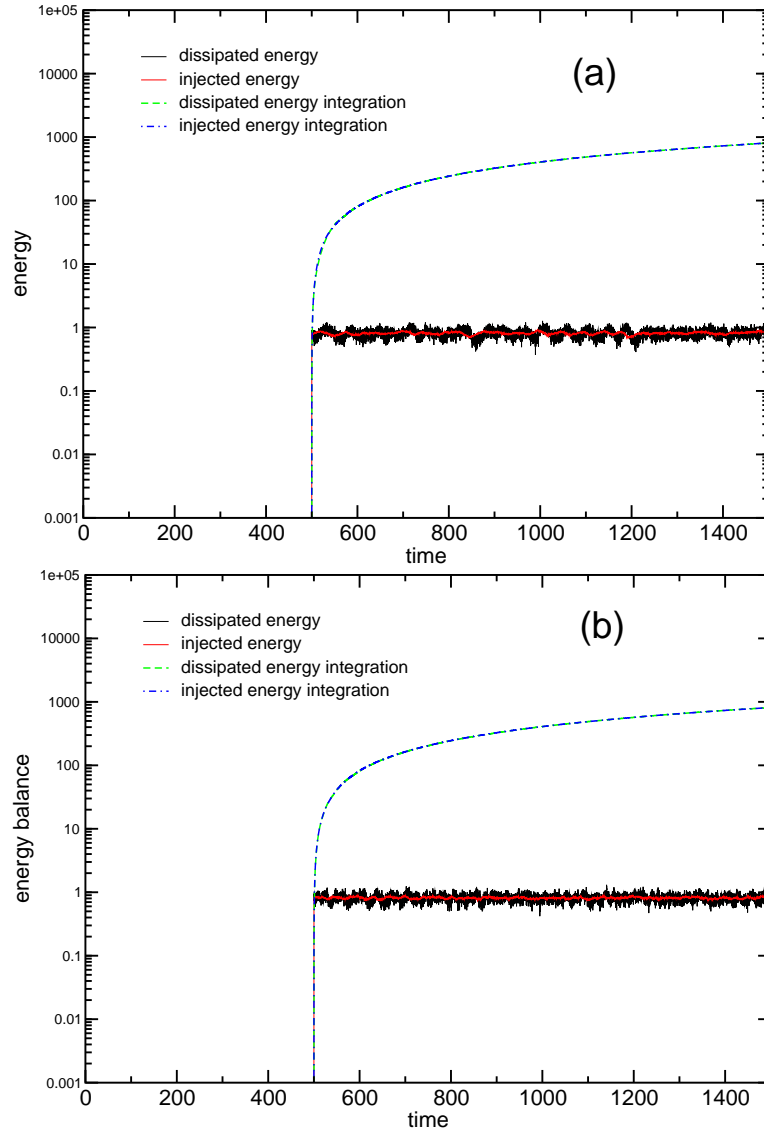


Figure B.1: (Top) The injected and dissipated power and their integration for $\phi = 0.60$. (Bottom) The injected and dissipated power and their integration for $\phi = 0.70$. The black, red, green, and blue curves show the dissipated power, the injected power, the dissipated energy, and the injected energy respectively.

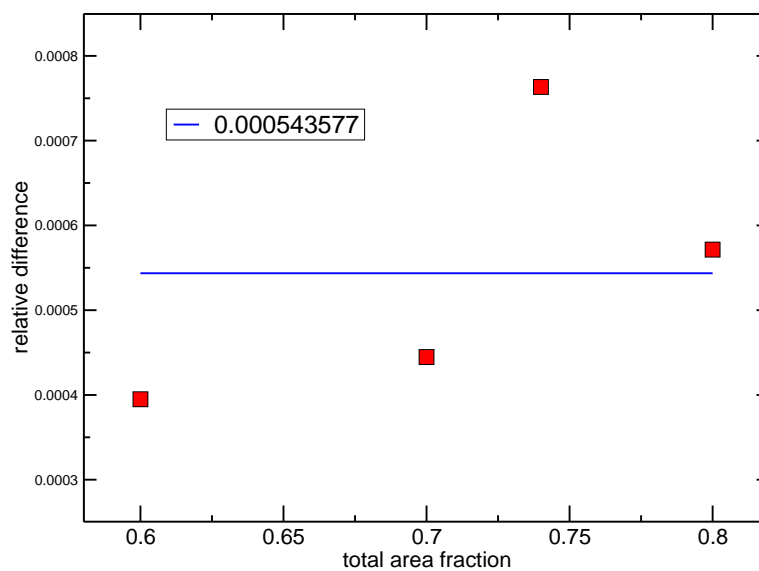


Figure B.2: Percentage of the relative difference of the injected energy and the dissipated energy as a function of the total area fraction.

Appendix C

Derivation of stress tensor

C.1 Tensorial form of the Virial theorem

The stress tensor is a mathematical tool to explore the momentum transfer in the system. One of the main tools that strongly equipped us to study dynamics of wet discs under shear. Therefore, in this section, we want to present derivation of the stress tensor from the tensorial form of the Virial theorem.

The tensorial form of the Virial quantity can be defined as:

$$\langle \xi \rangle = \left\langle \frac{1}{V} \sum_i \vec{r}_i \otimes \vec{p}_i \right\rangle \quad (\text{C.1})$$

in which ξ is the Virial quantity, V is the volume of the homogeneous sample, \vec{r}_i and \vec{p}_i are the position and momentum vectors of the particle i . \otimes is the tensor product and m_i is mass of the particle i .

Since ξ describes interactions of particles which are inside a homogeneous portion, then $\langle \frac{d\xi}{dt} \rangle$ should be equal zero. By virtue of equ.C.1, one can write:

$$\langle \frac{1}{V} \sum_i \vec{p}_i \otimes \vec{p}_i \rangle + \langle \frac{1}{V} \sum_i \vec{r}_i \otimes \vec{F}_i \rangle = 0 \quad (\text{C.2})$$

For the simplicity, we define:

$$\chi = \langle \frac{1}{V} \sum_i \vec{r}_i \otimes \vec{F}_i \rangle \quad (\text{C.3})$$

We separate the interactions of particle i with the particles that are inside and outside the

portion.

$$\chi = \langle \frac{1}{V} \sum_i \vec{r}_i \otimes \vec{F}_i^{int.} \rangle + \langle \frac{1}{V} \sum_i \vec{r}_i \otimes \vec{F}_i^{ext.} \rangle = \chi_1 + \chi_2 \quad (C.4)$$

Where:

$$\chi_1 = \langle \frac{1}{V} \sum_i \vec{r}_i \otimes \vec{F}_i^{int.} \rangle \quad (C.5)$$

$$\chi_2 = \langle \frac{1}{V} \sum_i \vec{r}_i \otimes \vec{F}_i^{ext.} \rangle \quad (C.6)$$

In the case of granular material, in which the interactions are short range limited to the neighbors of particles, each particle can have maximum 6 or 12 neighbors in two and three dimension respectively. χ_2 consists the interactions of particles near the boundary with particles outside the portion. Therefore, we change the summation in χ_2 to an integral on surface of the portion:

$$\langle \sum_i \rangle \Rightarrow \oint_{bound.} \sum_{\gamma} dA_{\gamma} \quad (C.7)$$

The dyadic form of χ_2 can be written as:

$$\begin{aligned} (\chi_2)_{dyad} &= \frac{1}{V} \oint_{bound.} \sum_{\gamma} (\vec{r} \otimes \vec{F})_{\beta\gamma} dA_{\gamma} = \frac{1}{V} \oint_{bound.} \sum_{\gamma} (r_{\gamma} (S_{\beta\gamma} + \rho U_{\beta} U_{\gamma})) dA_{\gamma} \\ &= \frac{1}{V} \oint \sum_{\gamma} \nabla_{\gamma} (r_{\gamma} (S_{\beta\gamma} + \rho U_{\beta} U_{\gamma})) d^3 r \end{aligned} \quad (C.8)$$

$$(\chi_2)_{dyad} = \frac{1}{V} (S_{\beta\gamma} + \rho U_{\beta} U_{\gamma}) \oint \sum_{\gamma} \nabla_{\gamma} \cdot \vec{r}_{\gamma} d^3 r \quad (C.9)$$

Therefore, χ_2 can be simplified as:

$$\chi_2 = S + \rho \vec{U} \otimes \vec{U} \quad (C.10)$$

Where \vec{U} is the drift velocity in the portion, and ρ is the density.

χ_1 can be interpreted as an expression which consists interactions of the particles with each other inside the portion:

$$\begin{aligned}
\chi_1 &= \langle \frac{1}{V} \sum_i \vec{r}_i \otimes \vec{F}_i^{int.} \rangle = \langle \frac{1}{V} \sum_{j>i} \vec{r}_{ij} \otimes \vec{F}_{ij}^{int.} \rangle \\
&= \frac{1}{V} \vec{R} \otimes \vec{F}^{int.}
\end{aligned} \tag{C.11}$$

Therefore, we can simplify the stress tensor as a function of the internal and boundary interactions as well as the drift velocity in the portion:

$$S = \frac{1}{V} \sum_i (\vec{v}_i - \vec{U}) \otimes (\vec{v}_i - \vec{U}) + \frac{1}{V} \vec{R} \otimes \vec{F}^{int.} \tag{C.12}$$

C.2 Stress Tensor in 2D

The stress tensor in dyadic form is:

$$S = \frac{1}{A} \sum_i (\vec{v}_i - \vec{U}) \otimes (\vec{v}_i - \vec{U}) + \frac{1}{A} \vec{R} \otimes \vec{F}^{int.} \tag{C.13}$$

In which A is area of the portion. The stress tensor in 2D is a 2×2 matrix:

$$S = \frac{1}{A} \sum_i ((v_{i_x} - U_x)\hat{i} + (v_{i_y} - U_y)\hat{j})^2 + \frac{1}{A} (R_x F_x^{int} \hat{i}\hat{i} + R_x F_y^{int} \hat{i}\hat{j} + R_y F_x^{int} \hat{j}\hat{i} + R_y F_y^{int} \hat{j}\hat{j}) \tag{C.14}$$

Or:

$$S = \frac{1}{A} \begin{pmatrix} \sum_i (v_{i_x} - U_x)^2 & \sum_i (v_{i_x} - U_x)(v_{i_y} - U_y) \\ \sum_i (v_{i_x} - U_x)(v_{i_y} - U_y) & \sum_i (v_{i_y} - U_y)^2 \end{pmatrix} + \frac{1}{A} \begin{pmatrix} R_x F_x^{int} & R_x F_y^{int} \\ R_y F_x^{int} & R_y F_y^{int} \end{pmatrix} \tag{C.15}$$

One can calculate the effective viscosity η , the effective compressibility β , pressure P of the system as the following:

$$\begin{aligned}
\nu &= -\frac{(S_{xy} + S_{yx})}{2\Gamma} \\
P &= tr(S) \\
\beta &= A \frac{P}{2K}
\end{aligned}$$

Where K is the drift subtracted kinetic energy of the system.

References

- [1] H. M. Jaeger, S. R. Nagel, R. P. Behringer, *Rev. of Mod. Phys.*, **68** 4, (1996).
- [2] S. Herminghaus, *Advances in Physics*, **54** 221, (2005).
- [3] M. Bertz, J.B. Cunningham, P.L. Kurczynski, F. Nori, *Phys. Rev. Lett.*, **69** 2431, (1992).
- [4] A. Fingerle, S. Herminghaus, V. Yu. Zaburdaev, *Phys. Rev. E*, **75** 61301, (2007).
- [5] L. Boquet , E. Charlaix, S. Ciliberto J. Crassous, *Nature*, **396** 732, (1998).
- [6] N. Fraysse, H. Thome and L. Petit, *Eur. Phys J. B*, **11** 615, (1999).
- [7] G. D. Anna , *Phys. Rev. E*, **62** 62982, (2000).
- [8] M. Scheel, R. Seemann, M. Brinkmann, M. Di Michiel, A. Sheppard, B. Breidenbach, S. Herminghaus, *Nature Materials*, **7** 189, (2008).
- [9] P. Bartlet, B. Othmar, *Physics World*, **14** 25, (2001).
- [10] Kansai International Airport Co. Ltd. Brief summary of settlement, www.kaiac.co.jp
- [11] M. Schulz , B. M. Schulz, S. Herminghaus, *Phys. Rev. E*, **67** 5, (2003).
- [12] X. Y. Yang, C. Huan, D. Candela, R. W. Mair, R. L. Walsworth , *Phys. Rev. Lett.*, **88** 44301, (2002).
- [13] B. Utter, R. P. Behringer, *Phys. Rev. E*, **69** 31308, (2004).
- [14] P. A. Thompson, G. S. Grest, *Phys. Rev. Lett.*, **67** 1751, (1991).

-
- [15] W. Losert, L. Bocquet, T. C. Lubensky, J. P. Gollub, *Phys. Rev. Lett.*, **85** 7, (2000).
- [16] N. Xu, C. S. O'Hern, L. Kondic, *Phys. Rev. Lett.*, **94** 16001, (2005).
- [17] R. Dikau, D. Brunsden, L. Schrott, M. L. Ibsen, *Landslide Recognition*, Wiley (1996).
- [18] D. K. Keefer, *Bulletin of the Geological Society of America*, **95** 406, (1984).
- [19] N. Caine, *Geografiska Annale*, **62** 23, (1980).
- [20] D. J. Varnes, *United Nations Educational, Scientific and Cultural Organization*, (1984).
- [21] C. J. Chung, A. G. Fabbri, *Photogrammetric engineering and remote sensing*, **65** 1389, (1999).
- [22] D. M. Cruden, *Bulletin International Association for Engineering Geology*, **43** 27, (1991).
- [23] D. J. Varnes, *Landslide Analysis and Control*, **176** 11, (1978).
- [24] J. N. Hutchinson, *5th. Int. Symp. on Landslide*, **1** 3, (1988).
- [25] J. N. Hutchinson, *Proc. Geotech. Conf.*, **1** 113, (1967).
- [26] J. N. Hutchinson, *Encyclopaedia of Geomorphology*, (1968).
- [27] J. N. Hutchinson, *Geotechnique*, **20** 412, (1970).
- [28] J. N. Hutchinson, *J. Japan Landslide Society*, **21** 1, (1984).
- [29] H. Ochiai et al., *Landslides*, **3** 211, (2004).
- [30] A. W. Bishop, *Q. J. Eng. Geol.*, **6** 335, (1973).
- [31] R. L. Shreve, *Geol. Soc. Am. Spec. Pap.*, **108** 47, (1968).
- [32] T. H. Erismann, G. Abele, *Springer*, (2001).
- [33] E. C. Spiker and P. L. Gori, *National Landslides Mitigation Strategy*, (2003).
- [34] F. V. De Blasio, *Rock Mechanics and Rock Engineering*, **41** 219 (2008).

-
- [35] S. Smith-Shaller, *Review of proposed mechanisms for Sturzstroms (long-runout landslides)*, **185**, (1996).
- [36] H. J. Melosh, *Journal of Geophys. Res.*, **84** 7513, (1979).
- [37] K. J. Hsü, *Geol. Soc. Am Bull*, **86** 129, (1975).
- [38] T. R. H. Davies, *Rock Mechanics*, **15** 9, (1982).
- [39] C. S. Campbell, P. W. Cleary, M. Hopkins, *Journal of Geophys. Res.*, **100** 8267, (1995).
- [40] S. Straub, *Particulate Gravity Currents*, **31** (2001).
- [41] P. Habib, *Rock Mechanics and Rock Engineering*, **7** , 193 (1975).
- [42] J. Goguel, *Geothermics*, McGraw-Hill, New York (1976).
- [43] J. P. Hyslip, L. E. Vallejo, *Engineering Geology*, **48** 231 (1997).
- [44] F. Soulie, F. Cherblane, M. S. El Youssoufi, C. Saix, *Int. J. Numer. Analyt. Mech Geomech.*, **30** 213, (2006).
- [45] A. Fingerle, S. Herminghaus, V. Zaburdaev, *Phys. Rev. Lett*, **95** 198001 (2005).
- [46] A. Fingerle and S. Herminghaus, *Phys. Rev. Lett.*, **97** 78001 (2006)
- [47] V. Yu. Zaburdaev and S. Herminghaus, *Phys. Rev E*, **75** 31304 (2007).
- [48] L. D. Landau, E. M. Lifshitz, A M Kosevich, L P Pitaevskii, *Theory of elasticity*, (1986).
- [49] B. J. Adler, T. E. Wainwright, *J. Chem. Phys.*, **27** 1208, (1957).
- [50] B. J. Adler, T. E. Wainwright, *J. Chem. Phys.*, **31**, 459, (1950).
- [51] B. J. Adler, T. E. Wainwright, *J. Chem. Phys.*, **33** 1439, (1960).
- [52] T. Pöschel, T. Schwager, *Computational granular dynamics*, Springer, (2004).
- [53] N. V. Brilliantov, T. Pöschel, *Kinetic theory of granular gases*, Oxford University Press, (2003).
- [54] X. Nie, E. Ben-Naim, and S. Chen, *Phys. Rev. Lett.*, **89** 204301, (2002).

- [55] V. Yu. Zaburdaev, M. Brinkmann, S. Herminghaus, *Phys. Rev. Lett.*, **97** 18001, 2006
- [56] N. Xu, C. S. O'Hern, L. Kondic, *Phys. Rev. Lett.*, **94** 16001, (2005).
- [57] N. Xu, C. S. O'Hern, *Phys. Rev. Lett.*, **94** 55701, (2005).
- [58] N. Xu, C. S. O'Hern, L. Kondic, *Phys. Rev. E*, **72** 41504, (2005).
- [59] N. Xu, C. S. O'Hern, *Phys. Rev. E*, **73** 61303, (2006).
- [60] V. Richefeu, M. S. El Youssoufi, F. Radja, *Phys. Rev. E*, **73** 051304, 2006.
- [61] M. Schulz, B. M. Schulz, S. Herminghaus, *Phys. Rev. E*, **67** 52301, (2003).
- [62] M. P. Allen, D. J. Tildesley, *Computer simulation of liquids*, Oxford science publications, (1986).
- [63] T. Poeschel, T. Schwager, *Springer*, (2005).
- [64] J. H. Snoeijer, T. J. H. Vlugt, W. G. Ellenbroek, M. van Hecke, J. M. J. van Leeuwen, *Phys. Rev. E*, **70** 61306, (2004).
- [65] C. F. Moukarzel, *Phys. Rev. Lett.* **81**, 1634, (1998).
- [66] C. S. O'Hern, L. E. Silbert, A. J. Liu, S. R. Nagel, *Phys. Rev. E*, **68** 11306, (2003).
- [67] R. A. Bagnold, *Proc. R. Soc. London, Ser. A*, **225** 49, (1954).
- [68] R. Brewster, G. S. Grest, J. W. Landry, A. J. Levine, *Phys. Rev. E*, **72** 61301, (2005).
- [69] P. Eshuis, K. van der Weele, D. van der Meer, D. Lohse, *Phys. Rev. Lett.*, **95** 258001, (2005).
- [70] F Da Cruz, F. Chevoir, D. Bonn, P. Coussot, *Phys. Rev. E*, **66**, (2002).
- [71] P. Coussot, Q. D. Nguyen, H. T. Huynh, D. Bonn, *Phys. Rev. Lett.*, **88** 17, (2002).
- [72] J. S. A. Green, *J. Fluid Mech.* **62** 273, (1974).
- [73] L. D. Meshalkin and Y. G. Sinai, *J. Appl. Math. Mech.* **25** 1700, (1961).
- [74] B. D. Lubachevsky, F. H. Stillinger, *Jour. of Stat. Phys.*, **60** 561, (1990).

-
- [75] S. Strogatz, *Non-linear Dynamics and Chaos*, Perseus Books, (2000).
- [76] J. C. Williams, *Powder Technol.* **15** 245, (1976).
- [77] D. Geromichalos, M. M. Kohonen, F. Mugele and S. Herminghaus, *Phys. Rev. Lett.*, **90** 168702, (2003).
- [78] O. R. Walton, R. L. Braun, *Jour. of Rheology* **30** 949, (1986).
- [79] R. Garcia-Rojo, S. Luding, J.J. Brey, *Phys. Rev. E*, **74** 061305, (2006).
- [80] H. M. Jaeger, S. R. Nagel, and R. P. Behringer, *Rev. Mod. Phys.* **68** 1259, (1996).
- [81] T. Travers, M. Ammi, D. Bideau, A. Gervois, J.C. Messenger, and J.P. Troadec, *Europhys. Lett.*, **4** 329 (1987).
- [82] E. Guyon, S. Roux, A. Hansen, D. Bideau, J.-P. Troadec, and H. Crapo, *Rep. Prog. Phys.*, **53** 373 (1990).
- [83] C. Liu and S. R. Nagel, *Phys. Rev. Lett.*, **68** 2301, (1992).
- [84] M. Leibig, *Phys. Rev. E*, **49** 1647, (1994).
- [85] S. Melin, *Phys. Rev. E* **49** 2353, (1994).
- [86] A. V. Potapov and C. S. Campbell, *Phys. Rev. Lett.*, **77** 4760, (1996).
- [87] R. S. Sinkovits and S. Sen, *Phys. Rev. Lett.*, **74** 2686, (1995).
- [88] M. Ammi, D. Bideau, and J. P. Troadec, *J. Phys. D* **20** 424, (1987).
- [89] C. Liu, S. R. Nagel, D. A. Schecter, S. N. Coppersmith, S. Majumdar, O. Narayan, and T. A. Witten, *Science*, **269** 513, (1995).
- [90] G. W. Baxter, in *Powders and Grains 97*, edited by R. P. Behringer and J. T. Jenkins Balkema, *Rotterdam*, (1997)
- [91] D. M. Mueth, H. M. Jaeger, and S. R. Nagel, *Phys. Rev. E* **57** 3164, (1998).
- [92] F. Radjai, S. Roux, and J. J. Moreau, *Chaos* **9** 544, (1999).
- [93] D. L. Blair *et al.*, *Phys. Rev. E* **63** 041304, (2001).

- [94] S. N. Coppersmith, C. Liu, S. Majumdar, O. Narayan, and T. A. Witten, *Phys. Rev. E*, **53** 4673, (1996).
- [95] F. Radjai, M. Jean, J. J. Moreau, and S. Roux, *Phys. Rev. Lett.*, **77** 274, (1996).
- [96] C. Goldenberg and I. Goldhirsch *Phys. Rev. Lett.* **89** 084302, (2002).
- [97] F. Radjai, D. Wolf, M. Jean, and J. J. Moreau unpublished.
- [98] F. Radjai, D. E. Wolf, S. Roux, M. Jean, and J. J. Moreau, *Powders and Grains*, (2001).
- [99] S. Luding, *Phys. Rev. E*, **55** 4720, (1997).
- [100] B. Miller, C. O'Hern, and R. P. Behringer, *Phys. Rev. Lett.*, **77** 3110, (1996).
- [101] C. Eloy and E. Clement, *J. Phys. (France)* **I 7** 1541, (1997).
- [102] H. Kuno and I. Kuri, *Powder Technol.*, **34** 87, (1983).
- [103] C.S. O'Hern, S.A. Langer, A.J. Liu, S.R. Nagel, *Phys. Rev. Lett.*, **86** 111, (2001).
- [104] N. Xu, PhD thesis, Yale University (2005).
- [105] Private Communications, I. Aronson, (2009).

Acknowledgments

This work would not have been possible without the support and encouragement of a large number of my colleagues and friends. First, I would like to appreciate *Prof. Dr. Stephan Herminghaus* for offering me the opportunity to work under his supervision. Soon after joining his department, I realized that there holds a special place within the larger Max-Planck society, since the director was not only a physicist, but also an artist or, maybe a better term to use, a “Künstler”. It would be honest that it was not sometimes easy for me to go along with a person who thinks way more faster than a typical one does. I, hereby, would like to thank *Dr. Martin Brinkmann* for advising me during my PhD project. During last three years, it was his great sense of commitment toward this project which, among others, played the role of an encouraging factor for me to move further on. I’ve been deeply benefited from his unique physical intuition and smart computer programming skills. His helps during the final steps of preparing my dissertation are unforgettable. *PD. Dr. Jürgen Vollmer* took responsibility for coordinating the project when *Dr. Brinkmann* was away for medical reasons. Besides being a great theoretician, *Dr. Vollmer’s* excellent management skills led me toward getting exciting results in a fairly short period of invaluable time. Submitting these results to a refereed journal enabled me to hand in my thesis. I would like to express my gratitude to *PD. Dr. Jürgen Vollmer* for his great supports at a very critical time.

I would like to thank all of my colleagues at the Max-Planck Institute for Dynamics and Self-Organization to supporting me all the time. Especially, Dr. Enkhtuul Surenjav for giving me a lot of advices on graduation process, Shashi Thutupalli for reading the third chapter of the thesis and giving great comments, Dr. Zeina Khan, Klaus Roeller, Dr. Matthias Schroeter, Prof. Dr. Ralf Seemann, and Sonia May.

My friends at the town with whom I filled all of my weekends and holidays, Enayat Khojasteh, Saber Qanbari, Sina Mozaffari, Conny Bellersen, Marlen Schiche, Dr. Ping Lee, and Toni Froehlich. Our secreter Mrs. Monika Teuteberg who is the best secreter I have ever seen.

Finally, my singing teacher Mrs. Uta Grunewald who gave me wings to fly in the worlds of classical music.

Erklärung

1. Ich habe diese Arbeit selbständig und ohne unerlaubte Hilfe angefertigt und dabei nur die angegebenen Quellen benutzt.
2. Ich habe noch keinen Promotionsversuch unternommen.

Göttingen, den 22 April 2009.

Seyed Habibollah EBRAHIMNAZHAD RAHBARI

Scientific Papers Published :

1. S. H. Ebrahimpnazhad Rahbari, J. Vollmer, S. Herminghaus, M. Brinkmann, ‘ *A response function perspective on yielding of wet granular matter*’, *Europhys. Lett.*, **87** 14002, (2009).
2. S. H. Ebrahimpnazhad Rahbari, J. Vollmer, S. Herminghaus, M. Brinkmann, ‘ *Fluidization transition in wet granulates under shear*’, *submitted to Phys. Rev. E*.
3. S. H. Ebrahimpnazhad Rahbari, J. Vollmer, S. Herminghaus, M. Brinkmann, ‘ *Wet disks running down on an inclined plane*’, *in preparation*.
4. S. H. Ebrahimpnazhad Rahbari, J. Vollmer, S. Herminghaus, M. Brinkmann, ‘ *Wet disks sheared with Lees-Edwards boundary conditions*’, *in preparation*

Lebenslauf

Persönlicher Status

Name : Seyed Habibollah EBRAHIMNAZHAD RAHBARI
Geburtsdatum : 17. November 1979
Geburtsort : Tabriz, West Azarbayjan, Iran
Wohnort : Gauswohnheim, 37073 Göttingen
Staatsangehörigkeit : Iranisch

Ausbildung

April 2006 – seit Doktorarbeit am Max-Planck Institut für Dynamik und Selbstorganisation, Göttingen (Prof. Dr. Stephan Herminghaus).

2005 Sept. – Praktikum am Max-Planck Institute für Biophysikalechemie,
2006 Abteilung Prof. Troe, Theoretische Reaction Dynamics Group

2001 – 2005 Masterarbeit in Theoretische Physik Tehran Universität, Tehran, Iran.
Projekt: '*Gravitational Microlensing by Rotating Stars*' (Prof. Dr. Mohammad Nouri-Zonoz).

1997 – 2001 Bachelor in Physik, Tabriz Universität, Tabriz, Iran.